CONTINUUM- BASED COMPUTATIONAL MODELS OF BIOLOGICAL LIVING CELL

A Thesis

by

FEIFEI CHENG

Submitted to the Office of Graduate Studies of
Texas A&M University
in partial fulfillment of the requirements for the degree of

MASTER OF SCIENCE

December 2008

Major Subject: Mechanical Engineering

CONTINUUM- BASED COMPUTATIONAL MODELS OF BIOLOGICAL LIVING CELL

A Thesis

by

FEIFEI CHENG

Submitted to the Office of Graduate Studies of
Texas A&M University
in partial fulfillment of the requirements for the degree of

MASTER OF SCIENCE

Approved by:

Chair of Committee,	J.N. Reddy
Committee Members,	Xinlin Gao
	Harry Jones
Head of Department,	Dennis O'Neal

December 2008

Major Subject: Mechanical Engineering

ABSTRACT

Continuum- based Computational Models of Biological Living Cell. (December 2008)

Feifei Cheng, B. E., Dalian University of Technology, China

Chair of Advisory Committee: Dr. J.N. Reddy

All living creatures, despite their profound diversity, share a common architectural building block: the cell. Cells are the basic functional units of life, yet are themselves comprised of numerous components with distinct mechanical characteristics. It is well established that cells have the ability to sense and respond to externally applied forces. However, the detailed mechanism of mechanosensation is still not clearly understood, and is an active area of research involving experimental and theoretical works. Mathematical modeling of the mechanical stimulus correlating to different experimental stimulation procedures forms the first step to understanding the mechanosensation in cellular system. In this thesis, a continuum -based computational model of living cells that explicitly incorporate the material properties of various cellular components are developed. In the constitutive modeling of cell, the continuum standard linear solid viscoelastic model (SLS), its natural extension for large scale deformation standard Neo-Hookean solid viscoelastic model (SnHS) as well as polymer mechanics-based dynamic shear modulus model was introduced. Finite element simulations of three widely used experiments- atomic force microscopy (AFM), magnetic twisting cytometry (MTC) and micropipette aspiration in the quantification of cell properties were carried out to verify the developed constitutive model.

From the results of AFM finite element simulation, it was observed that the force-deformation and strain-relaxation curves obtained fit the experimental results very well. The influences of cytoplasm shear modulus which varies due to the formation of stress fiber, and cortex shear modulus which alters with the actin filament concentration factors and load frequency were systematically studied. Similarly, in magnetic twisting cytometry (MTC) simulation, the role of cytoplasm material properties, constant/sinusoidal forcing rates and various frequencies on the overall mechanical response of a cell was obtained. Numerical results are validated against experiments results. Micropipette aspiration simulation was also carried out in which the typical creep deformation test was carried out to study the viscoelastic behavior of the cell. Based on the results from finite element simulation, the effect of pipette radius, effect of cortex shear modulus and effect of pressure rate have been derived for the interpretation of the mechanical parameters from the micropipette aspiration.

ACKNOWLEDGEMENTS

I would like to thank my committee chair, Dr. Reddy, and my committee members, Dr. Jones, Dr. Gao, for their guidance and support throughout the course of this research.

Thanks also go to Dr. Ginu for his generous help in this research. I also want to extend my gratitude to my friends and colleagues and the department faculty and staff for making my time at Texas A&M University a great experience.

Finally, thanks to my grandmother and grandfather for their great love and encouragement on every step of my life.

TABLE OF CONTENTS

Page

ABSTRACT iii

ACKNOWLEDGEMENTS v

TABLE OF CONTENTS vi

LIST OF TABLES viii

LIST OF FIGURES ix

CHAPTER

I INTRODUCTION 1

A. Background 1

B. Motivations 2

C. Objective 6

II COMPUTIONAL MODELING OF BIOLOGICAL CELL 7

A. Introduction 7

B. Cell Physiology 7

C. Formulation of Constitutive Model 12

D. Modeling of Cortical Cytoplasm 14

E. Modeling of Inner Cytoplasm 21

F. Modeling of Nucleus 21

III FINITE ELEMENT ANALYSIS OF ATOMIC FORCE MICROSCOPY (AFM) FOR SINGLE LIVING CELL 22

A. Introduction 22

B. Material Constitutive Relation 23

C. FEM Analysis 25

D. Results 28

E. Conclusion 44

Page

CHAPTER

IV FINITE ELEMENT ANALYSIS OF MAGNETIC TWISTING CYTOMETRY (MTC) FOR SINGLE LIVING CELL 46

A. Introduction 46

B. Material Constitutive Relation 47

C. FEM Analysis 48

D. Results and Discussion 50

E. Conclusion 72

V FINITE ELEMENT ANALYSIS OF MICROPIPETTE ASPIRATION FOR SINGLE LIVING CELL 73

A. Introduction 73

B. Material Constitutive Relation 74

C. FEM Analysis 75

D. Results and Discussion 77

E. Conclusion 92

VI CONCLUSIONS 93

A. Summary 93

B. Future Works 94

REFERENCES 96

VITA 101

LIST OF TABLES

Page

Table 2.1 Storage shear modulus for the cases of concentration factor c=0.2, 0.3, 0.5, 1, 2mg/ml and frequency f=10, 100, 1000, 10000Hz 20

Table 2.2 Loss shear modulus for the cases of concentration factor c=0.2, 0.3, 0.5, 1, 2mg/ml and frequency f=10, 100, 1000, 10000Hz 20

LIST OF FIGURES

Page

Figure 1.1 Schematic representation of a generalized cell. 2

Figure 2.1 Stained image of bovine cell, green and red indicates cytoskeletal filaments and blue is the nucleus. 9

Figure 2.2 Mechanical behaviors of cytoskeletal filaments. 9

Figure 2.3 Mechanical analog of the standard linear solid model 15

Figure 3.1 Axisymmetric finite element model for a adherent cell. 26

Figure 3.2 Stress distribution obtained from finite element analysis for SLS model with shear modulus of cortex 275 Pa, cytoplasm 200Pa. 28

Figure 3.3 Strain distribution obtained from finite element analysis for SLS model with shear modulus of cortex 275 Pa, cytoplasm 200Pa. 29

Figure 3.4 Vertical displacement distribution obtained from finite element analysis for SLS model with shear modulus of cortex 275 Pa, cytoplasm 200Pa. 29

Figure 3.5 Force- deformation curves for the various cytoplasm shear modulus G=100Pa, 200Pa, 400Pa, 600Pa. (a) SLS model, (b) SnHS model. 31

Figure 3.6 Time vs. force curve for the case of: offset 0.2 μm, frequency 0.1 Hz and indenter velocity0.1 μm/s. (a) SLS model, (b) SnHS model. 32

Figure 3.7 Time vs. force curve for the case of: offset 0.2 μm, frequency 0.5 Hz and indenter velocity0.1 μm/s. (a) SLS model, (b) SnHS model. 33

Figure 3.8 Time vs. force curve for the case of: offset 0.2 μm, frequency 1 Hz and indenter velocity0.1 μm/s. (a) SLS model, (b) SnHS model. 34

Figure 3.9 Force-indentation curves for the case of: offset 0.2 μm, frequency 0.5 Hz and indenter velocity0.1 μm/s. (a) SLS model, (b) SnHS model. 35

Page

Figure 3.10 Force-indentation curves (SLS model) for the case of: offset 0.2 μm, frequency 1 Hz and indenter velocity0.1 μm/s. (a) SLS model, (b) SnHS model. 36

Figure 3.11 Indentation force deflection curves. (a) SLS model, (b) SnHS model. 37

Figure 3.12 Force time curves for entire time history, cortex G=275Pa, cytoplasm G=100Pa. (a) SLS model, (b) SnHS model.. 38

Figure 3.13 Indentation & force curves for various concentration factors under f=10Hz. 39

Figure 3.14 Indentation & force curves for various concentration factors under f=100Hz. 39

Figure 3.15 Indentation & force curves for various concentration factors under f=1000Hz. 40

Figure 3.16 Indentation & Force curves for various concentration factors under f=10000Hz. 40

Figure 3.17 Indentation & force curves for various frequencies with the concentration factor c=0.2mg/ml. 41

Figure 3.18 Indentation & force curves for various frequencies with the concentration factor c=0.5mg/ml. 41

Figure 3.19 Indentation & force curves for various frequencies with the concentration factor c=1mg/ml. 42

Figure 3.20 Indentation & force curves for various frequencies with the concentration factor c=2mg/ml. 42

Figure 3.21 V=0.1μm/s, displacement (input) and reaction force of indenter (output) for the entire time history 43

Figure 3.22 Force & indentation curve for various frequencies with the concentration factor c=2mg/ml. 43

Page

Figure 4.1 3-D finite element mesh of the cylindrical cell block selected for MTC simulation. The top of the actin cortical region having a thickness of 0.2 μm, and the part below forms the inner cytoplasm without nucleus..... 48

Figure 4.2 Distribution (3-D contours) of the amplitude of effective (von-Mises) stress for SLS model G=100 for both cortex and cytoplasm due to a lateral force 250pN. 50

Figure 4.3 Strain distribution (3-D contours) induced by bead displacement along 1-2 direction for SLS model G=100 Pa for both cortex and cytoplasm due to a lateral force 250pN. 51

Figure 4.4 Strain distribution (3-D contours) induced by bead displacement along 2-2 direction for SLS model G=100 Pa for both cortex and cytoplasm due to a lateral force 250pN. 51

Figure 4.5 The lateral displacement distribution (3-D contours) for SLS model G=100 Pa due to a lateral force 250pN 52

Figure 4.6 The vertical displacement distribution (3-D contours) for SLS model G=100 Pa due to a lateral force 250pN. 53

Figure 4.7 Bead center lateral displacement versus time, resulting from the SLS model with fixed forcing rate 100pN/s. 54

Figure 4.8 Bead center lateral displacement versus time, resulting from (a) SLS model and (b) SnHS model, for fixed forcing rate 250pN/s. 55

Figure 4.9 Bead center lateral displacement versus time, resulting from the SLS model fixed forcing rate 500pN/s..... 56

Figure 4.10 Bead center lateral displacement versus time, resulting from the SLS model with cortex shear modulus 100 Pa and cytoplasm shear modulus 100 Pa due to different force rates. 57

Figure 4.11 Bead center lateral displacement versus time, resulting from the SLS model with cortex shear modulus 100 Pa and cytoplasm shear modulus 200 Pa due to different force rates. 58

Page

Figure 4.12 Bead center lateral displacement versus time, resulting from the SLS model with cortex shear modulus 100 Pa and cytoplasm shear modulus 400 Pa due to different force rates. 58

Figure 4.13 Bead center lateral displacement versus time, resulting from the SLS model with cortex shear modulus 100 Pa and cytoplasm shear modulus 600 Pa due to different force rates 59

Figure 4.14 Bead center lateral displacement versus time, resulting from the SLS model with both cortex cytoplasm shear modulus 100 Pa under sinusoidal forcing amplitude 125pN with different frequencies. 60

Figure 4.15 Bead center lateral displacement versus time, resulting from the SLS model with cortex G=100 Pa and cytoplasm G= 200 Pa under sinusoidal forcing amplitude 125pN with different frequencies..... 61

Figure 4.16 Bead center lateral displacement versus time, resulting from the SLS model with cortex G=100 Pa and cytoplasm G= 400 Pa under sinusoidal forcing amplitude 125pN with different frequencies..... 61

Figure 4.17 Force versus bead center lateral displacement, resulting from the SLS model with cortex G=100 Pa and cytoplasm G= 100 Pa under sinusoidal forcing amplitude 125pN with different frequencies..... 62

Figure 4.18 Force versus bead center lateral displacement, resulting from the SLS model with cortex G=100 Pa and cytoplasm G= 200 Pa under sinusoidal forcing amplitude 125pN with different frequencies. 63

Figure 4.19 Force versus bead center lateral displacement, resulting from the SLS model with cortex G=100 Pa and cytoplasm G= 400 Pa under sinusoidal forcing amplitude 125pN with different frequencies. 63

Figure 4.20 Bead center lateral displacement versus time, resulting from the (a) SLS model and (b) SnHS model for fixed sinusoidal force amplitude 125pN with f=0.1Hz for various shear modulus. 65

Figure 4.21 Bead center lateral displacement versus time, resulting from the SLS model for fixed sinusoidal force amplitude 125pN with f=0.5Hz for various SLS model shear modulus..... 66

Page

Figure 4.22 Bead center lateral displacement versus time, resulting from the SLS model for fixed sinusoidal force amplitude 125pN with f=1Hz for various SLS model shear modulus..... 66

Figure 4.23 Force versus bead center lateral displacement, resulting from (a) SLS model and (b) SnHS model for fixed sinusoidal force amplitude 125pN with f=0.1Hz for various shear modulus. 67

Figure 4.24 Force versus bead center lateral displacement, resulting from the SLS model for fixed sinusoidal force amplitude 125pN with f=0.5Hz for various SLS model shear modulus..... 68

Figure 4.25 Force versus bead center lateral displacement, resulting from the SLS model for fixed sinusoidal force amplitude 125pN with f=1Hz for various SLS model shear modulus..... 68

Figure 4.26 Bead center lateral displacement versus time, resulting for SLS model with both cortex and cytoplasm shear modulus 100Pa under fixed frequency f=0.5Hz with various sinusoidal force amplitude. 69

Figure 4.27 Bead center lateral displacement versus time, resulting for SLS model with both cortex and cytoplasm shear modulus 100Pa under fixed frequency f=1Hz with various sinusoidal force amplitude. 70

Figure 4.28 Force versus bead center lateral displacement, resulting for SLS model with both cortex and cytoplasm shear modulus 100Pa under fixed frequency f=0.5Hz with various sinusoidal force amplitude. 70

Figure 4.29 Force versus bead center lateral displacement, resulting for SLS model with both cortex and cytoplasm shear modulus 100Pa under fixed frequency f=1Hz with various sinusoidal force amplitude. 71

Figure 5.1 The micropipette aspiration of a cell. R_c is the radius of the undeformed cell, R_p is the pipette radius, e is the fillet radius, L_p is the projection length, and L_c is the axial cell length, Δp is the sucking pressure..... 75

Figure 5.2 An axisymmetric finite element model for the cell. 76

Page

Figure 5.3 Stress distribution obtained from the finite element analysis of axisymmetric cell model due to pressure amplitude of 500Pa. (a) Rp*=0.25, (b) Rp*=0.4, (c) Rp*=0.5, (d) Rp*=0.6. 78

Figure 5.4 Strain distribution obtained from the finite element analysis of axisymmetric cell model due to pressure amplitude of 500Pa. (a) Rp*=0.25, (b) Rp*=0.4, (c) Rp*=0.5, (d) Rp*=0.6 79

Figure 5.5 Vertical displacement distribution obtained from the finite element analysis of axisymmetric cell model due to pressure amplitude of 500Pa. (a) Rp*=0.25, (b) Rp*=0.4, (c) Rp*=0.5, (d) Rp*=0.6. 80

Figure 5.6 Force-deformation curve of (a) SLS model and (b) SnHS model, with cortex G=200Pa, cytoplasm G=200Pa for various pipette radius. 82

Figure 5.7 Force-deformation curve of (a) SLS model and (b) SnHS model, with cortex G=400Pa, cytoplasm G=200Pa for various pipette radius. 83

Figure 5.8 Force-deformation curve (a) SLS model and (b) SnHS model, with cortex G=600Pa, cytoplasm G=200Pa for various pipette radius. 84

Figure 5.9 Force-deformation curve of (a) SLS model and (b) SnHS model, with various cortex shear modulus under pipette radius Rp*=0.25. 85

Figure 5.10 Force-deformation curve of (a) SLS model and (b) SnHS model, with various cortex shear modulus under pipette radius Rp*=0.4. 86

Figure 5.11 Force-deformation curve of (a) SLS model and (b) SnHS model, with various cortex shear modulus under pipette radius Rp*=0.6. 87

Figure 5.12 Creep deformation process for SLS model (solid line) and SnHS model (dash line) for the case of pressure 100Pa and the shear modulus of both of the cortex and cytoplasm is 200Pa. 88

Figure 5.13 Effect of pipette radius on creep deformation process, cortex shear modulus G=200P and p=300Pa. 89

Figure 5.14 Effect of pressure amplitude on creep deformation process, cortex shear modulus G=200Pa and Rp*=0.25. 90

Page

Figure 5.15 Effect of cortex shear modulus on creep deformation process, for fixed Rp*=0.25 and p=100Pa. 91

CHAPTER I

INTRODUCTION

A. Background

All living creatures, despite their profound diversity, share a common architectural building block: the cell. Cells are the basic functional units of life, yet are themselves comprised of numerous components with distinct mechanical characteristics. To perform their various functions, cells undergo or control a host of intra- and extracellular events, many of which involve mechanical phenomena which are guided by the external mechanical stimuli experienced by the cell. Cell mechanics describe and evaluate mechanical properties of cells and cellular structures and the mechanical interaction between cells and their environment [1].

Nowhere is the importance of biology in cell mechanics more evident than in the ability of the cell to sense and respond to externally applied forces. Perhaps all cells are able to sense when a physical force is applied to them. They respond through a variety of biological pathways that lead to such diverse consequences as changes in membrane channel activity, up- or- down- regulation of gene expression, alterations in protein synthesis, or altered cell morphology. One reason for the strong interest in mechanosensation is that many cells have shown that they can both sense and respond to a mechanical stimulus. While many of these responses appear designed to help the cell resist large deformations and possible structural damage, others have an undesirable out-

---

This thesis follows the style of Journal of Biomechanical Engineering.

come, including atherosclerosis, arthritis, and pulmonary hypertension. However, the detailed mechanism of mechanosensation is still not clearly understood, and is an active area of research involving experimental and theoretical works. Mathematical modeling of the mechanical stimulus correlating to different experimental stimulation procedures forms the first step leads to understanding the mechanosensation in cellular system.

B. Motivations

The main parts of a generalized cell, shown in Figure 1.1, are cellular membrane, cytoplasm, nucleus and organelles. The cytoplasm consists of biopolymer filaments called cytoskeleton which is a spatially sparse tangled matrix of rods and rod-like elements held together by smaller proteins. Actin, microtubule, and intermediate filaments are the three types of cytoskeletal polymers- actin filaments that maintain the cell structure.

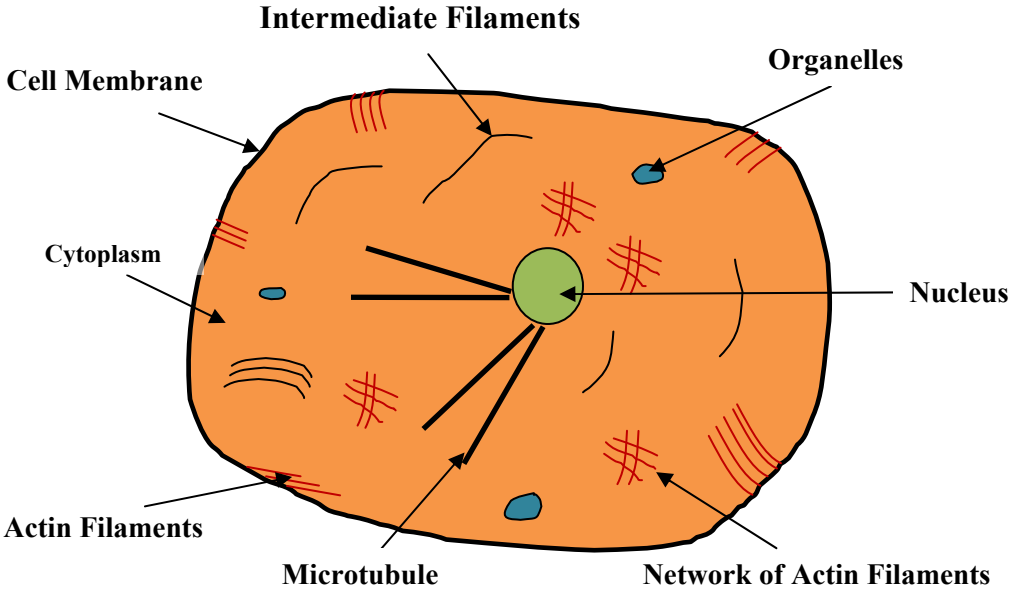

Figure 1.1 Schematic representation of a generalized cell.

Numerous experimental techniques have been developed to quantify cytoskeletal mechanics, typically involving a mechanical perturbation of the cell in the form of either an imposed deformation or force and observation of the static and dynamic responses of the cell. Novel methods to measure the viscoelasticity of soft materials and new theories relating these measurements to the underlying molecular structures have the potential to revolutionize our understanding of complex viscoelastic material like cytoplasm. Much of the progress in this field has been in methods to apply piconewton forces and to detect motion over distance of nanometers, thus performing mechanical manipulations on the scale of single- macromolecules and measuring the viscoelastic properties of volumes as small as fraction of a cell. Exogenous forces ranging from pN to nN are applied by optical traps, magnetic beads, glass needles, and atomic force microscope cantilevers, while deformations on a scale of nanometers to microns are measured by deflection of lasers onto optical detectors or by high resolution light microscopy. Complementary to the use of external forces to probe material properties of the cell are analyses of the thermal motion of refractile particles such as internal vesicles or submicron- sized beads imbedded within the cell. Measurements of local viscoelastic parameters are essential for mapping the properties of small but heterogeneous material like cytoplasm; some methods, most notably atomic force microscopy and optical tracking methods, enable high- resolution mapping of the cell's viscoelasticity.

A wide range of computational models also exist for cytoskeletal mechanics [2-4] which use to relate the experimental results. But these derived material properties vary by orders of magnitude, even for the same cell type. The main reason for such a disparity is due to the stimulation process and the different theoretical models used in interpreting the experimental data [5].

The roles of three types of cytoskeletal polymers- actin filaments, intermediate filaments, and microtubules, especially the actin stress fibers, in contribution to the mechanical properties of cells is well studied in literature [6-9]. And it is reported that the mechanical properties of the cells, like adhesion and viscoelastic nature, are depended on cytoskeletal frameworks .The changes caused by pathological conditions like malaria; aging and cancer on the cellular behavior have also been correlated to the structural and morphological changes in the cytoskeleton [10, 11]. Therefore, a precise representation of the anisotropic, nonlinear behavior of the cytoskeletal architecture is needed for computational analysis of living cell which can accurately capture inter-atomic and intermolecular interactions and cytoskeletal dynamics as the cytoskeletal network is altered by the disease state. This approach further leads to establish comprehensive connections between cell mechanics and chemical and biological cell functions in human health and disease which can provide novel and powerful developments for disease diagnostics, prophylactics and therapeutics.

It is well established that cells respond physiologically to mechanical stimuli. To explain how cells generate mechanical stresses in response to external mechanical stimuli (for example, deformations or forces), and how those stresses affect cellular functions, various models applicable to distinct type and functions of cell are available in the literature [7,21]. These cell models can be divided into two distinct classes: discrete models and continuum models.

Discrete cell models like the cellular tensegrity models [12], which represent the cell using a finite number of discrete elements, subjected to conditions of mechanical equilibrium and geometrical compatibility at every node. At this point, a coarse-graining average can be applied and local stresses and strain can be obtained as continuous filed variables. Although discrete models are very useful in study the static elastic behavior

of cells, they have limitation in describing and understanding cell dynamic viscoelastic behavior. Continuum based models assumes the cell satisfies the continuum hypotheses. A continuum cell model provides the displacement, strain, and stress fields induced in the cell, given its initial geometry and material properties, and the boundary conditions it is subjected to(such as displacements and forces applied on the cell surface). Laws of continuum mechanics are used to solve for the distribution of mechanical stress and deformation in the cell. Many continuum mechanical models in the literature [13-17] obtained their numerically solution via discretization of the cell volume into smaller computational cells using (for example) finite element techniques. Significant reasons for the popularity of finite element method are its efficiency, ease of computation, and speed of implementation. In addition, material as well as geometric nonlinearities can be easily incorporated. However, it should be mentioned that most of these works, based on continuum hypothesis, simply model the entire cell as mechanical elastic, viscoelastic, or poro-viscoelastic continuum, and do not explicitly consider the vastly different mechanical properties of the various parts of the cell, with some exceptions being the works of [3, 4, and 7].

Characteristic mechanical and material properties of cells have been experimentally obtained by considering response over a limited range of frequencies. Recent studies have indicated that the cytoskeleton response is governed by power law rheology over a broad frequency spectrum [18- 20]. The emergence of this relatively simple power law behavior for complex structure such as cytoskeleton and actin gels has motivated both theoretical and computational efforts to interpret these experimental observations. However, it should be noted that this computational model is phenomenological, and fails to provide any physical insight into the mechanism responsible for the emergence of this peculiar behavior of the cytoskeleton. To overcome

the limitations of these mathematical models, a continuum-based model capable of considering the different mechanical properties of various cellular components is proposed in this study.

C. Objective

The main objective of this dissertation is to develop a continuum-based computational framework for the mechanical behavior of cells. The different stages in the application of computational model to a complex system like biological cells are: a) Development of a mathematical model for the cellular behavior, b) Numerical solution of the mathematical model using finite element methods, c) Verification and implementation of the model to study cell behavior with results from literature.

The primary steps undertaken in the modeling of cells are as follows:

a. Identify primary cellular components responsible for the biomechanical behavior of cells.
b. Develop constitutive models of biological cells based on the mechanical properties of cellular components.
c. Implement the proposed constitutive models in the finite element analysis by atomic force microscopy (AFM), magnetic twisting cytometry (MTC) and Micropipette Aspiration.

This thesis is organized as follows. The development of mechanical formulations of main cellular components is given in Chapter II. The validation of the models using finite element analysis by atomic force microscopy (AFM), magnetic twisting cytometry (MTC) and Micropipette Aspiration are presented separately in Chapter III, IV and V. And at the end, the thesis concludes with a summary and future works in Chapter VI.

CHAPTER II

COMPUTIONAL MODELING OF BIOLOGICAL CELL

A. Introduction

Cell is the structural and functional unit of all known living organisms and has long been observed to sense and respond to external mechanical stimuli. Mathematical modeling of the mechanical stimulus correlating to different experimental stimulation procedures forms the first step leads to understanding the physiological behavior of cellular system.

Numerous experimental techniques and computational models have been developed to quantify cytoskeletal mechanics [1-3, 8]. The computational models can be divided into two classes- discrete models and continuum model. Both of them have their own limitations: discrete cell models are very useful in the study of the static elastic behavior of cells, but have limitation in describing and understanding cell dynamic viscoelastic behavior; while most of the works based on continuum hypothesis do not explicitly consider the vastly different mechanical properties of the various cellular components, but simply model the entire cell as mechanical elastic, viscoelastic, or poro-viscoelastic continuum. To overcome the limitations of these mathematical models, a continuum- based model capable of considering the different mechanical properties of various cellular components is proposed in this study.

B. Cell Physiology

The principal structural components of the cell are cytoplasm, cell membrane, and nucleus. The cell membrane is a selectively permeable lipid layer found in all cells.

Cytoplasm consists of fluid like cytosol containing organelles (mitochondria, nucleus, etc), the cytoskeleton, and a variety of other molecules. Cytoskeleton, which forms the biomechanical framework, is responsible for maintaining the structural integrity and also the distribution of forces in a cell. The organelles present in cytosol, except for the nucleus, do not contribute significantly to the structural integrity of a cell and are generally neglected in mechanical modeling of cell. The major components of cells are explained below.

1. **Cytoskeleton**

Cytoskeleton is a dynamic structure that maintains cell shape, protects the cell, enables cellular motion and plays important roles in both intracellular transport and cellular division. Cytoskeleton consists of three filaments: actin, intermediate filaments and microtubule distributed throughout the cytoplasm. Figure 2.1 [22] shows eukaryotic cell with the cytoskeleton, actin filaments which are shown in red, microtubules in green. It has been found experimentally that actin filament has higher stiffness than the microtubule, but fails at lower extensions The intermediate filaments have characteristics between the two (Figure 2.2) [22]. The interactions of the cytoskeleton with one another and with accessory proteins are responsible for the biological response of the cell.

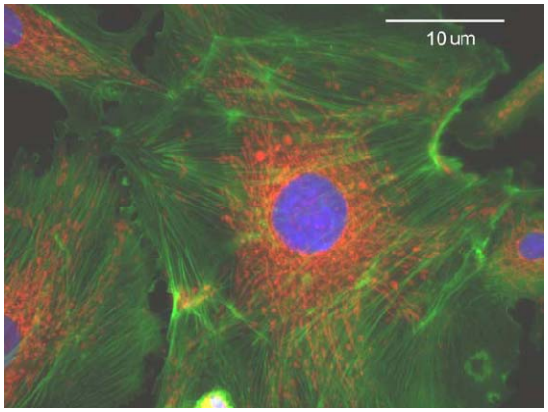

Figure 2.1 Stained image of bovine cell, green and red indicates cytoskeletal filaments and blue is the nucleus.

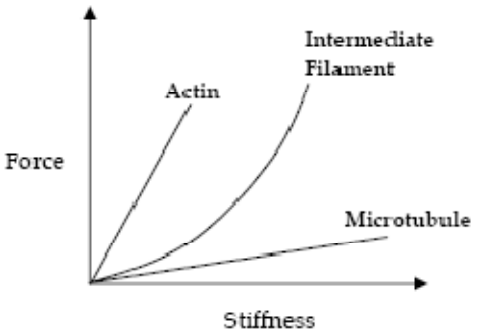

Figure 2.2 Mechanical behaviors of cytoskeletal filaments.

1.1. Actin Filament

The elementary actin filament building block is the protein G- actin ("G" for globular), a single chain of approximately 375 amino acids having a molecular mass of 42000Da. G-actin units can assembling into a long string called F-actin ("F" for filamentous). The filament has a width of about 8nm and a mass per unit length of 16000Da/nm. Typical actin monomer concentrations in the cell are 1-5 mg/ml. Two

important cellular structures are formed by actin filaments- actin cortex and stress fibers. Actin cortex is a three dimensional networks formed as a thick band below the plasma membrane providing additional strength to the membrane and responsible for cell surface movement. Actin stress fibers are sarcomeric-like structures based on both their protein composition and ability to contract. They are formed by the bundling of actin filaments through rigid connections in an adherent cell. The stress fibers originate from the cortical layer where it connects to the plasma membrane through focal points and either connects with another focal point or would end in a network of other cytoskeletal filaments. They act as structural regulators within the cells influencing cell behavior like adhesion and cell contraction [23].

1.2. Intermediate Filaments (IF)

Intermediate filaments are slightly wider than F-actin and have a more complex hierarchical structure. The basic building blocks of the filements are two protein chains intertwined as a helix. Pairs of helices lay side- by- side to form a linear protofilament some 2-3 nm in width. The intermediate itself is a bundle of eight protofilaments in a roughly cylindrical shape about 10 nm in diameter. The intermediate filament network envelopes the nucleus and is closely interconnected with the microtubule filaments extending throughout the cytoplasm. The primary function of intermediate filament is to provide mechanical stability to the cytoplasm and the nucleus.

1.3. Microtubules (MT)

The thickest individual filaments are microtubules of the protein tubulin, present as a heterodimer of α- tubulin and β- tubulin. Pairs of α- tubulin and β- tubulin form a unit 8 nm in length, and these units can assemble α to β successively into a hollow microtubule of 13 linear protofilaments. Unlike the intermediate filaments and the actin filaments, microtubule is distributed across the cytoplasm as individual filaments.

Microtubule acts as contractile members in the cytoskeleton, and besides providing structural stability, microtubules also act as pathways for the transfer of organelles inside the cytoplasm. They also help in the cellular division by forming a polarized region due to difference in the arrangement of α and β tubulin units. The Microtubule Binding Proteins, (MBPs) stabilize the organization of the microtubule and also acts as mediators in their interactions with other cell components.

Experimental and theoretical works have shown that the mechanical properties of the cells, like adhesion and viscoelastic nature, are depended on these cytoskeletal frameworks [24, 25]. The changes caused by pathological conditions like malaria; aging and cancer on the cellular behavior have also been correlated to the structural and morphological changes in the cytoskeleton [10]. Apart from the deformations, cell filaments are also constantly in the process of polymerization and depolymerization inducing additional changes in these load bearing components.

2. Cytosol and Organelles

The cytosol is a fluid medium in the cytoplasm (most of it is water, which makes up about 70% of a typical cell by volume). Cytosol consisting of the organelles and the cytoskeleton, aids in the biological response of the cell and preserves the incompressible nature of cell. The organelles present in cytosol, except for the nucleus, do not contribute significantly to the structural integrity of a cell. So these effects are not considered for computational analysis in most of the cases. Nucleus occupies a volume of nearly 20% of cytosol has a significant bearing on the behavior of the cell (see Figure 2.1). Structurally it can be considered as a single entity and experimentally it is 3-4 times stiffer and twice viscous than the cytoplasm [26, 27].

3. Cell Membrane

The cell membrane is a selectively permeable lipid layer found in all cells. It contains a wide variety of biological molecules, primarily proteins and lipids, which are involved in a vast array of cellular process such as cell adhesion and motion, ion channel conductance and cell signaling. The cell membrane also serves as the attachment point for both the intracellular cytoskeleton and, if present, the cell wall. Adhesion is achieved through a series of transmembrane proteins which connects the extra cellular matrix with the cytoskeleton. Movement of cell is achieved through the lamellipods and through a series of polymerization and depolymerization of cell skeleton.

C. Formulation of Constitutive Model

1. Mechanical Models of Cell

It is well established that cells respond physiologically to mechanical stimuli. To explain how cells generate mechanical stresses in response to external mechanical stimuli (for example, deformations or forces), and how those stresses affect cellular functions, various models applicable to distinct type and functions of cell are available in the literature [7, 21]. These cell models can be divided into two distinct classes: discrete models and continuum models.

Discrete cell models like the cellular tensegrity models [12], which represent the cell using a finite number of discrete elements, subjected to conditions of mechanical equilibrium and geometrical compatibility at every node. At this point, a coarse-graining average can be applied and local stresses and strain can be obtained as continuous filed variables. Although discrete models are very useful in study the static elastic behavior of cells, they have limitation in describing and understanding cell dynamic viscoelastic

behavior. Continuum based models assumes the cell satisfies the continuum hypotheses. A continuum cell model provides the displacement, strain, and stress fields induced in the cell, given its initial geometry and material properties, and the boundary conditions it is subjected to(such as displacements and forces applied on the cell surface). Laws of continuum mechanics are used to solve for the distribution of mechanical stress and deformation in the cell. Many continuum mechanical models in the literature [13-17] obtained their numerically solution via discretization of the cell volume into smaller computational cells using (for example) finite element techniques. Significant reasons for the popularity of finite element method are its efficiency, ease of computation, and speed of implementation. In addition, material as well as geometric nonlinearities can be easily incorporated. However, it should be mentioned that most of these works, based on continuum hypothesis, simply model the entire cell as mechanical elastic, viscoelastic, or poro-viscoelastic continuum, and do not explicitly consider the vastly different mechanical properties of the various parts of the cell, with some exceptions being the works of [3, 4, and 7].

Characteristic mechanical and material properties of cells have been experimentally obtained by considering response over a limited range of frequencies. Recent studies have indicated that the cytoskeleton response is governed by power law rheology over a broad frequency spectrum [18- 20]. The emergence of this relatively simple power law behavior for complex structure such as cytoskeleton and actin gels has motivated both theoretical and computational efforts to interpret these experimental observations. However, it should be noted that this computational model is phenomenological, and fails to provide any physical insight into the mechanism responsible for the emergence of this peculiar behavior of the cytoskeleton. To overcome the limitations of these mathematical models, a continuum-based model capable of

considering the different mechanical properties of various cellular components is proposed in this study.

2. Theoretical Formulation

As we discussed in the section of Cell Physiology, a generalized cell can be divided into three distinct layers: an outer cortical layer- cortex, formed by the actin filament networks; inner cytoplasmic region, and the nucleus. Most of the previous works on continuum based constitutive modeling simply model the entire cell as mechanical elastic, viscoelastic, or poro-viscoelastic continuum. However, such simplifications limit the applicability of the model in connecting the physiological phenomenon with the mechanical properties of the cell. For example, when a cell is attached to a substrate, the mechanical properties are changed due to the formation of stress fibers, a fact that cannot be explained with the simple continuum cell models. To overcome such a limitation, a constitutive model capable of consider the vastly different mechanical properties of the various cellular components is developed in this work. Using the continuum based viscoelastic theory and trying to introduce polymer mechanics into the model to describe actin dynamic mechanical behavior, modeling of the actin cortex and the cytoplasm with the nucleus as an inclusion is outlined next.

D. Modeling of Cortical Cytoplasm

The actin cortex region is modeled as a viscoelastic material by assuming the cortical region to be of an isotropic distribution of the actin network filaments.

1. Standard Linear Solid Viscoelasticity

In the integral form of linear viscoelasticity, the stress is expressed in terms of the strain history as

$$\mathbf{S}(t) = \int_{-\infty}^{t} G(t-s)\dot{\boldsymbol{\varepsilon}}(s)ds \tag{2.1}$$

$$\boldsymbol{\varepsilon} = \nabla\mathbf{u} + \nabla\mathbf{u}^T \quad \dot{\boldsymbol{\varepsilon}} = \nabla\mathbf{v} + \nabla\mathbf{v}^T \quad \mathbf{S} = \boldsymbol{\sigma} + p\mathbf{I} \tag{2.2}$$

where $\mathbf{S}$ is the deviatoric stress tensor, t is the current time, $G(t)$ is the time-dependent shear relaxation modulus, $\boldsymbol{\varepsilon}$ is the engineering strain tensor, which is the same as the deviatoric component under the condition of incompressibility, $\dot{\boldsymbol{\varepsilon}}$ is the engineering strain rate tensor, $\mathbf{u}$ is the displacement field, $\mathbf{v}$ is the velocity field, $\boldsymbol{\sigma}$ is the total stress tensor, p is the hydrostatic pressure and $\mathbf{I}$ is the unit tensor.

For the standard linear solid model, the shear relaxation modulus $G(t)$ can be expressed as a *Prony series* expansion with the first term

$$G(t) = G_0[1 - g_1(1 - e^{-t/\lambda_1})] \tag{2.3}$$

The relationship between the two sets of viscoelastic parameters in the differential form Eq. (2.3) and integral form Eq. (2.1) can be derived as

$$G_0 = k_1 + k_2, g_1 = \frac{k_2}{k_1 + k_2}, \lambda_1 = \frac{\mu}{k_2} \tag{2.4}$$

The mechanical analog of the SLS model is shown in Figure 2.3.

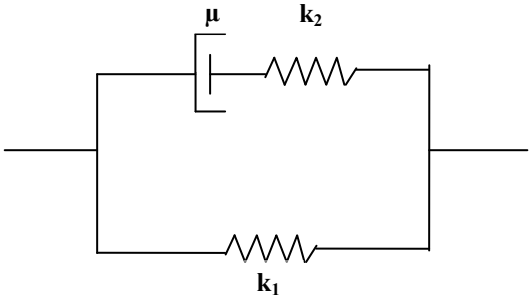

Figure 2.3 Mechanical analog of the standard linear solid model.

2. Standard Neo- Hookean Solid Viscoelasticity

Generally, the SLS model is applied to small strain analysis because of the use of small strain tensor and many cytomechanical experiments involve large strain without breaking the cell. Thus it is necessary to apply large strain constitutive law for describing cellular material. The neo-Hookean hyperelastic model is a natural extension of the linear elastic model. The neo-Hookean hyperelastic model reduces to the linear model for small deformation and does not deviate far from the linear elastic model at large deformation.

The hyperelastic material model utilizes a general strain energy potential to describe the material behavior at finite strain for incompressible rubber-like materials. The incompressible neo-Hookean constitutive law is the simplest hyperelastic model and is characterized by only one parameter, the shear modulus G_0. The strain energy density function of an incompressible Neo-Hookean material is

$$U = \frac{G_0}{2}(I_1 - 3) \tag{2.5}$$

where I_1 is the deviatoric strain invariant, defined as

$$I_1 = \lambda_1^2 + \lambda_2^2 + \lambda_3^2 \tag{2.6}$$

with $\lambda_1, \lambda_2, \lambda_3$ being the principal stretches. From the virtual work principle, it can be deduced that

$$\begin{aligned} \mathbf{S} &= G_0\left(\mathbf{B} - \frac{1}{3}I_1 \cdot \mathbf{I}\right) \\ \mathbf{B} &= \mathbf{F}\cdot\mathbf{F}^T, \mathbf{F} = \frac{\partial \mathbf{x}}{\partial \mathbf{X}} \end{aligned} \tag{2.7}$$

where **S** is the deviatoric part of the Cauchy stress tensor, G_0 is the shear modulus, **F** is the deformation gradient of the current configuration **x** relative to the initial configuration **X**, and **B** is the left Cauchy-Green strain tensor.

The SnHS viscoelasticity is a natural extension of the SLS viscoelasticity. The relaxation modulus of the SnHS model is essentially the same as Eq. (2.3) in form, whereas the deviatoric part of the Cauchy stress tensor is

$$\begin{aligned}\mathbf{S}(t) &= \mathbf{S}_0(t) + \mathrm{SYM}\left[\int_0^t \frac{\dot{G}(s)}{G_0}\mathbf{F}_t^{-1}(t-s)\cdot\mathbf{S_0}(t-s)\cdot\mathbf{F}_t(t-s)ds\right] \\ \mathbf{F_t}(t-s) &= \frac{\partial\mathbf{x}(t-s)}{\partial\mathbf{x}(t)}\end{aligned} \tag{2.8}$$

where $\mathbf{F_t}(t-s)$ is the deformation gradient of the configuration $\mathbf{x}(t-s)$ at $t-s$, relative to the configuration $\mathbf{x}(t)$ at time t, and $\mathbf{S}_0(t)$ represents the instantaneous stress caused by the deformation, which can be computed using Eq. (2.7), SYM[.] denotes the symmetric part of a matrix. This constitutive equation is applicable to large deformation analysis because the instantaneous elastic behavior is governed by the neo-Hookean hyperelasticity instead of the linear elasticity.

Some of the assumptions made for the SLS and SnHS model are as follows:

a. The material properties are assumed to be constant and adequately described by the homogeneous incompressible standard neo-Hookean solid model.
b. The viscosity and osmolarity of the surrounding fluid as well as temperature effects have been neglected.
c. Neglect the local inhomogeneity in the probing area.

3. Dynamic Shear Modulus Viscoelastic Model

From another point of view, the actin filaments network of cortical cytoplasm/cortex can also be considered as a semi-flexible polymer network. F. Gittes and F. C. MacKintosh in [28] construct a model for the dynamic shear modulus $G(\omega)$ of entangled or crosslinked networks of semi-flexible polymer that can account for the high-frequency scaling behavior, $G(\omega) \sim \omega^{3/4}$ has been observed in solutions of the biopolymer F-actin. They also report molecular dynamics simulations that support the single filament response that is the basis of their model for the network shear modulus.

For a strain $u_{ij} = \frac{1}{2}\left(\nabla_i u_j + \nabla_j u_i\right)$, a segment of orientation $\hat{n}$ and l length undergoes a relative change in end-to-end length of $\delta l / l = n_i n_j u_{ij}$, and there will be an induced tension τ_ω , given by $\delta l_\omega = \alpha_\omega \tau_\omega$, where $\alpha_\omega = \alpha_\omega' + i\alpha_\omega''$ is the longitudinal response function of the segment of filament. For a spatial density ρ of filaments, the stress due to filament tension is

$$\sigma_{ij}^{(\tau)} = \rho\left\langle \tau n_i n_j \right\rangle = \frac{\rho l_e}{\alpha_\omega}\left\langle n_i n_j n_k n_l \right\rangle u_{kl} \tag{2.9}$$

There is an additional stress $-2i\omega\eta u_{ij}$ due to the solvent (with η the viscosity). For an isotropic distribution of filaments, $\left\langle n_i n_j n_k n_l \right\rangle = \frac{1}{15}\left\{\delta_{ij}\delta_{kl} + \delta_{ik}\delta_{jl} + \delta_{il}\delta_{jk}\right\}$. Assuming incompressibility ($u_{ij} = 0$) and identifying $\sigma_{ij} \equiv 2G(\omega)u_{ij}$, one finds

$$G(\omega) = \frac{\rho l_e}{15\alpha_\omega} - i\omega\eta \tag{2.10}$$

We defined α_ω as the response of a fluctuating segment of inextensible filament to tension $\tau(t)$, from [29] and [30] we obtain the end-to-end response function of a segment of inextensible filament,

$$\alpha_\omega = \frac{1}{Tq_1^4 l_p^2}\sum_{n=1}^{\infty}\frac{1}{n^4 - i\omega/2\omega_1} \tag{2.11}$$

where $\omega_1 = (\kappa/\varsigma)(\pi/l_e)^4$ is the relaxation rate of the slowest mode, $q = q_1 = \pi / l$. The imaginary part α_ω'' is given by the fluctuation-dissipation theorem $\alpha_\omega'' = (\omega/2T)(\delta l^2)_\omega$. Replacing the sum in Eq. (2.11) by an integral to find

$$\alpha_\omega \approx \frac{1}{2\sqrt{2}} \frac{l}{Tl_p^2} \left(\frac{2\kappa}{-i\varsigma\omega} \right)^{3/4} \quad (\omega \gg \omega_1) \tag{2.12}$$

Again using Eq. (2.10), we find the shear modulus at high frequencies ($\omega \gg \omega_1$),

$$G(\omega) \approx \frac{1}{15} \rho\kappa l_p (-2i\varsigma / \kappa)^{3/4} \omega^{3/4} - i\omega\eta \tag{2.13}$$

The scaling response depends solely on the density of filaments, their bending stiffness and their lateral drag coefficient. In the case of F-actin, each actin filament contains fourteen 43-kD monomers per 38-nm half-pitch; it follows that the density of filament length in 1mg/ml polymerized F-actin is $\rho = 3.8 \times 10^{13}\,\mathrm{m}^{-2}$.

From [28, 31], assuming persistence length of 17 μm , with a mesh size ξ 0.19 μm , the diameter of the filament $d \approx 5\mathrm{nm}$, the linear elastic modulus is calculated as 275 Pa for small strain, then

$$\begin{aligned} \kappa &= \frac{275}{(17)^{2/5}(0.19)^{-22/5}} = 0.0594, \\ \zeta &= 4\pi\eta / \ln(0.6\lambda / d) \approx 0.0023. \end{aligned} \tag{2.14}$$

Substitute Eq. (2.16) into Eq. (2.13), we have

$$G(f) \approx (1.6\mathrm{Pa}) \left(\frac{c_A}{1\mathrm{mg/ml}} \right) \left(\frac{f}{1\ \mathrm{Hz}} \right)^{3/4} i^{-3/4} \tag{2.15}$$

The equivalent form for storage and loss modulus of Eq. (2.14) is,

$$\begin{aligned} &G(f) \approx (1.6\mathrm{Pa}) \left(\frac{c_A}{1\mathrm{mg/ml}} \right) \left(\frac{f}{1\mathrm{Hz}} \right)^{3/4} \cdot (0.3827 - 0.9239\mathrm{i}) = G'(f) - G''(f)\mathrm{i} \\ &G'(f) = 0.6123 \left(\frac{c_A}{1\mathrm{mg/ml}} \right) \left(\frac{f}{1\mathrm{Hz}} \right)^{3/4} \mathrm{Pa}, \quad G''(f) = 1.4782 \left(\frac{c_A}{1\mathrm{mg/ml}} \right) \left(\frac{f}{1\mathrm{Hz}} \right)^{3/4} \mathrm{Pa} \end{aligned} \tag{2.16}$$

Table 2.1 and Table 2.2 show the storage shear modulus and loss shear modulus for various concentration factors and frequencies respectively. Identical conclusions

have been obtained independently by Morse [32]. This scaling of $G(\omega)$ is in good agreement with prior results of F-actin by microrhelogy [33] experiments.

Table 2.1 Storage shear modulus for the cases of concentration factor c=0.2, 0.3, 0.5, 1, 2mg/ml and frequency f=10, 100, 1000, 10000Hz

G'(Pa)				
	f=10Hz	f=100Hz	f=1000Hz	f=10000Hz
c=0.2mg/ml	0.6886	3.8725	21.7768	122.5
c=0.3mg/ml	1.033	5.8088	32.6652	183.7
c=0.5mg/ml	1.7216	9.6813	54.442	306.1
c=1mg/ml	3.4432	19.3626	108.884	612.3
c=2mg/ml	6.8864	38.7253	217.7681	1224.6

Table 2.2 Loss shear modulus for the cases of concentration factor c=0.2, 0.3, 0.5, 1, 2mg/ml and frequency f=10, 100, 1000, 10000Hz

G''(Pa)				
	f=10Hz	f=100Hz	f=1000Hz	f=10000Hz
c=0.2mg/ml	1.6625	9.349	52.5731	295.6
c=0.3mg/ml	2.4938	14.0234	78.8596	443.5
c=0.5mg/ml	4.1563	23.3724	131.4326	739.1
c=1mg/ml	8.3125	46.7448	262.8653	1478.2
c=2mg/ml	16.6251	93.4896	525.7305	2956.4

E. Modeling of Inner Cytoplasm

Cytoplasm is composed of an organized network of cytoskeletal filaments of actin, intermediate filaments and microtubules. Therefore, here we also model the cytoplasm as viscoelastic material using Standard Linear Solid Model (SLS) and Standar neo-Hookean Solid Model (SnHS) which we mentioned in the previous section. Since the distribution of the cytoskeletal filaments alters according to the type and environment of the cell, the material properties of cell vary respectively. For example, the form of stress fibers due to cell adhesion will lead to the change of material properties of cell. To take this characteristic into consideration, a study on the effect of various subcellular material properties to the overall mechanical behavior of cell is also conducted in this study.

F. Modeling of Nucleus

The nucleus has generally been found to be stiffer and more viscous than the cytoplasm. Probing isolate chondrocyte nuclei with micropipette aspiration [34] found nuclei to be 3-4 times stiffer and nearly twice as viscous as the cytoplasm. Its higher viscosity results in a slower time scale of responses, so that the nucleus can often be considered as elastic, even when the rest of the cell requires viscoelastic modeling.

CHAPTER III

FINITE ELEMENT ANALYSIS OF ATOMIC FORCE MICROSCOPY (AFM) FOR SINGLE LIVING CELL

A. Introduction

The atomic force microscope (AFM) is a very high-resolution type of scanning probe microscope with demonstrated resolution of fractions of a nanometer. The precursor to the AFM, the scanning tunneling microscope, was developed by Gerd Binnig and Heinrich Rohrer in the early 1980s, a development that earned them the Nobel Prize for Physics in 1986 [35]. The AFM is one of the foremost tools for imaging, measuring, manipulating matter at the nanoscale, and is widely accept in the area of cell mechanics due to its high quality of derivable structural and functional information.

The AFM consists of a microscale cantilever with a sharp tip (probe) at its end which is used to scan the specimen surface. The cantilever is typically silicon or silicon nitride with a tip radius of curvature in the order of nanometers. When the tip is brought into proximity of a sample surface, forces between the tip and the sample lead to a deflection of the cantilever which can be described using Hooke's law. Typically, the deflection is measured using a laser spot reflected from the top of the cantilever into an array of photodiodes.

In this chapter, an axisymmetric viscoelastic finite element model is developed for cell micromanipulation by atomic force microscopy (AFM). For the material modeling, standard linear solid (SLS) model and its natural extension standard neo-Hookean solid (SnHS) model, as well as a polymer mechanics based dynamic shear modulus model are introduced in this study.

B. Material Constitutive Relation

A generalized cell can be divided into three distinct layers: an outer cortical layer formed by the actin filament networks (cortex), an inner cytoplasmic region, and the nucleus.

1. Modeling of Actin Cortex

1.1 Standard Linear Solid Model (SLS) and Neo-Hookean Solid Model (SnHS)

In the integral form of linear viscoelasticity, the stress is expressed in terms of the strain history as

$$\mathbf{S}(t) = \int_{-\infty}^{t} G(t-s)\dot{\boldsymbol{\varepsilon}}(s)ds \tag{3.1}$$

$$\boldsymbol{\varepsilon} = \nabla\mathbf{u} + \nabla\mathbf{u}^T \quad \dot{\boldsymbol{\varepsilon}} = \nabla\mathbf{v} + \nabla\mathbf{v}^T \quad \mathbf{S} = \boldsymbol{\sigma} + p\mathbf{I} \tag{3.2}$$

The SnHS viscoelasticity is a natural extension of the SLS viscoelasticity. The relaxation modulus of the SnHS model is essentially the same as Eq. (3.1) in form, whereas the deviatoric part of the Cauchy stress tensor is

$$\mathbf{S}(t) = \mathbf{S}_0(t) + \mathrm{SYM}\left[\int_0^t \frac{\dot{G}(s)}{G_0}\mathbf{F}_t^{-1}(t-s)\cdot\mathbf{S_0}(t-s)\cdot\mathbf{F}_t(t-s)ds\right]$$
$$\mathbf{F_t}(t-s) = \frac{\partial\mathbf{x}(t-s)}{\partial\mathbf{x}(t)} \tag{3.3}$$

For the SLS and SnHS, the shear relaxation modulus $G(t)$ can be expressed as a Prony series expansion with the first term

$$G(t) = G_0[1 - g_1(1 - e^{-t/\lambda_1})] \tag{3.4}$$

The relationship between the two sets of viscoelastic parameters in the differential form can be derived as,

$$G_0 = k_1 + k_2, g_1 = \frac{k_2}{k_1 + k_2}, \lambda_1 = \frac{\mu}{k_2} \tag{3.5}$$

The mechanical parameters for SLS and SnHS model are derived as [3, 13],

$$G_0 = 200\text{Pa}, 275\text{Pa}, g_1 = 0.9, \lambda_1 = 0.1\text{s}$$

1.2.Dynamic Shear Modulus Model

For the high frequency behavior of cortex, using the method discussed in Chapter II [28]:

$$G(f) \approx (1.6\text{Pa})\left(\frac{c_A}{1\text{mg/ml}}\right)\left(\frac{f}{1\text{ Hz}}\right)^{3/4} i^{-3/4}. \tag{3.6}$$

We have the equivalent form for storage and loss modulus of Eq. (3.6) is,

$$\begin{aligned} G(f) &\approx (1.6\text{Pa})\left(\frac{c_A}{1\text{mg/ml}}\right)\left(\frac{f}{1\text{Hz}}\right)^{3/4} \cdot (0.3827 - 0.9239\text{i}) = G'(f) - G''(f)\text{i} \\ G'(f) &= 0.6123\left(\frac{c_A}{1\text{mg/ml}}\right)\left(\frac{f}{1\text{Hz}}\right)^{3/4} \text{Pa}, \\ G''(f) &= 1.4782\left(\frac{c_A}{1\text{mg/ml}}\right)\left(\frac{f}{1\text{Hz}}\right)^{3/4} \text{Pa} \end{aligned} \tag{3.7}$$

And then the material properties can be calculated as Table 2.1 and Table 2.2:

G'(Pa)				
	f=10Hz	f=100Hz	f=1000Hz	f=10000Hz
c=0.2mg/ml	0.6886	3.8725	21.7768	122.5
c=0.3mg/ml	1.033	5.8088	32.6652	183.7
c=0.5mg/ml	1.7216	9.6813	54.442	306.1
c=1mg/ml	3.4432	19.3626	108.884	612.3
c=2mg/ml	6.8864	38.7253	217.7681	1224.6

G"(Pa)				
	f=10Hz	f=100Hz	f=1000Hz	f=10000Hz
c=0.2mg/ml	1.6625	9.349	52.5731	295.6
c=0.3mg/ml	2.4938	14.0234	78.8596	443.5
c=0.5mg/ml	4.1563	23.3724	131.4326	739.1
c=1mg/ml	8.3125	46.7448	262.8653	1478.2
c=2mg/ml	16.6251	93.4896	525.7305	2956.4

2. Modeling of Inner Cytoplasm

For the cytoplasm, the material model was also assumed as Standard Linear Solid model (SLS) and Standard neo-Hookean Solid model (SnHS).

The mechanical parameters for the SLS and SnHS model are derived as

$$G_0 = k_1 + k_2 = 200\text{Pa}, 400\text{Pa}, 600\ \text{Pa}, \quad g_1 = \frac{k_2}{k_1 + k_2} = 0.9, \quad \lambda_1 = \frac{\mu}{k_2} = 1\text{s}$$

C. FEM Analysis

1. Model Geometry

The cell geometry considered is 3.5 μm in half width, 3.0 μm in height, with a nucleus 0.9 μm diameter at a height of 0.75 μm from the base. The cortical region is assumed to be 0.2 μm thick and the cross section of the cell is shown in Figure 3.1 The cell is the considered as axisymmetric with a rigid spherical indenter (acting on the top of the cell surface.

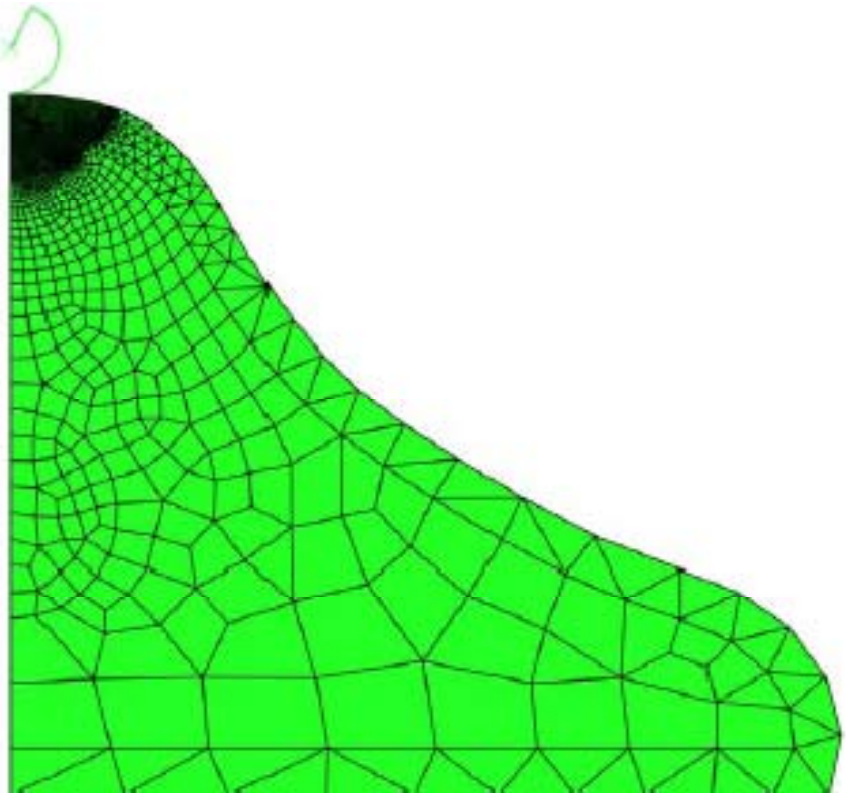

Figure 3.1 Axisymmetric finite element model for an adherent cell.

All simulations were performed using a commercially available finite element modeling software ABAQUS. To accurately capture details of deformation and the associated stress and strain patterns, a finer mesh is employed towards the bead region. The finite element model consists of 3453 nodes with 3536 CAX3 elements.

2. Boundary Conditions

Displacement boundary conditions are applied on the indenter and also at the base of the cell, while symmetric boundary conditions are taken along the axis of symmetry. The cell base is constrained in all directions to assume a perfect contact with the substrate.

3. Applied Load

Constant and sinusoidal velocities (or force) have been applied to the bead center while the typical strain-relaxation test has also been conducted to study the viscoelastic material properties of the cell.

a. For the constant velocity, the velocity was applied 0.1μm/s for 3.5s to give the relationship between force and indentation.
b. For the sinusoidal velocities, initial velocity of 0.1μm/s was applied for 2s to give an offset in order to give the adhesion depth and then velocity with the amplitude 0.1μm and frequencies 0.1 Hz, 0.5 Hz and 1 Hz have been applied to the bead center to obtain the frequency domain dynamic mechanical properties of the cell.
c. For the strain-relaxation test, also initial velocity of 0.1μm/s was applied to give an offset, and then removed from the bead to conduct the relaxation process.

D. Results

1. Results for SLS Model and SnHS Model

1.1. Stress, Strain and Displacement Distribution

The stress, strain and displacement in distribution of the cell subjected to an indentation of 0.5 μm is shown in Figure 3.2-Figure 3.4. The actin cortical layer, which is in direct contact with the indenter, sustains the maximum deformation. The inner cytoplasm near the region of indentation also experiences very high strains and the intensity decreases away from the center. The total reaction force acting on the indenter is calculated by considering the horizontal and vertical reaction forces at the reference point of the rigid indenter.

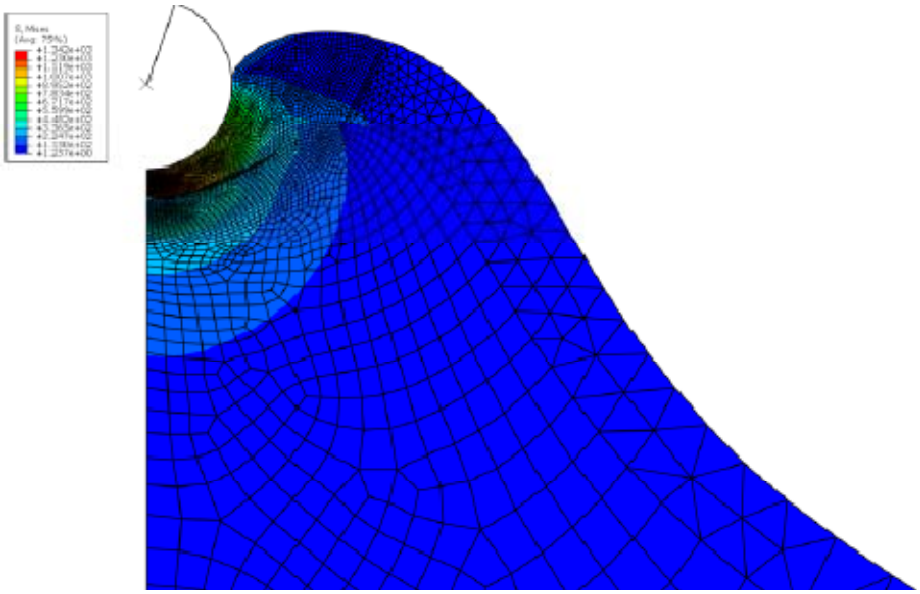

Figure 3.2 Stress distribution obtained from finite element analysis for SLS model with shear modulus of cortex 275 Pa, cytoplasm 200Pa.

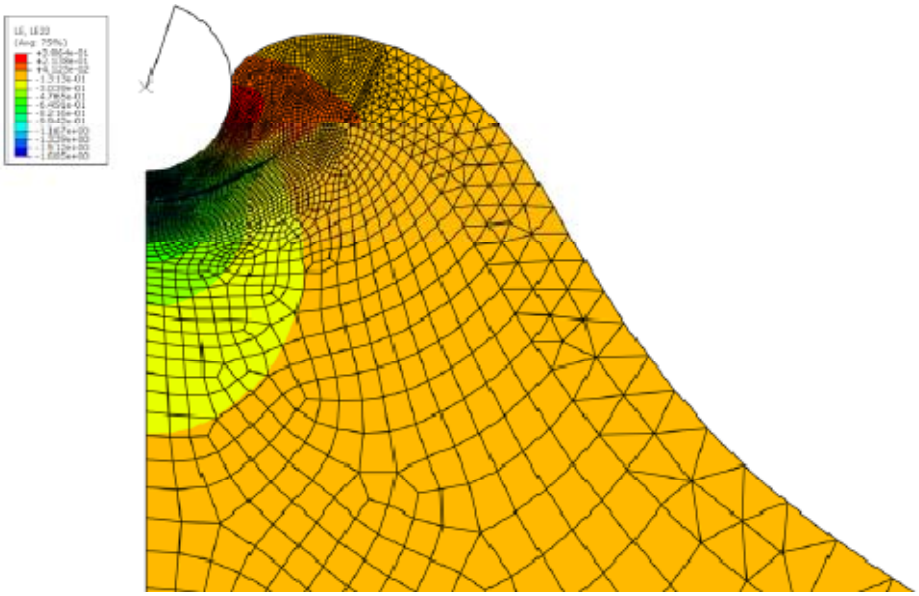

Figure 3.3 Strain distribution obtained from finite element analysis for SLS model with shear modulus of cortex 275 Pa, cytoplasm 200Pa.

.

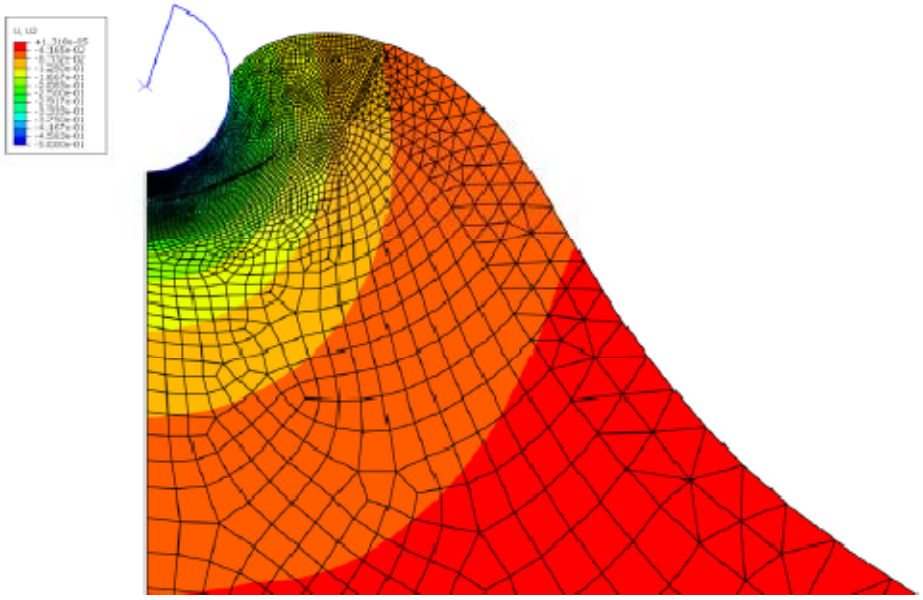

Figure 3.4 Vertical displacement distribution obtained from finite element analysis for SLS model with shear modulus of cortex 275 Pa, cytoplasm 200Pa.

1.2. Fore-Displacement Relationship

As was discussed in Chapter II, the material property of the cytoplasm varies as the formation of stress fiber during cell adhesion. In AFM simulation, cell is assumed to adherent to a surface and has the fixed displacement boundary condition, in which case the stress fiber will form during the process. Therefore, by changing the shear modulus of cytoplasm, influence of it to the overall mechanical properties of the cell was studied. The results for SLS model and SnHS model are nearly the same, as seen in Figure 3.5 (a) and (b), and it is found that for the fixed indentation, the reaction force increases as the shear modulus of cytoplasm increase. Also the force-indentation curve of higher shear modulus shows higher nonlinearity.

1.3. Application of Sinusoidal Force

To study the frequency dependence of the dynamic viscoelastic behavior of the cell, sinusoidal loads with different frequencies have been applied to the bead center. The results show that bead displacement under sinusoidal loading also exhibits an oscillatory behavior. Again, the results for SLS model and SnHS model are very similar, and in both cases the reaction force scales approximately with the shear modulus of cytoplasm while inverse of the frequencies, see Figure 3.6-Figure 3.8. Also for the same offset 0.2 μm, reaction force increase as the shear modulus of cytoplasm increases, this explains the ellipses do not have the same center, as seen in Figure 3.9 and 3.10. And the phase lag between the force and indentation also increases as the rise of shear modulus of cytoplasm while decreases as frequency increases.

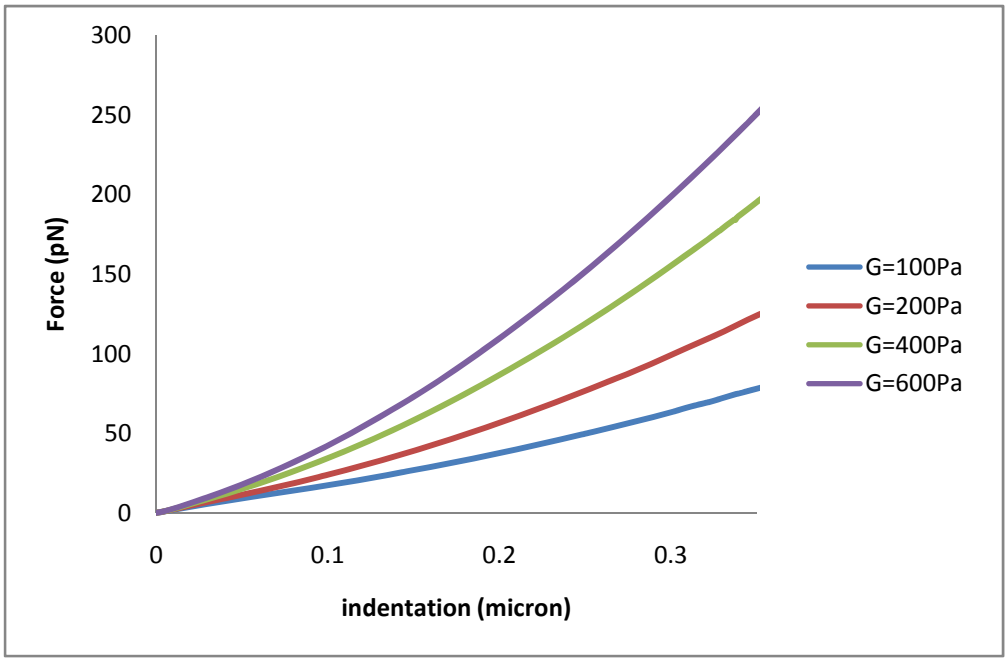

(a)

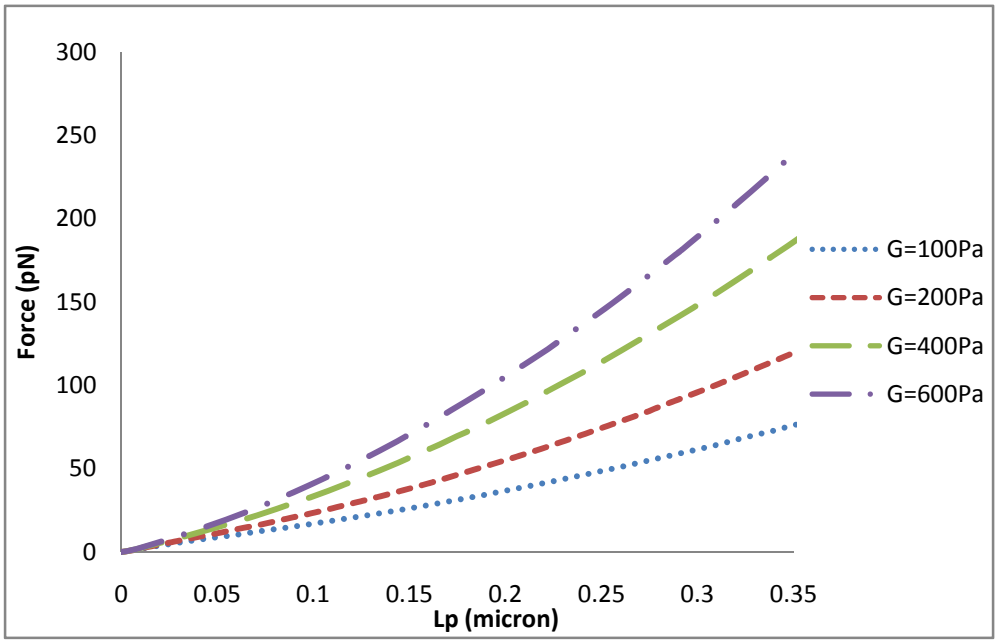

(b)

Figure 3.5 Force- deformation curves for the various cytoplasm shear modulus G=100Pa, 200Pa, 400Pa, 600Pa. (a) SLS model, (b) SnHS model.

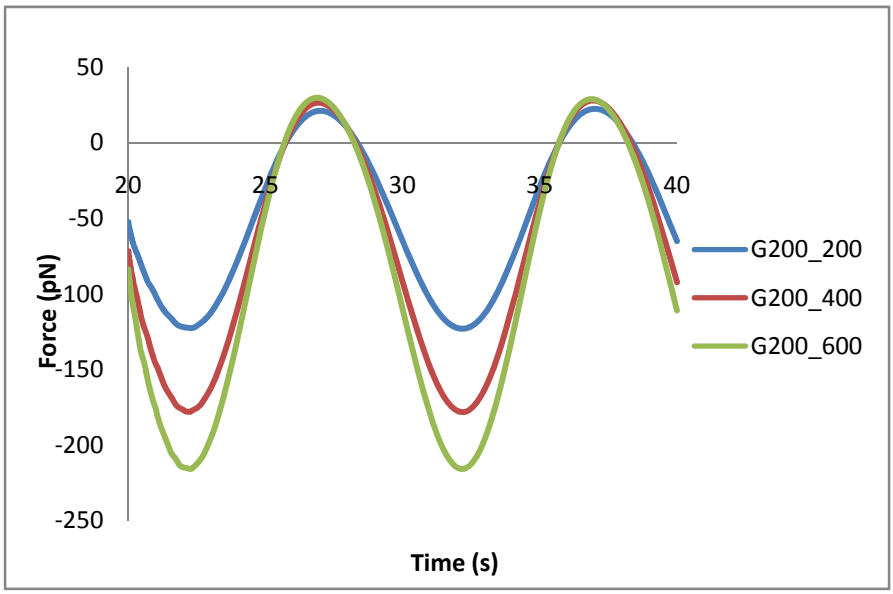

(a)

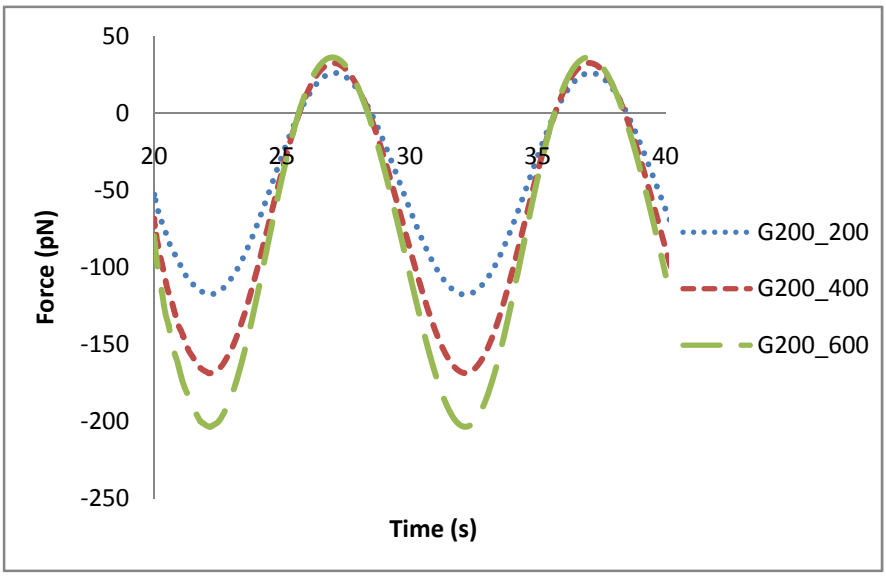

(b)

Figure 3.6 Time vs. force curve for the case of: offset 0.2 µm, frequency 0.1 Hz and indenter velocity0.1 µm/s. (a) SLS model, (b) SnHS model.

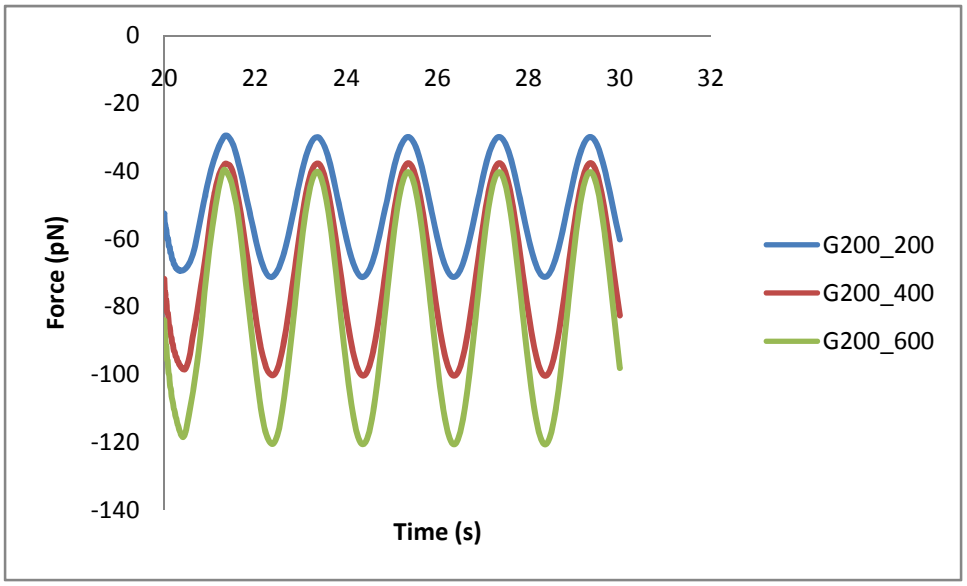

(a)

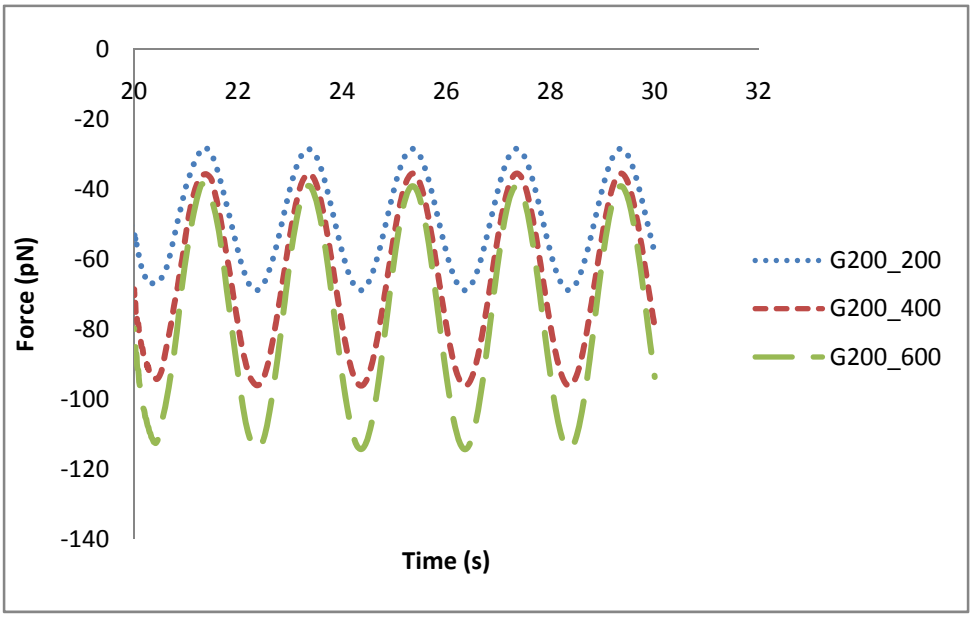

(b)

Figure 3.7 Time vs. force curve for the case of: offset 0.2 µm, frequency 0.5 Hz and indenter velocity0.1 µm/s. (a) SLS model ,(b) SnHS model.

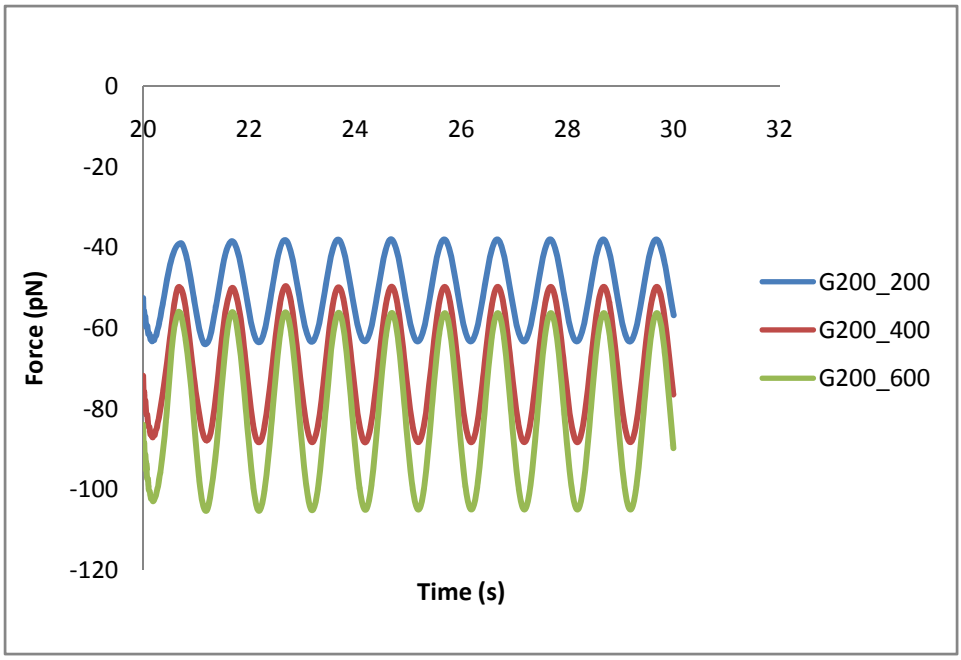

(a)

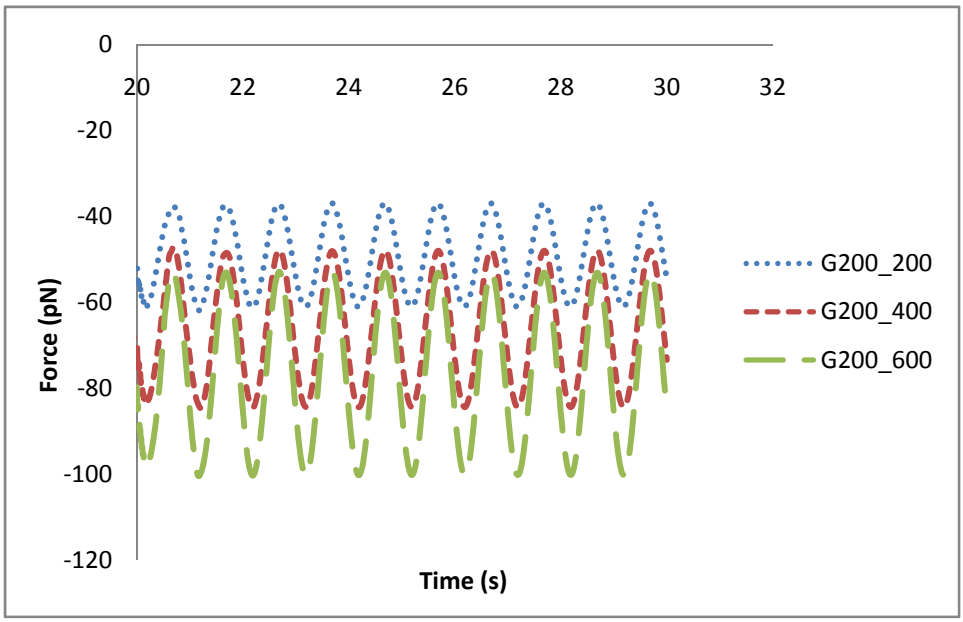

(b)

Figure 3.8 Time vs. force curve for the case of: offset 0.2 µm, frequency 1 Hz and indenter velocity0.1 µm/s. (a) SLS model, (b) SnHS model.

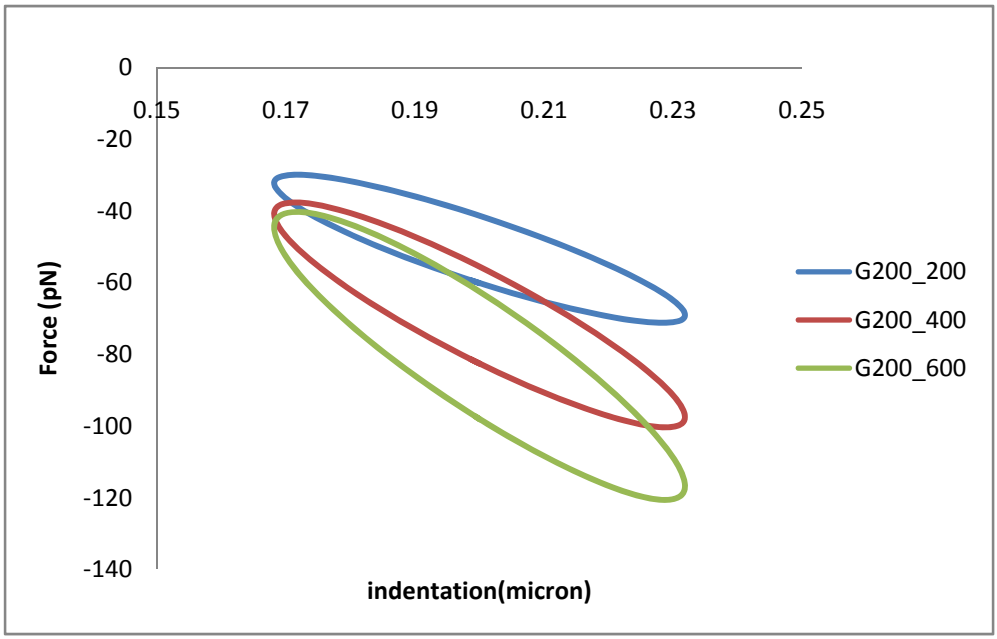

(a)

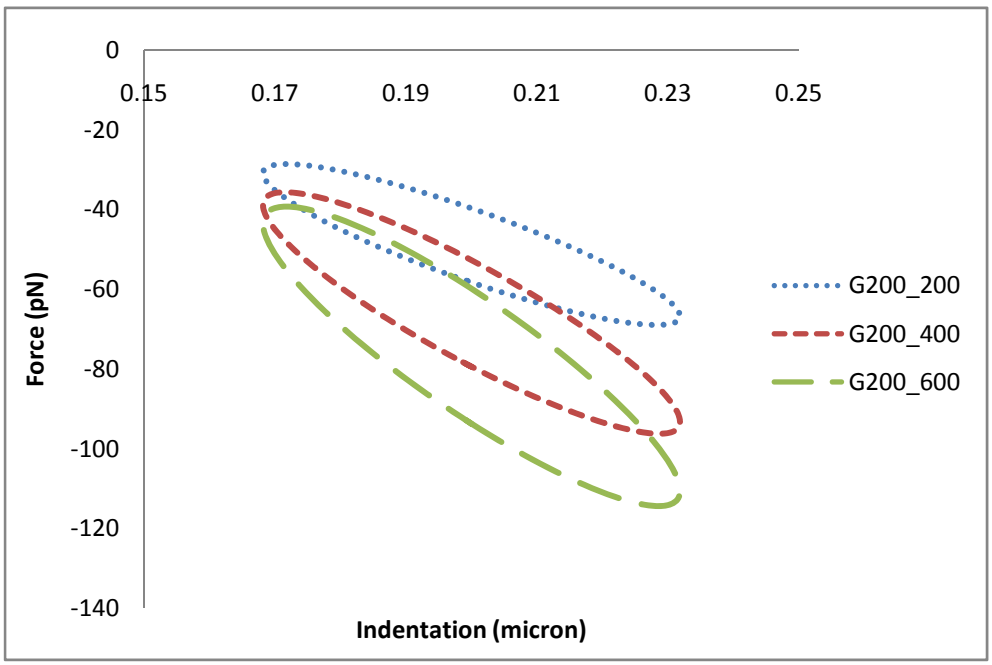

(b)

Figure 3.9 Force-indentation curves for the case of: offset 0.2 μm, frequency 0.5 Hz and indenter velocity0.1 μm/s. (a) SLS model, (b) SnHS model.

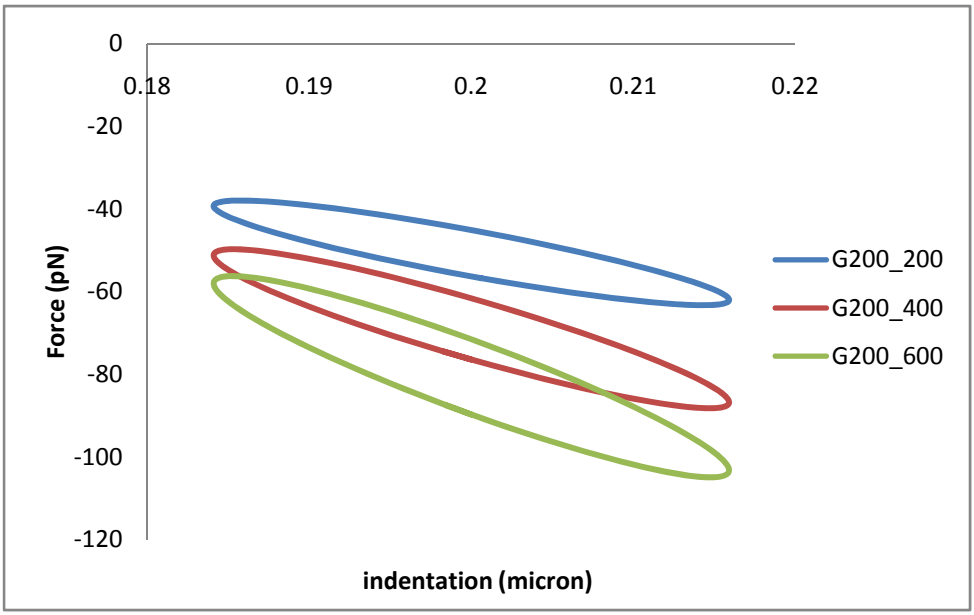

(a)

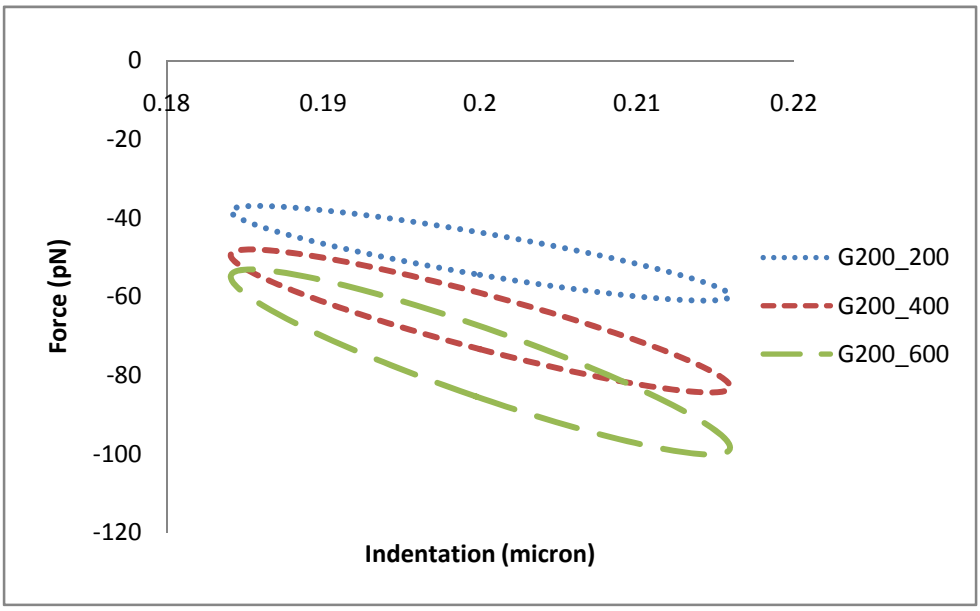

(b)

Figure 3.10 Force-indentation curves (SLS model) for the case of: offset 0.2 µm, frequency 1 Hz and indenter velocity0.1 µm/s. (a) SLS model, (b) SnHS model.

1.4. Strain-Relaxation Test

Monitoring the strain- relaxation response to a prescribed displacement is a common method of determining the viscoelastic characteristics of a material. From the analysis, for the indentation part the corresponding force deflection curve obtained is shown in Figure 3.11. For the entire time history, the force versus time curve obtained is shown in Figure 3.12. It is found that the results obtained from SLS and SnHS are very close to each other and for both cases the reaction force decrease sharply after removal of the load and then gradually switch to a steady state. The results are comparable to those obtained from experiment [13].

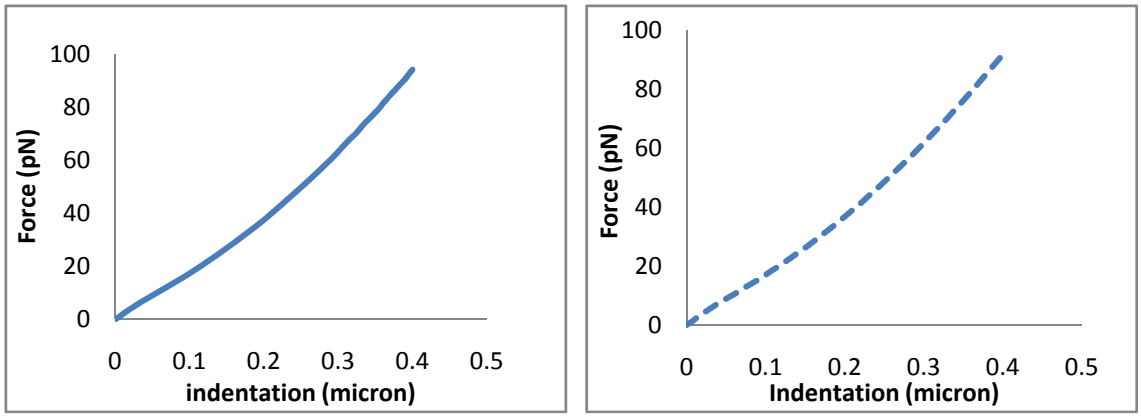

(a) (b)

Figure 3.11 Indentation force deflection curves, cortex G=275Pa, cytoplasm G=100Pa. (a) SLS model, (b) SnHS model.

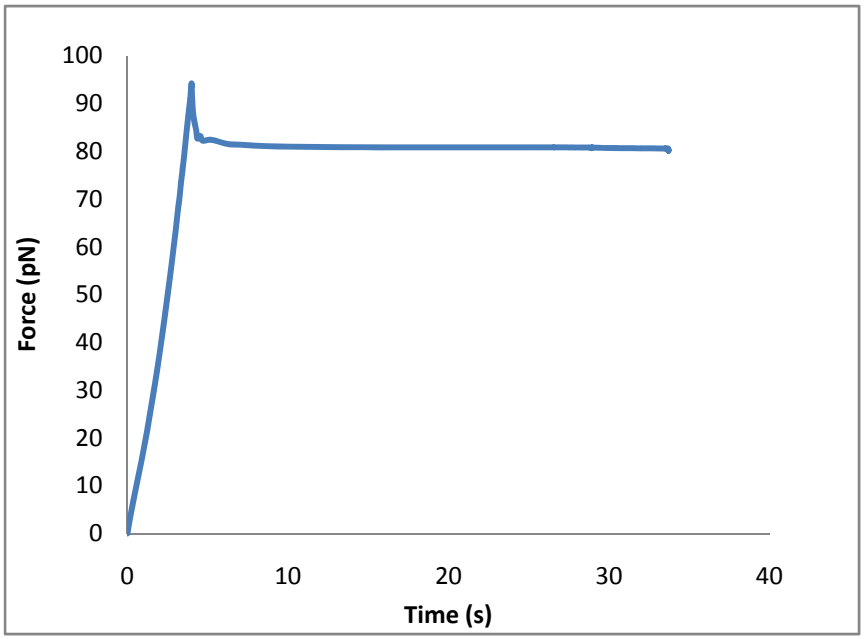

(a)

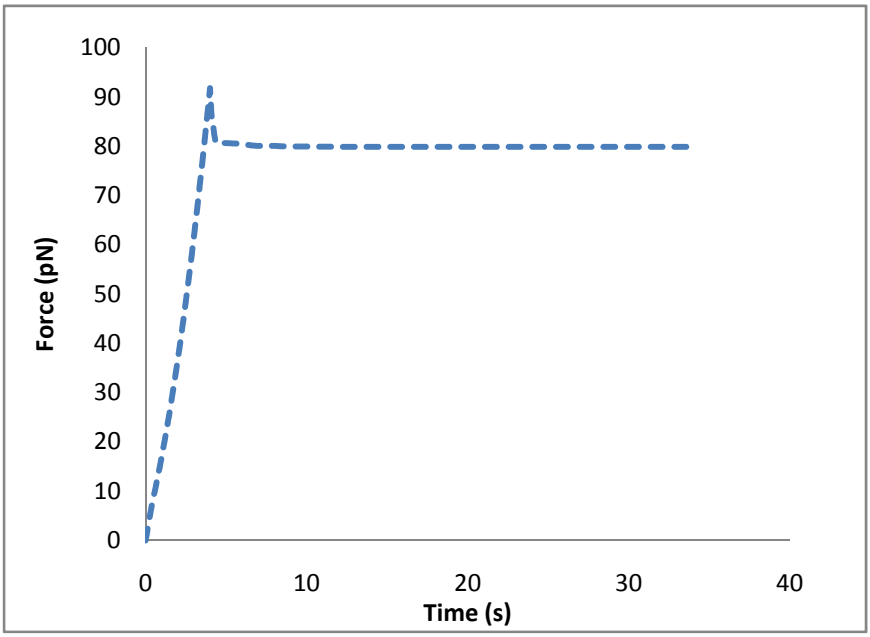

(b)

Figure 3.12 Force time curves for entire time history, cortex G=275Pa, cytoplasm G=100Pa. (a) SLS model, (b) SnHS model.

2. Results for Dynamic Shear Modulus Model

2.1. Force and Displacement Relationship

2.1.1. Effect of Concentration Factors

For fixed frequency, the equivalent Young's modulus will increase as the concentration factor increase (see Figure 3.13- Figure 3.16). And the material properties show nonlinearity for low frequency and trend to be linear as frequency increase.

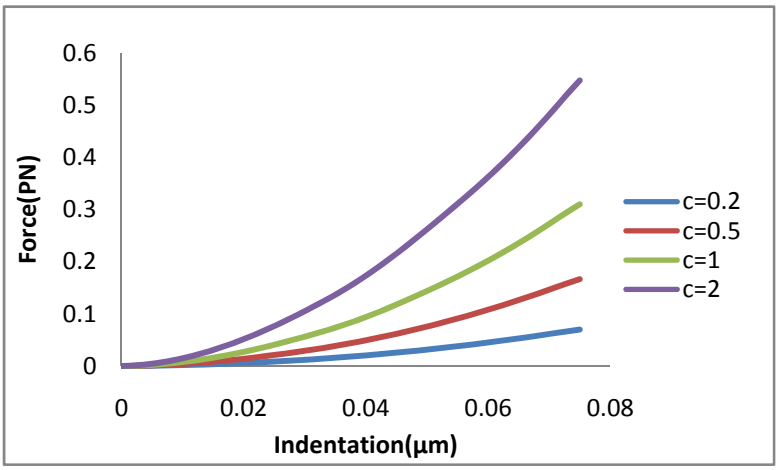

Figure 3.13 Indentation & force curves for various concentration factors under f=10Hz.

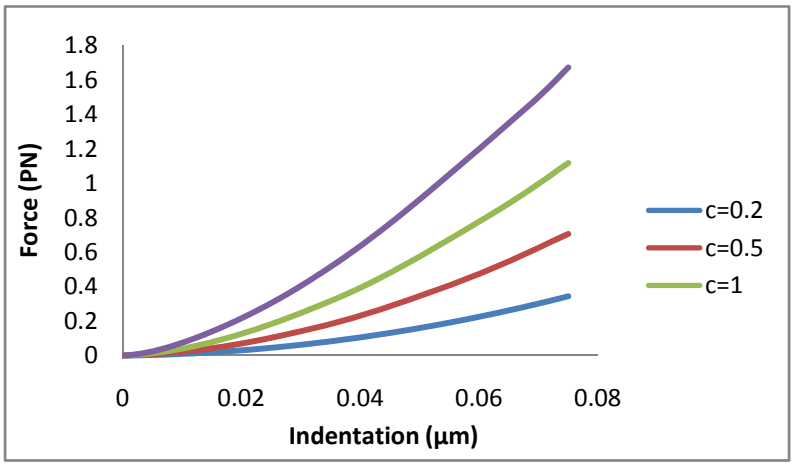

Figure 3.14 Indentation & force curves for various concentration factors under f=100Hz.

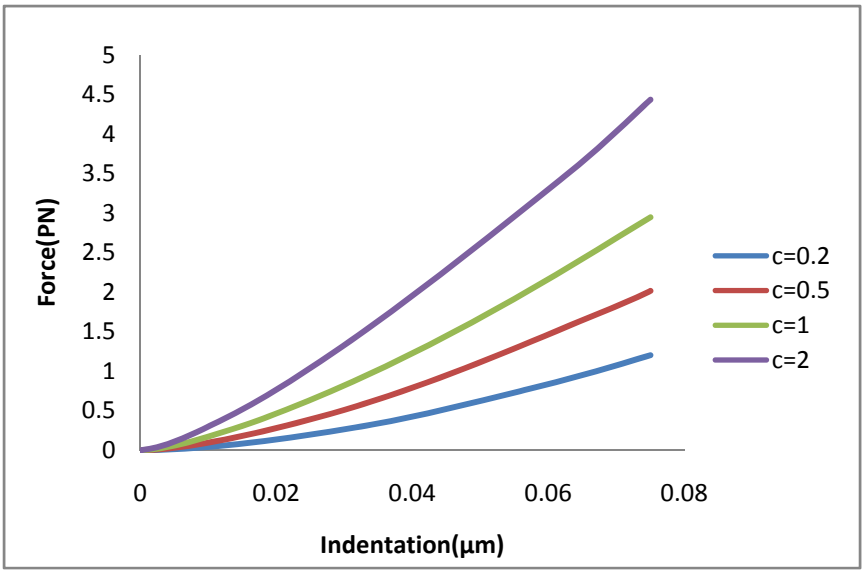

Figure 3.15 Indentation & force curves for various concentration factors under f=1000Hz.

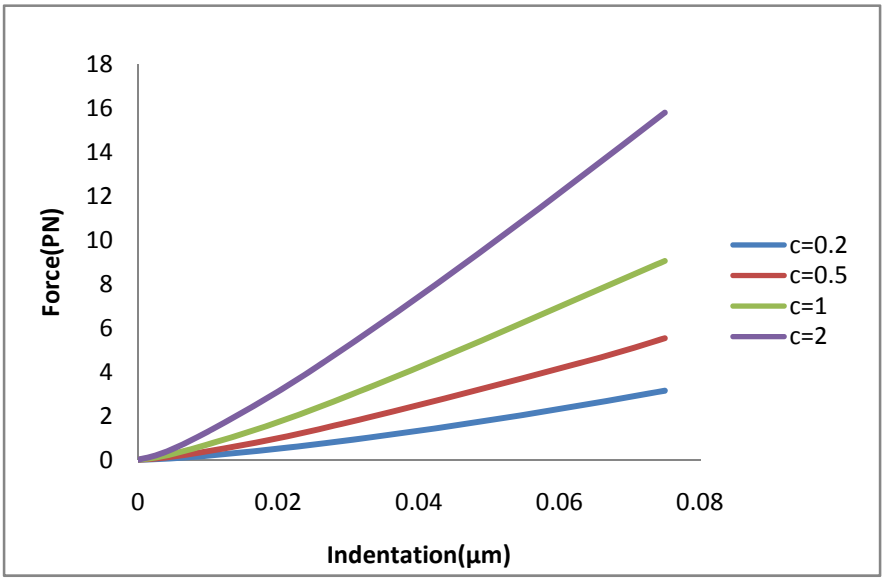

Figure 3.16 Indentation & force curves for various concentration factors under f=10000Hz.

2.1.2. Effect of Frequencies

For fixed concentration factor, the equivalent Young's modulus increase significantly as the frequency increase (see Figure 3.17- Figure 3.20)

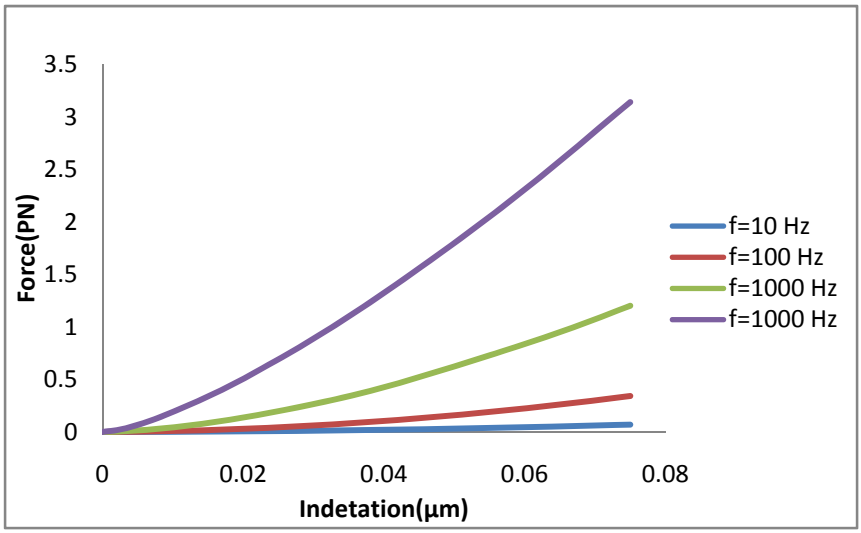

Figure 3.17 Indentation & force curves for various frequencies with the concentration factor c=0.2mg/ml.

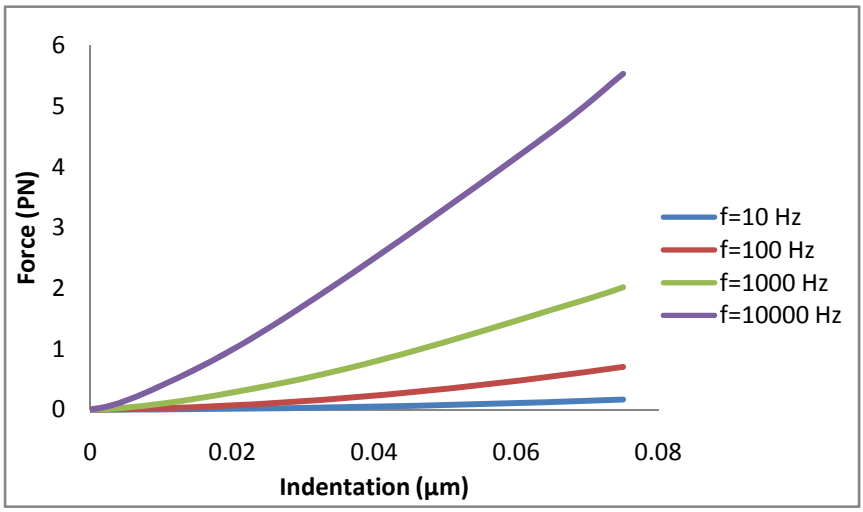

Figure 3.18 Indentation & force curves for various frequencies with the concentration factor c=0.5mg/ml.

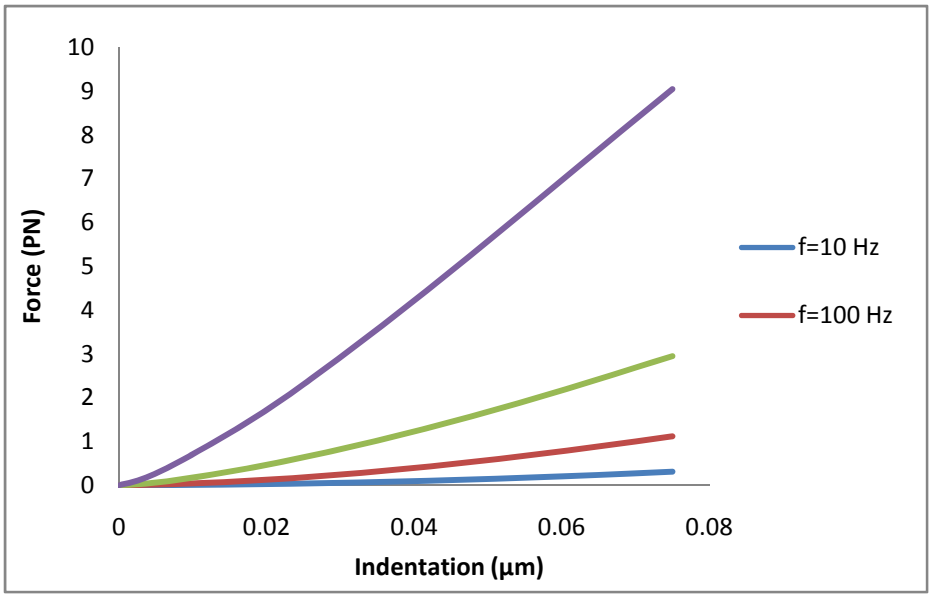

Figure 3.19 Indentation & force curves for various frequencies with the concentration factor c=1mg/ml.

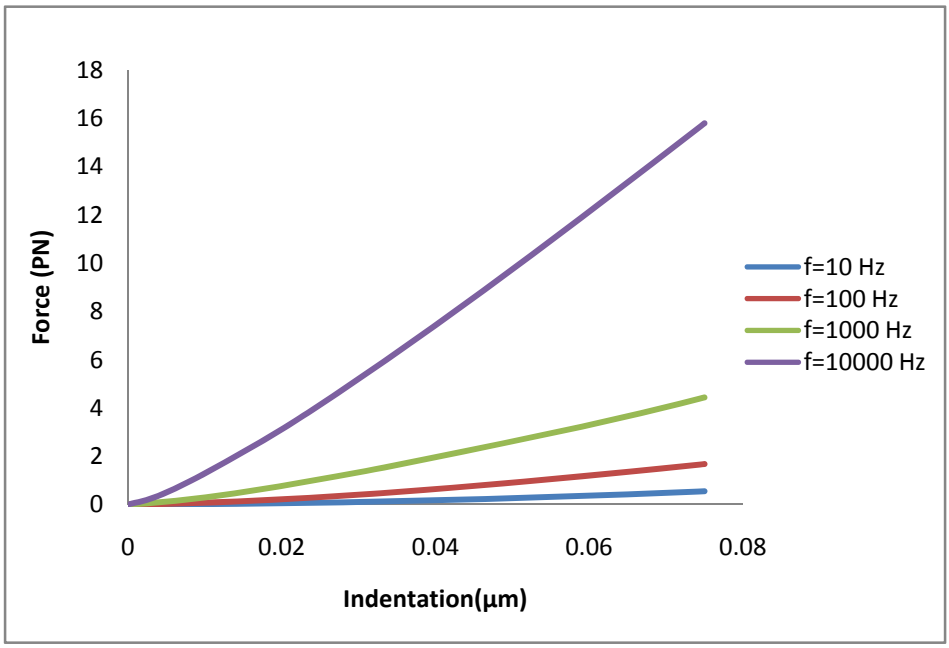

Figure 3.20 Indentation & force curves for various frequencies with the concentration factor c=2mg/ml.

2.2. Strain-Relaxation Test

For the dynamic shear modulus model, the strain- relaxation test which is used to study the time-dependent viscoelastic material properties was also simulated. From the figure, the results show the typical strain-relaxation curves (see Figure 3.21) which are comparable to the result from [13]. The equivalent Young's modulus obtained from the analysis (Figure 3.22) is also comparable to the result from [13].

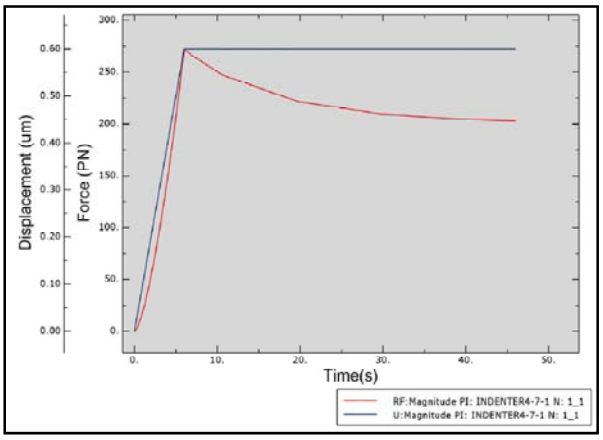

Figure 3.21 V=0.1μm/s, displacement (input) and reaction force of indenter (output) for the entire time history.

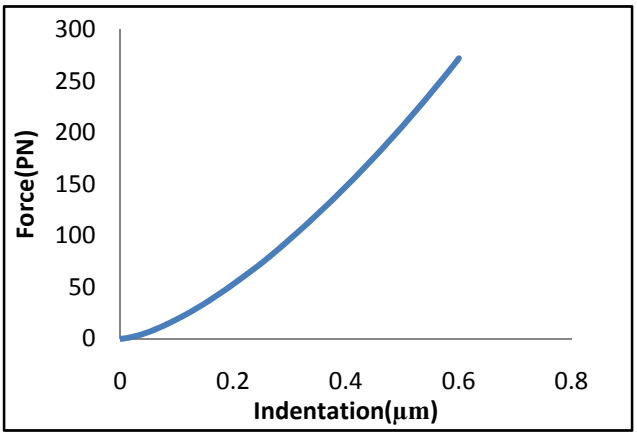

Figure 3.22 Force & indentation curve for various frequencies with the concentration factor c=2mg/ml.

E. Conclusion

In this chapter, a nonlinear finite element model of the atomic force microscopy (AFM) on the cell has been developed. The cortex was modeled as continuum based standard linear solid (SLS) viscoelastic model and its natural extension neo-Hookean solid (SnHS) viscoelastic model, as well as polymer mechanics based dynamic shear modulus model. Both of the time domain and frequency domain viscoelastic material properties of the cell were studied by applying constant force and sinusoidal force. The typical strain-relaxation experimental technique was also simulated to investigate the time-dependent material behavior of the cell. From results of finite element analysis, several relationships have been derived for interpretation of the mechanical properties of the cell.

For continuum based standard linear solid (SLS) viscoelastic model and standard neo-Hookean solid (SnHS) viscoelastic model, it is found that both the reaction force and phase lag between force and deformation will increase as cytoplasm shear modulus increases while frequency decreases. The results of strain- relaxation simulation again show the time-dependent viscoelastic material behavior of the cell which is verified against the experiment data. Also, the results of standard linear solid (SLS) viscoelastic model and standard neo-Hookean solid (SnHS) viscoelastic model are nearly the same. SnHS viscoelastic model is more general and can be used for large deformation analysis because hyperelasticity is used instead of linear elasticity used in SLS viscoelastic model. However, SnHS model is more time consuming than SLS model.

For the polymer mechanics based dynamic shear modulus model for cortex, the results show that the equivalent Young's modulus will increase as the rise of actin

concentration factor and frequency. Good results were also obtained for strain-relaxation test which can be verified by experimental results.

CHAPTER IV

FINITE ELEMENT ANALYSIS OF MAGNETIC TWISTING CYTOMETRY (MTC) FOR SINGLE LIVING CELL

A. Introduction

Magnetic twisting cytometry (MTC) is another experiment widely used to determine the mechanical properties of the cell. Though a correlation between the magnetic force acting on the bead and the lateral bead displacement or through magnetic moment and angular rotation, the material properties of the cell are obtained. Applying a pure torque to magnetic particles avoids the difficulties of constructing a well- controlled field gradient. The method consists of using a strong magnetic field pulse to magnetize a large number of ferromagnetic particles that were previously attached to an ensemble of cells. A weaker probe field oriented at 90º to the induced dipoles then causes rotation, which is measured in a lock- in mode with a magnetometer. Frequency dependence of the viscoelastic response was measured with smooth muscle cells between 0.05 and 0.4 Hz [36] and with bronchial epithelia cells up to 16 Hz [37].

In this chapter, a three-dimensional viscoelastic finite element model is developed for cell micromanipulation by bead magnetic twisting cytometry (MTC). This continuum-based viscoelastic model is employed to explore the role of material properties, constant/sinusoidal forcing rates and various frequencies on the overall mechanical response of a cell in MTC. Numerical results are validated against experiments performed on NIH 3T3 fibroblasts in [3].

B. Material Constitutive Relation

A generalized cell can be divided into three distinct layers: an outer cortical layer which is formed by the actin filament networks (cortex), an inner cytoplasmic region, and the nucleus. In magnetic twisting cytometry (MTC), a separated region of cell including cortex and cytoplasm without nucleus is modeled as a cell block will be studied.

1. Modeling of Actin Cortex

The actin filaments are known to behave as biopolymers and form a complex filament network whose properties are dependent on the individual filament characteristics. The actin cortex region is modeled as Standard Linear Solid (SLS) and its natural extension Standard neo-Hookean Solid (SnHS) material.

The normalized shear stress relaxation modulus is often represented by a series expansion in Prony Series:

$$g_R(t) = 1 - \sum_{i=1}^{N} g_i[1 - \exp(-t/\tau_i)] \tag{4.1}$$

For the ***standard linear solid*** model, the shear relaxation modulus $G(t)$ can be expressed as a Prony series expansion with the first term:

$$G(t) = G_0[1 - g_1(1 - e^{-t/\lambda_1})] \tag{4.2}$$

The relationship between the two sets of viscoelastic parameters can be derived as

$$G_0 = k_1 + k_2, g_1 = \frac{k_2}{k_1 + k_2}, \lambda_1 = \frac{\mu}{k_2} \tag{4.3}$$

According to [3], the material properties for SLS and SnHS in this study are given by the follows:

$$G_0 = 100Pa, g_1 = 0.9, \lambda_1 = 0.1\text{s}$$

2. Modeling of Inner Cytoplasm

Cytoplasm is composed of an organized network of cytoskeleton filaments of actin, inter mediate filaments, and microtubules. Also according to [3], here it is assumed that the material model of cytoplasm region is SLS and SnHS Model with:

$$G_0 = 100Pa, 200Pa, 400Pa, \quad g_1 = 0.9, \quad \lambda_1 = 1\text{s}$$

C. FEM Analysis

1. Model Geometry

The cell geometry is modeled as a 3D cylindrical block [3] with 10-μm-high and 40- μm-wide diameter, see Figure 4.1. The bead is rigid ferrous sphere of diameter 4.5 μm, which makes an indentation angel of 90 deg at the center of the cell block. The cortical thickness is assumed to be 0.2 μm with the inner region being the cytoplasm.

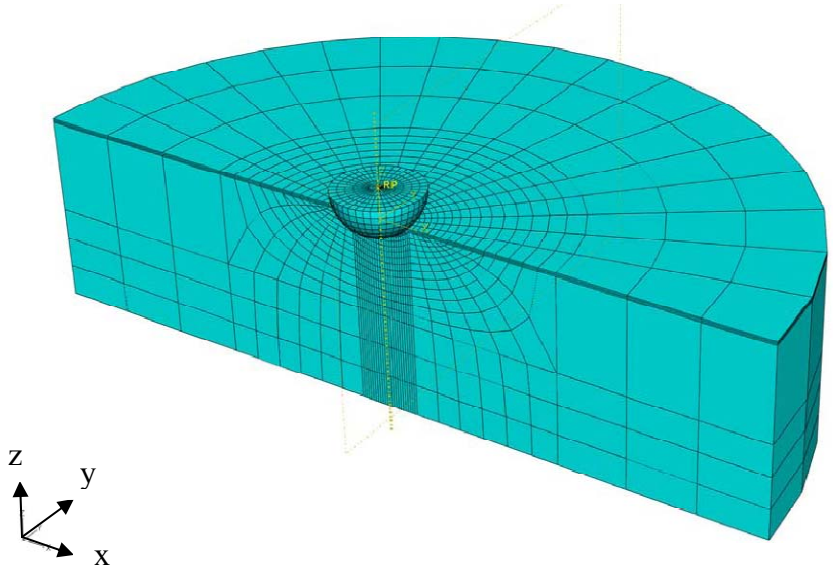

Figure 4.1 3-D finite element mesh of the cylindrical cell block selected for MTC simulation. The top of the actin cortical region having a thickness of 0.2 μm, and the part below forms the inner cytoplasm without nucleus.

All simulations were performed using a commercially available finite element modeling software ABAQUS. To accurately capture details of deformation and the associated stress and strain patterns, a finer mesh is employed towards the bead region and the finite element model consists of 7125 nodes with 6210 C3D8R elements.

2. Boundary Conditions

Since a symmetric boundary condition is assumed, only half of the material body is modeled. The base of the block was constrained in all directions to create a cell fully adhered to the substrate, and symmetric boundary conditions along y axis were applied (U2=UR1=UR3=0) to the half of the section.

3. Applied Load

Two kinds of loads, constant as well as sinusoidal force have been applied to the bead:

a. For the constant force, three constant rates of force 100pN/s, 250pN/s and 500pN/s have been applied.
b. For the sinusoidal force, three different amplitudes 125pN, 250pN and375pN have been used. During forcing, the bead is tethered to the cell over a part of its circumference.

D. Results and Discussion

1. Stress Distribution

The stress field induced in the cell block with SLS model with both of the cortex and cytoplasm same shear modulus G=100 Pa under the load rate 250pN/s for 1s is shown in Figure 4.2. The von- Mises stress field in the cell block is concentrated in the immediate vicinity of the bead, which is because the squeezing exerted by the bead spreads stress whereas the pulling only affects a very small region. The stress field is more diffuse in front of the bead compared to the rear. Both extremes are located on actin cortex. The high-stress field does not penetrate significantly into the cell cytoplasm.

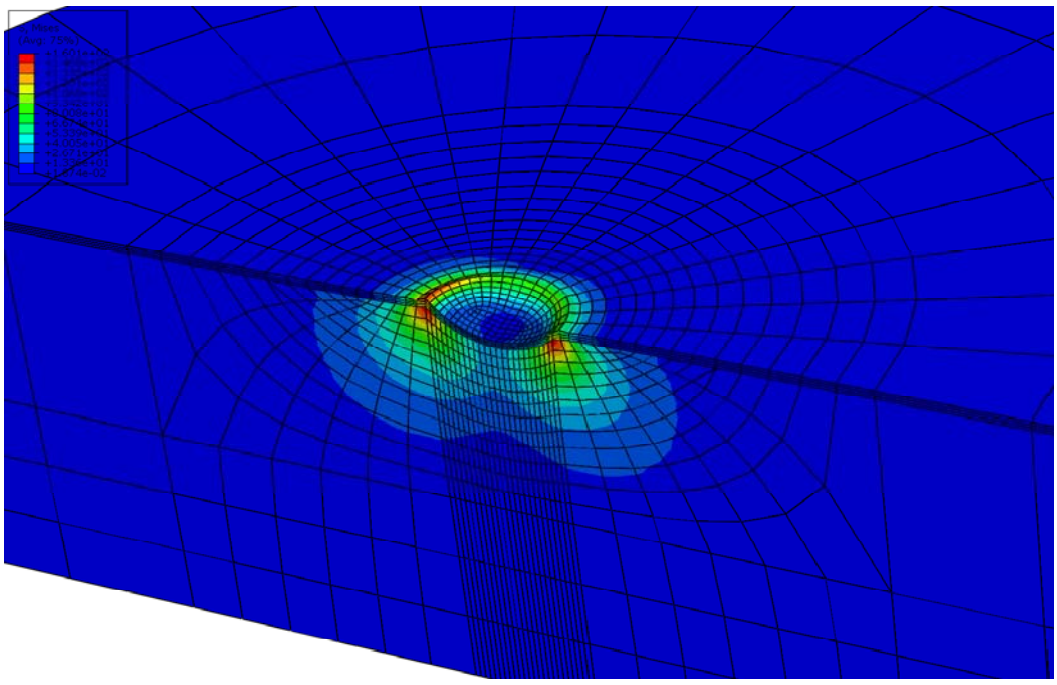

Figure 4.2 Distribution (3-D contours) of the amplitude of effective (von-Mises) stress for SLS model G=100 for both cortex and cytoplasm due to a lateral force 250pN.

2. Strain Distribution

The shear strain distribution is also concentrated near the surface and decreases away from bead surface (Figure 4.3 and Figure 4.4).

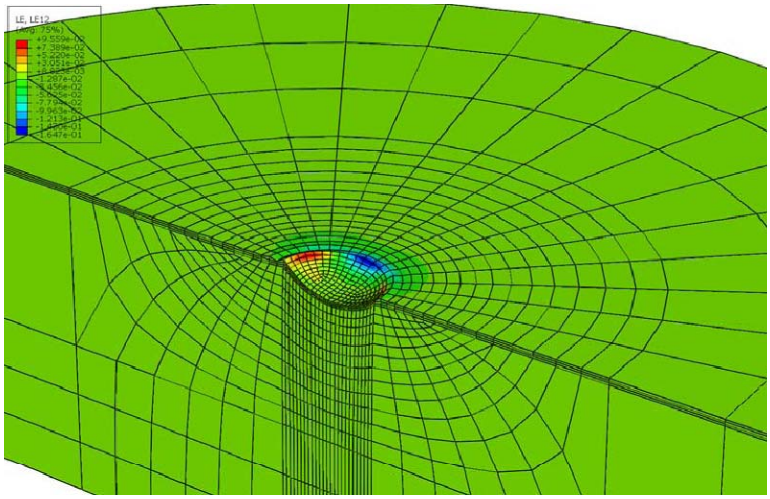

Figure 4.3 Strain distribution (3-D contours) induced by bead displacement along 1-2 direction for SLS model G=100 Pa for both cortex and cytoplasm due to a lateral force 250pN.

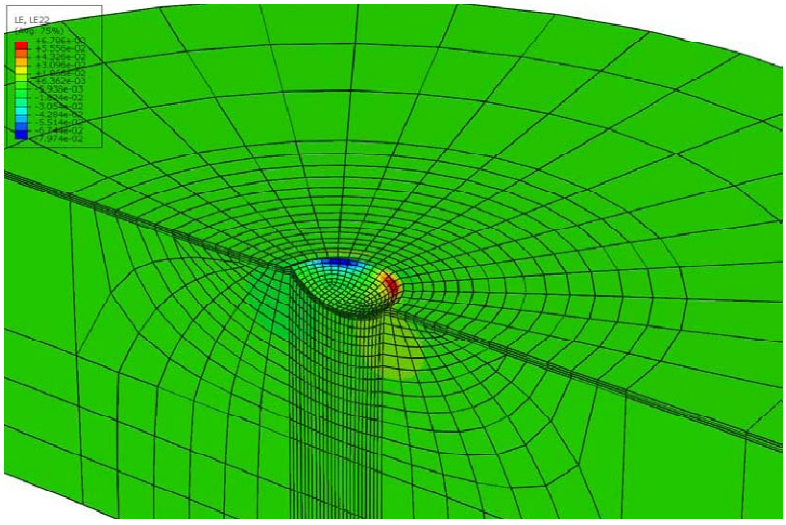

Figure 4.4 Strain distribution (3-D contours) induced by bead displacement along 2-2 direction for SLS model G=100 Pa for both cortex and cytoplasm due to a lateral force 250pN.

3. Displacement Distribution

Magnetic forcing produces both translation in the x-direction, z-direction and rolling about the y-axis (Figure 4.5, Figure 4.6). For U1 (displacement along x-direction), the maximum deformation locates along the upper edge while that of U3 (vertical displacement) locates on the two sides of the indent vicinity. U1 displacement field has spread a relative larger area than U3 (vertical displacement), and both of them fade away from the center of indent.

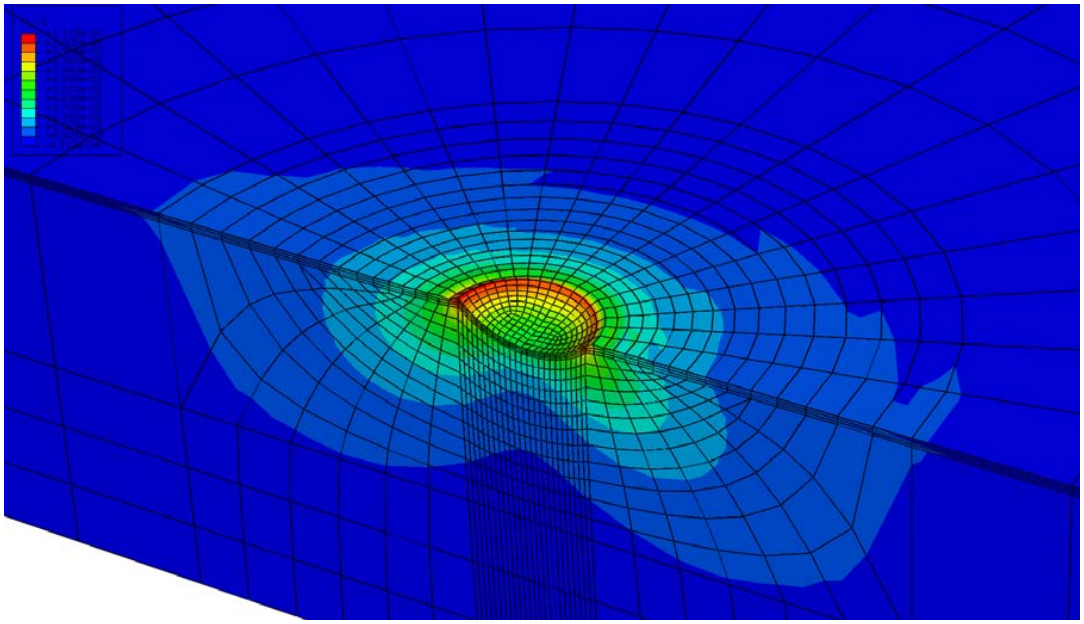

Figure 4.5 The lateral displacement distribution (3-D contours) for SLS model G=100 Pa due to a lateral force 250pN.

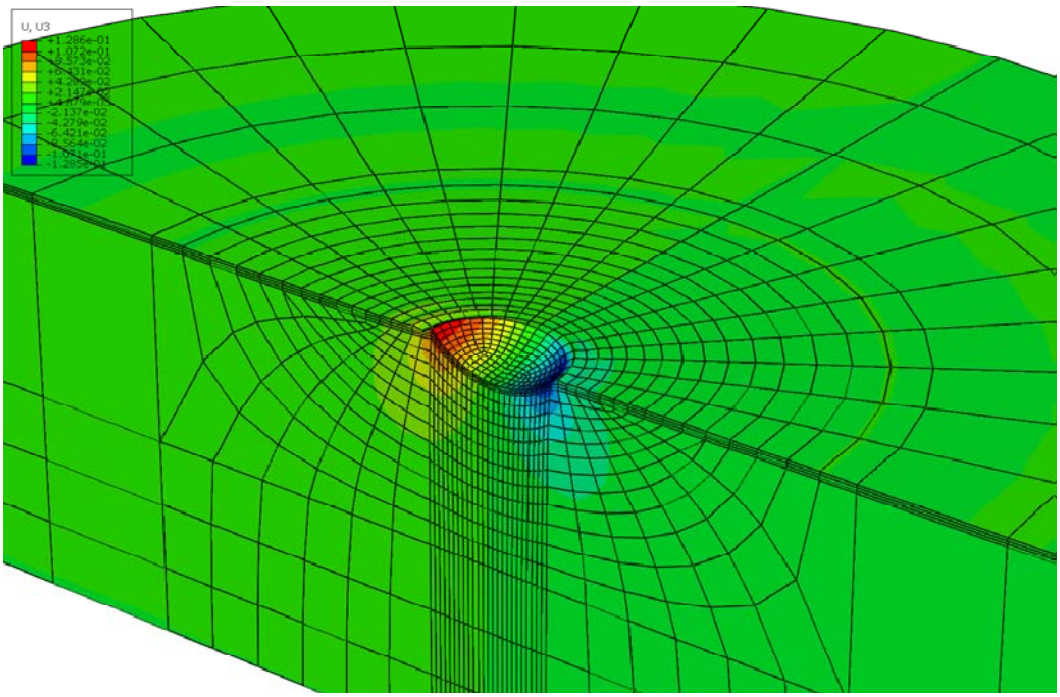

Figure 4.6 The vertical displacement distribution (3-D contours) for SLS model G=100 Pa due to a lateral force 250pN.

4. Bead Behavior

4.1. Constant Forcing Rates

4.1.1. Contribution of Cytoskeletal Shear Modulus

The forcing timescale is comparable to the cytoskeleton relaxation time scale and more importantly than the cortex since it exceeds relaxation time scale of cortex. Therefore, the force-displacement curve is dominated by the characteristics of the cytoskeleton [3]. Here, the cases for different cytoplasm shear modulus, G=100Pa, 200Pa, 400Pa, 600Pa were carried out. It is found that the bead displacements decrease while the shear moduli increase (Figure 4.7-Figure 4.9). Again, the response curve was observed to be more nonlinear for higher forcing rate.

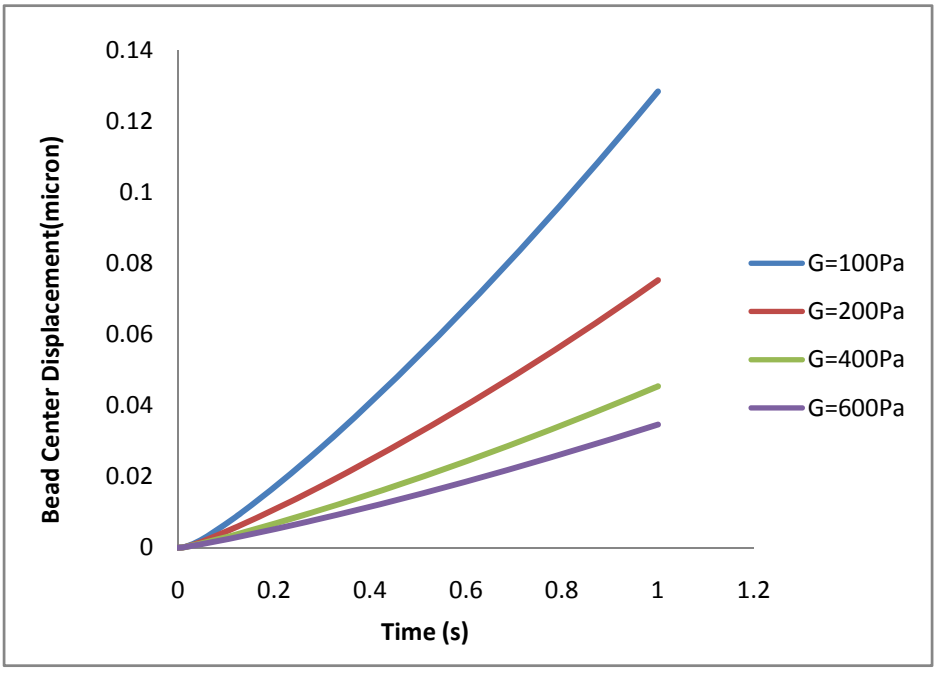

Figure 4.7 Bead center lateral displacement versus time, resulting from the SLS model with fixed forcing rate 100pN/s.

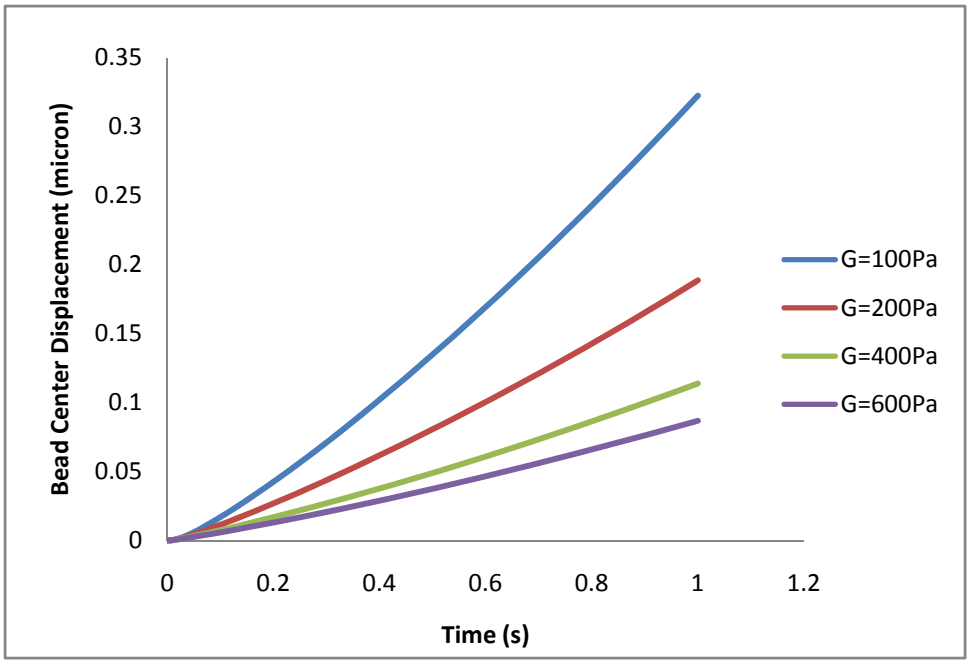

(a)

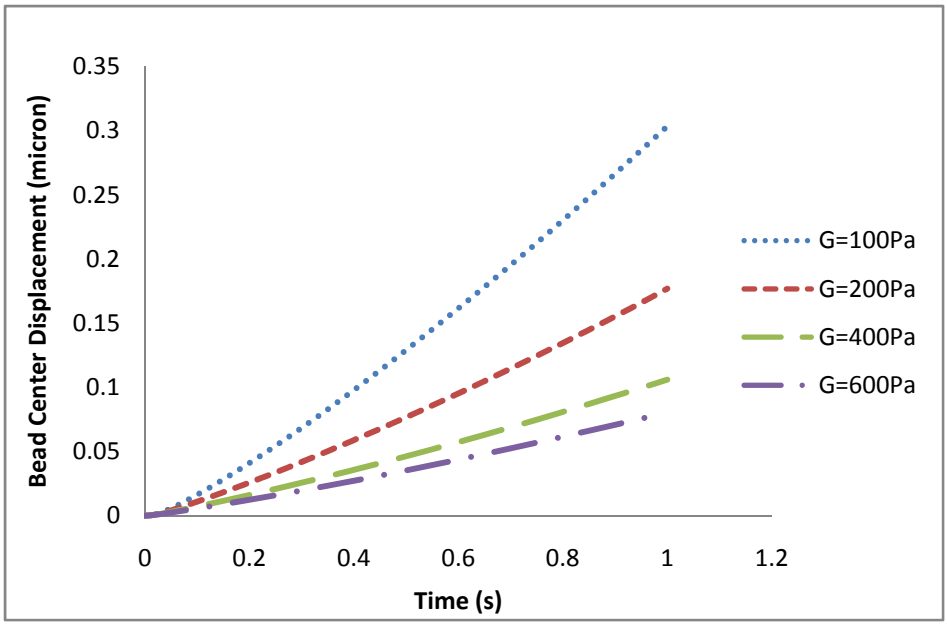

(b)

Figure 4.8 Bead center lateral displacement versus time, resulting from (a) SLS model and (b) SnHS model, for fixed forcing rate 250pN/s.

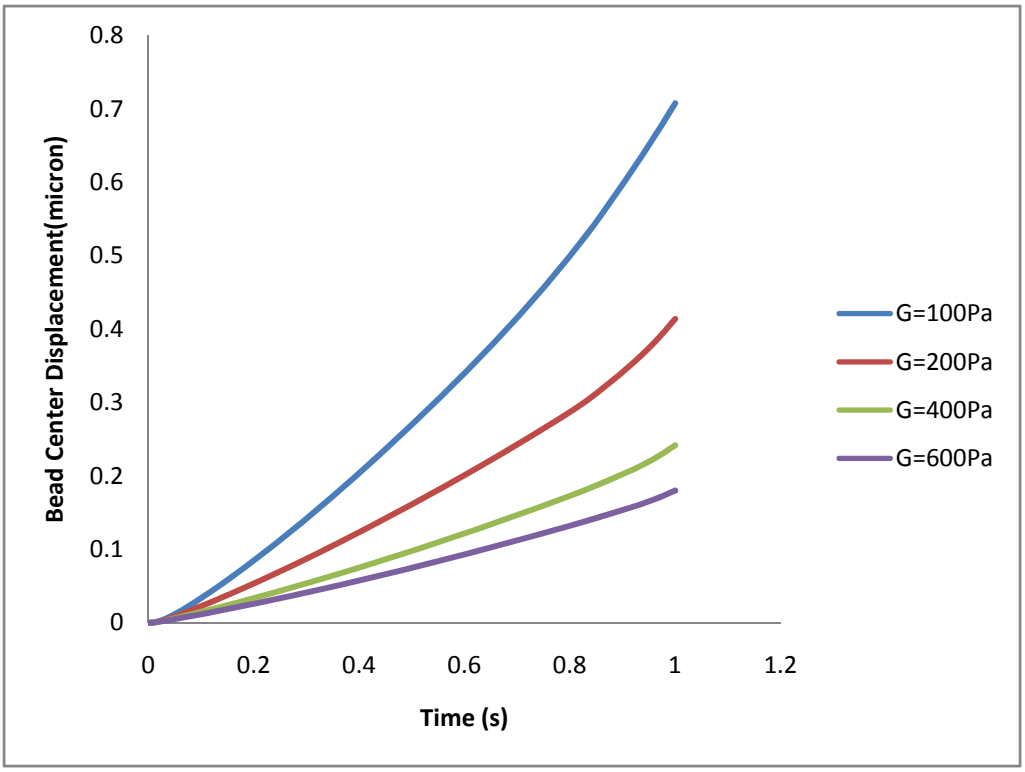

Figure 4.9 Bead center lateral displacement versus time, resulting from the SLS model fixed forcing rate 500pN/s.

4.1.2. Influence of the Forcing Rates

To further assess the implications of the viscoelastic behavior, simulations with different rates of force application on the bead center were performed. From the results it can be seen that faster forcing rates led to smaller bead displacements, consistent with the increasing resistance of the cell block with the rate of forcing (Figure 4.10-Figure 4.13). On the other hand, the response curve was observed to be more nonlinear for higher forcing rate.

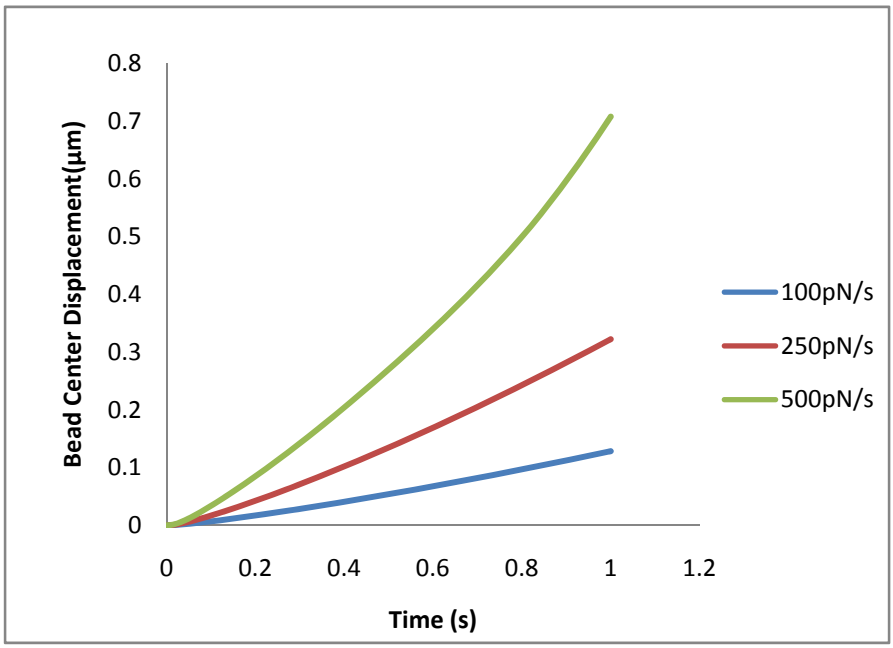

Figure 4.10 Bead center lateral displacement versus time, resulting from the SLS model with cortex shear modulus 100 Pa and cytoplasm shear modulus 100 Pa due to different force rates.

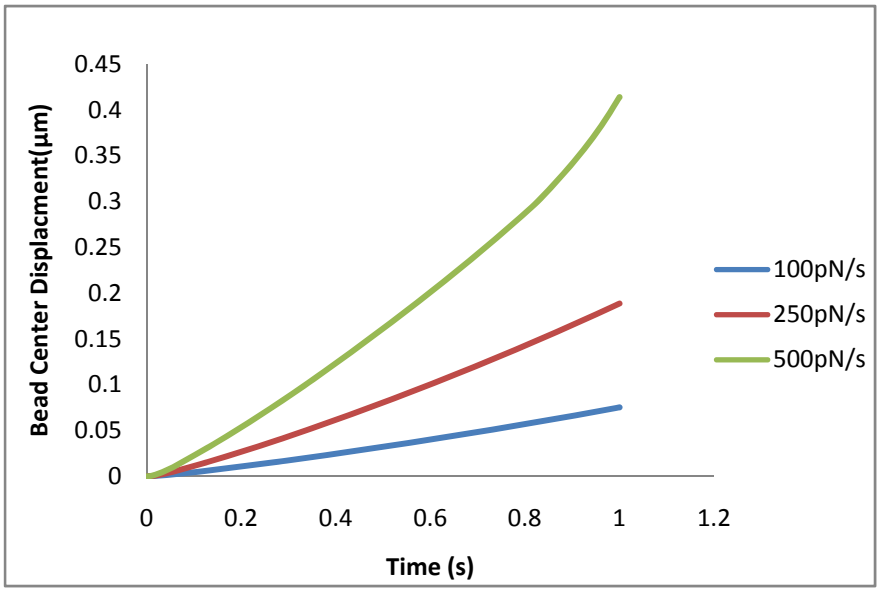

Figure 4.11 Bead center lateral displacement versus time, resulting from the SLS model with cortex shear modulus 100 Pa and cytoplasm shear modulus 200 Pa due to different force rates.

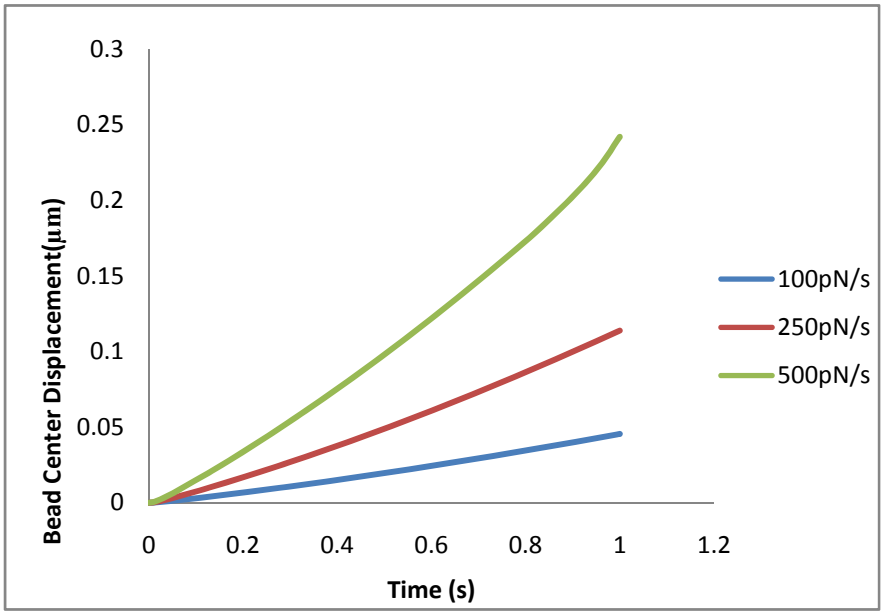

Figure 4.12 Bead center lateral displacement versus time, resulting from the SLS model with cortex shear modulus 100 Pa and cytoplasm shear modulus 400 Pa due to different force rates.

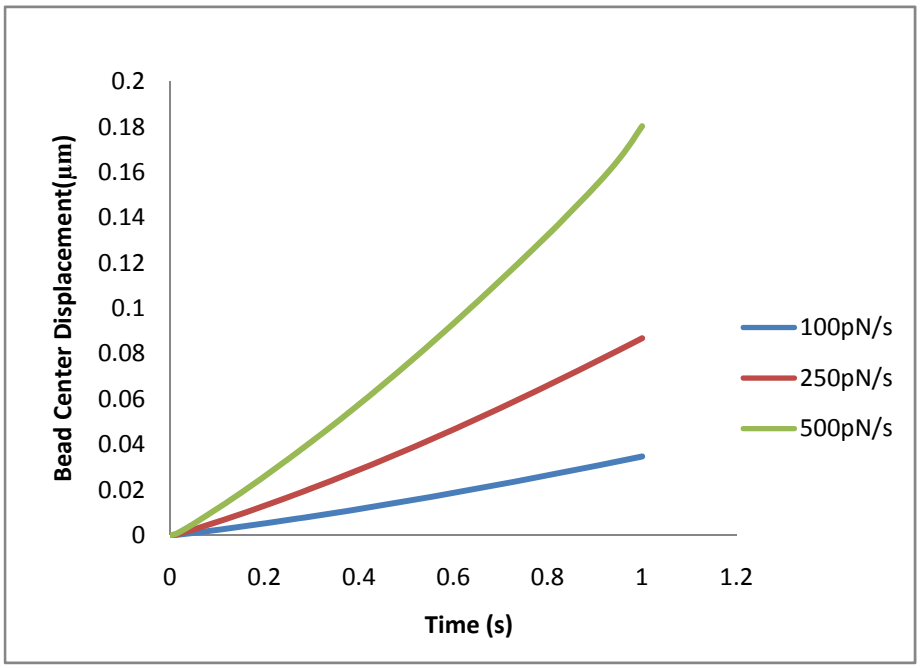

Figure 4.13 Bead center lateral displacement versus time, resulting from the SLS model with cortex shear modulus 100 Pa and cytoplasm shear modulus 600 Pa due to different force rates.

4.2. Application of Sinusoidal Force

4.2.1. Influence of Frequencies

To study the frequency dependence of the dynamic viscoelastic behavior of the cell, sinusoidal forces with different frequencies have been applied to the bead center. The results show that bead displacement under sinusoidal forcing exhibits an oscillatory behavior and the displacement scales approximately with the inverse of the frequencies, see Figure 4.14-Figure 4.16. For example, for f=0.1Hz, the displacement of the bead center is about 0.2 µm which for f=10 Hz it is only about 0.05 µm.

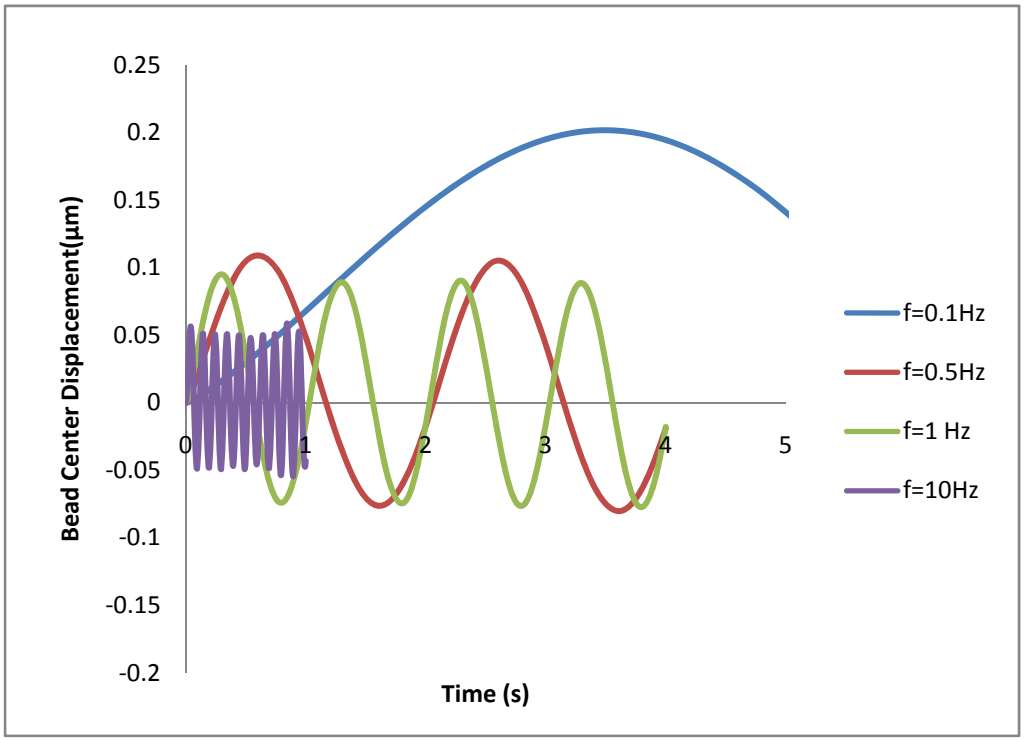

Figure 4.14 Bead center lateral displacement versus time, resulting from the SLS model with both cortex cytoplasm shear modulus 100 Pa under sinusoidal forcing amplitude 125pN with different frequencies.

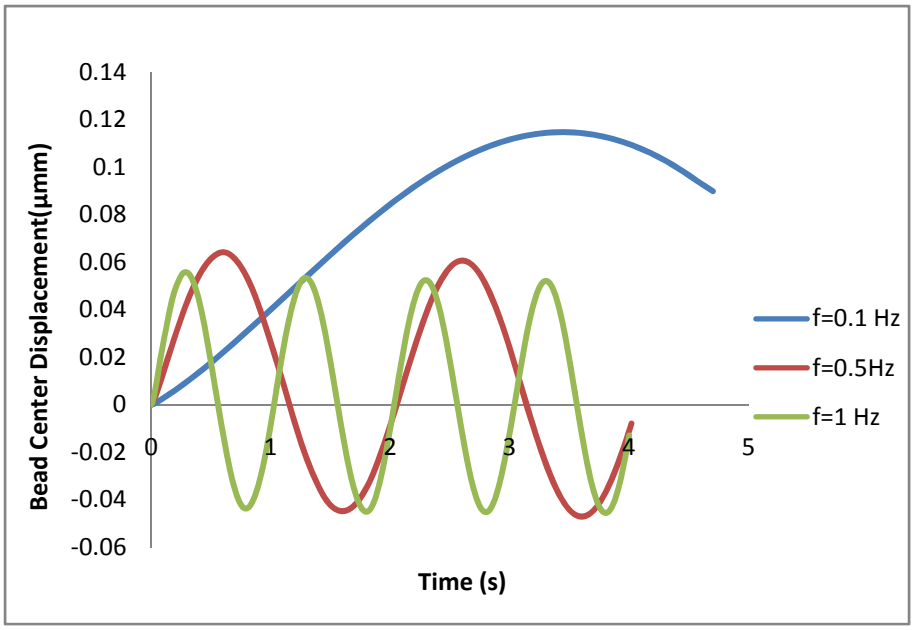

Figure 4.15 Bead center lateral displacement versus time, resulting from the SLS model with cortex G=100 Pa and cytoplasm G= 200 Pa under sinusoidal forcing amplitude 125pN with different frequencies.

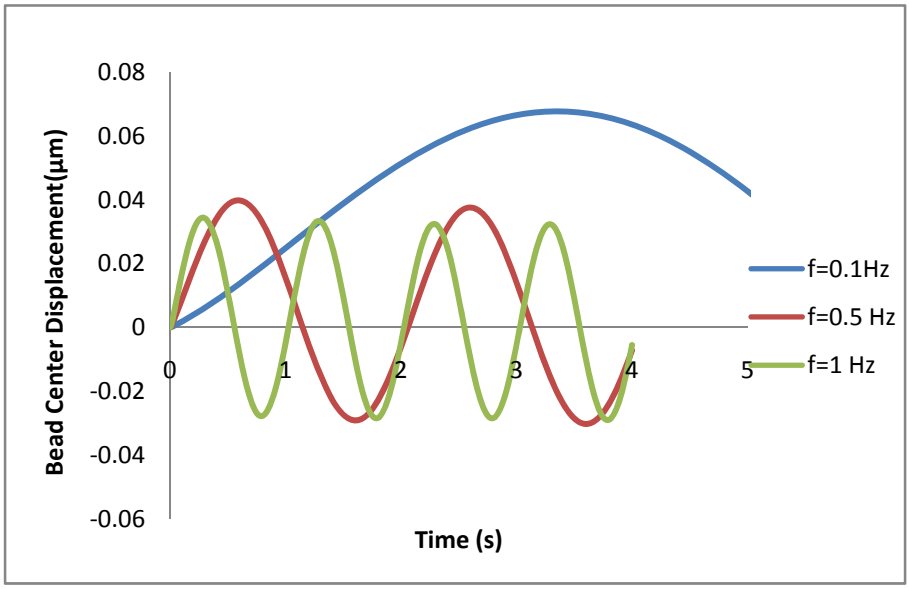

Figure 4.16 Bead center lateral displacement versus time, resulting from the SLS model with cortex G=100 Pa and cytoplasm G= 400 Pa under sinusoidal forcing amplitude 125pN with different frequencies.

Figure 4.17 - Figure 4.19 shows the calculated Force-displacement response at various frequencies of applied excitation for material having shear modulus 100Pa, 200pa and 400Pa respectively. The amplitude of the response decreases with increasing frequency of applied excitation leading to a more localized deformation. And the results are good fit with those in [16] and [3].

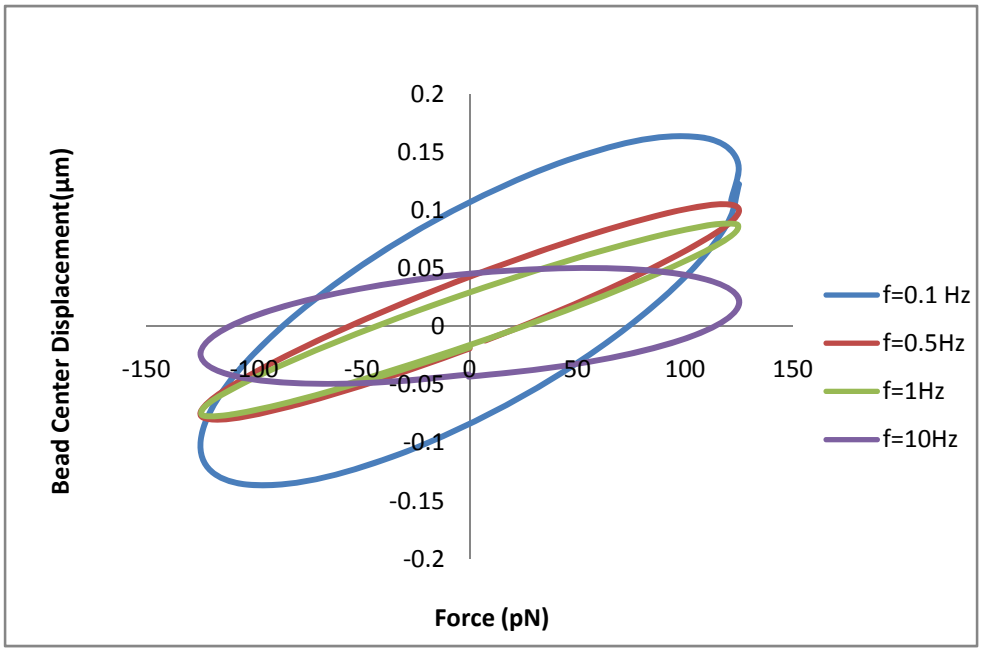

Figure 4.17 Force versus bead center lateral displacement, resulting from the SLS model with cortex G=100 Pa and cytoplasm G= 100 Pa under sinusoidal forcing amplitude 125pN with different frequencies.

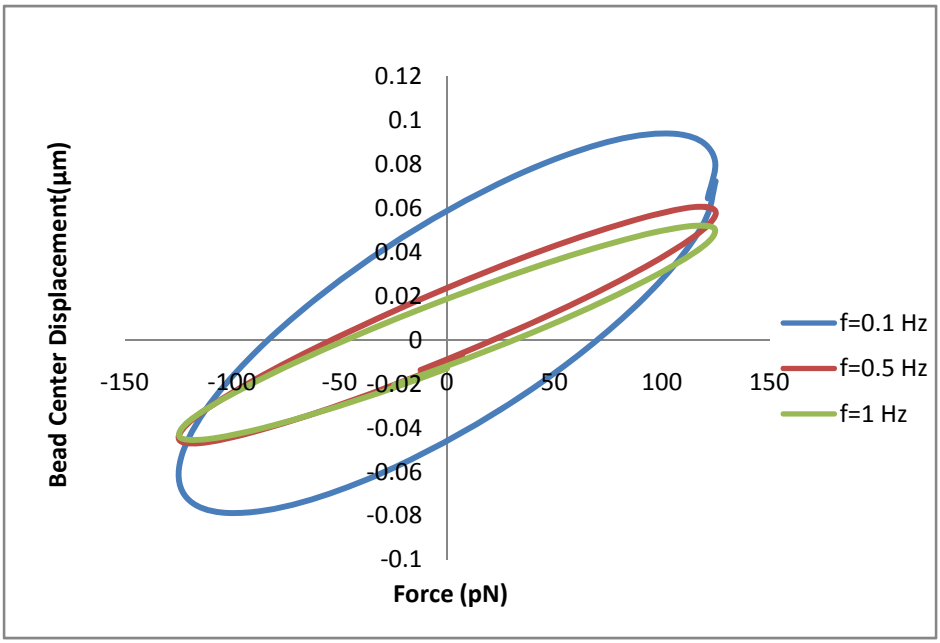

Figure 4.18 Force versus bead center lateral displacement, resulting from the SLS model with cortex G=100 Pa and cytoplasm G= 200 Pa under sinusoidal forcing amplitude 125pN with different frequencies.

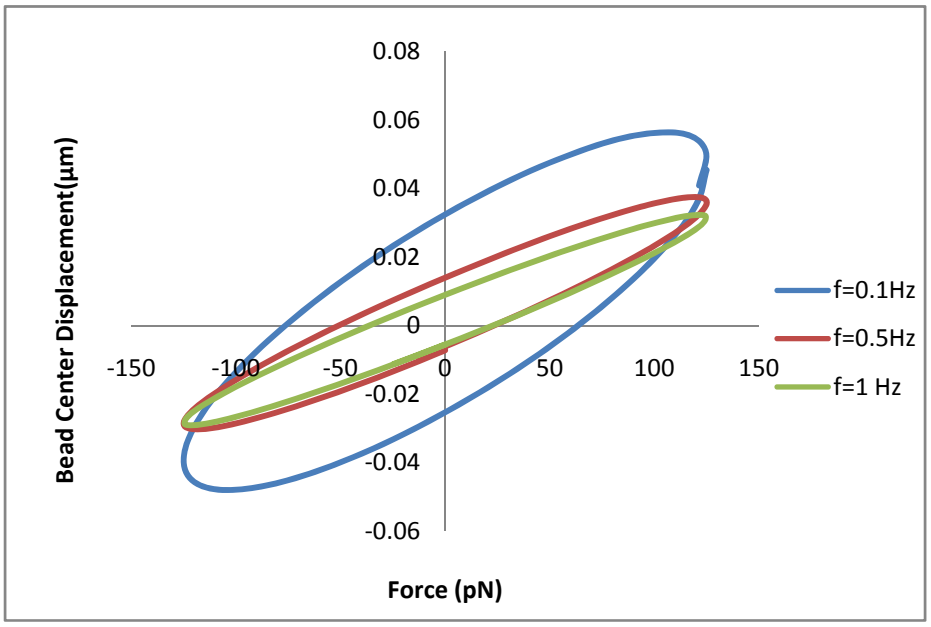

Figure 4.19 Force versus bead center lateral displacement, resulting from the SLS model with cortex G=100 Pa and cytoplasm G= 400 Pa under sinusoidal forcing amplitude 125pN with different frequencies.

4.2.2. Influence of Shear Modulus

For the sinusoidal forces, the contribution the cytoskeleton shear modulus to the mechanical property of cell was also investigated. Simulations with cell block having different cytoskeleton shear modulus G=100Pa, 200Pa and 400Pa. And from the results, it is found that the bead center displacement dropped correspondingly as the shear modulus increases, see time versus bead center displacement curves for fixed frequencies and force amplitude in Figure 4.20, Figure 4.21 and Figure 4.22. From sinusoidal force versus bead center displacement curves, see Figure 4.23-Figure 4.25, it can be observed that as the shear modulus increase the bead center displacement decreases and the phase lag between force and displacement becomes smaller. To compare the SnHS model with SLS model, a group of test for the case f=0.1 Hz, force rate=125pN/s was carried out. It is found that for the same load, the bead center displacement for and SLS model are same and they also share the same paten in both displacement-time curve and force-displacement curves(Figure 4.20(a), (b) and Figure 4.23 (a), (b)).

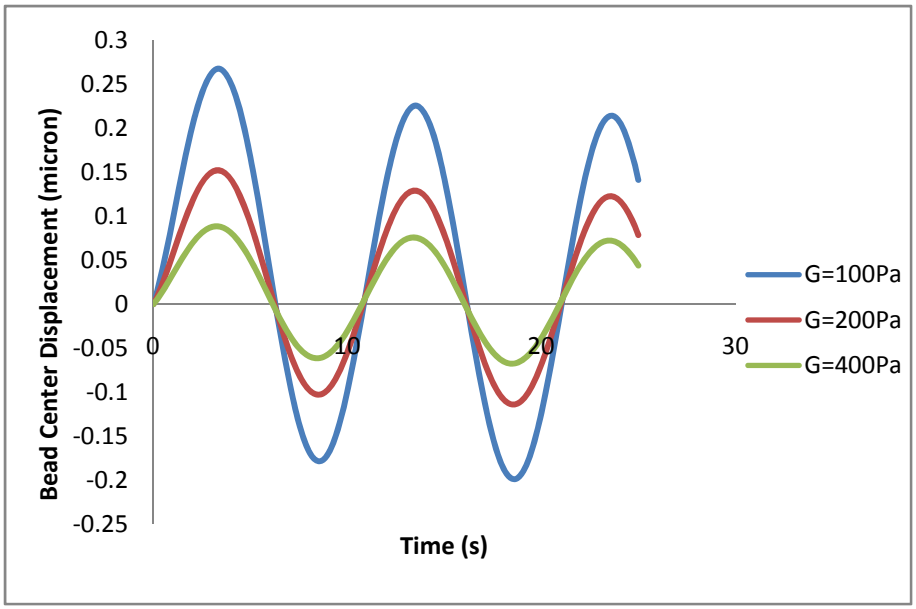

(a)

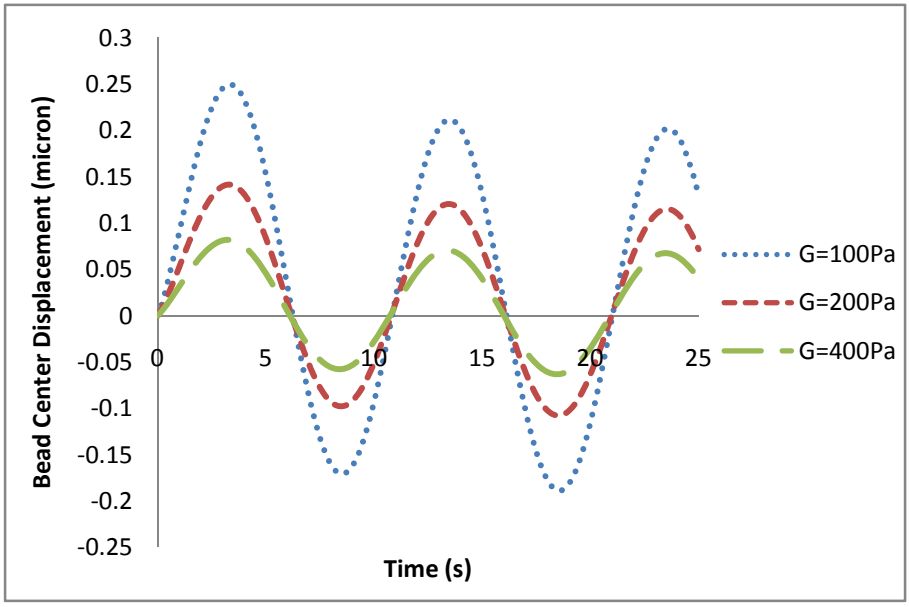

(b)

Figure 4.20 Bead center lateral displacement versus time, resulting from the (a) SLS model and (b) SnHS model for fixed sinusoidal force amplitude 125pN with f=0.1Hz for various shear modulus.

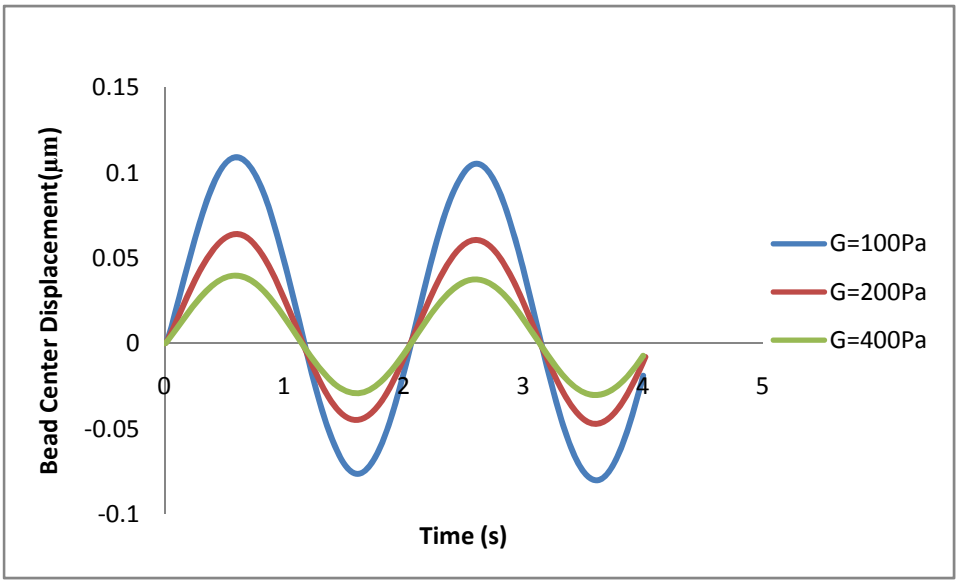

Figure 4.21 Bead center lateral displacement versus time, resulting from the SLS model for fixed sinusoidal force amplitude 125pN with f=0.5Hz for various SLS model shear modulus.

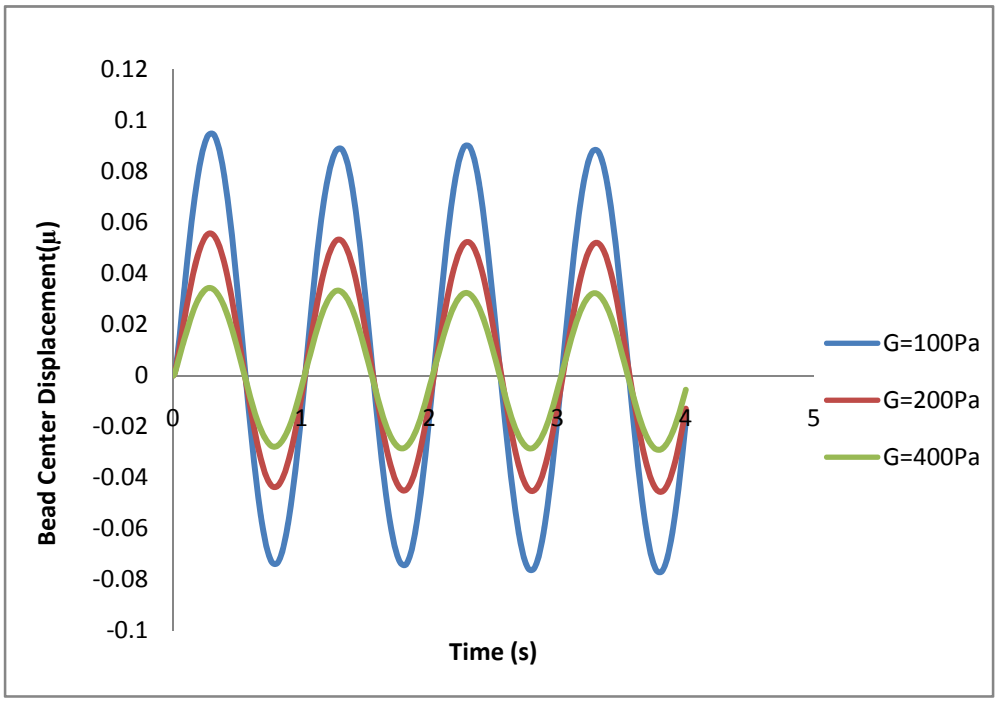

Figure 4.22 Bead center lateral displacement versus time, resulting from the SLS model for fixed sinusoidal force amplitude 125pN with f=1Hz for various SLS model shear modulus.

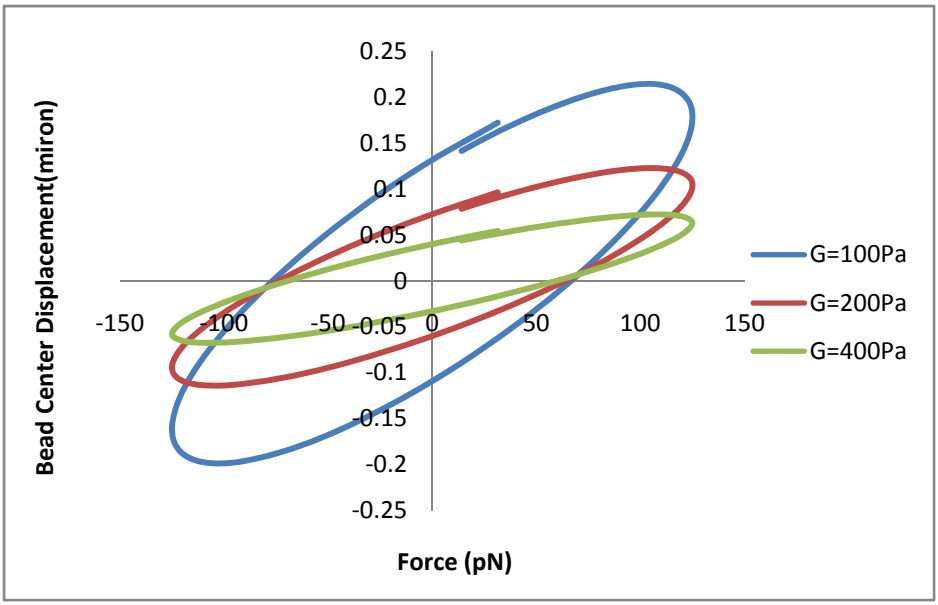

(a)

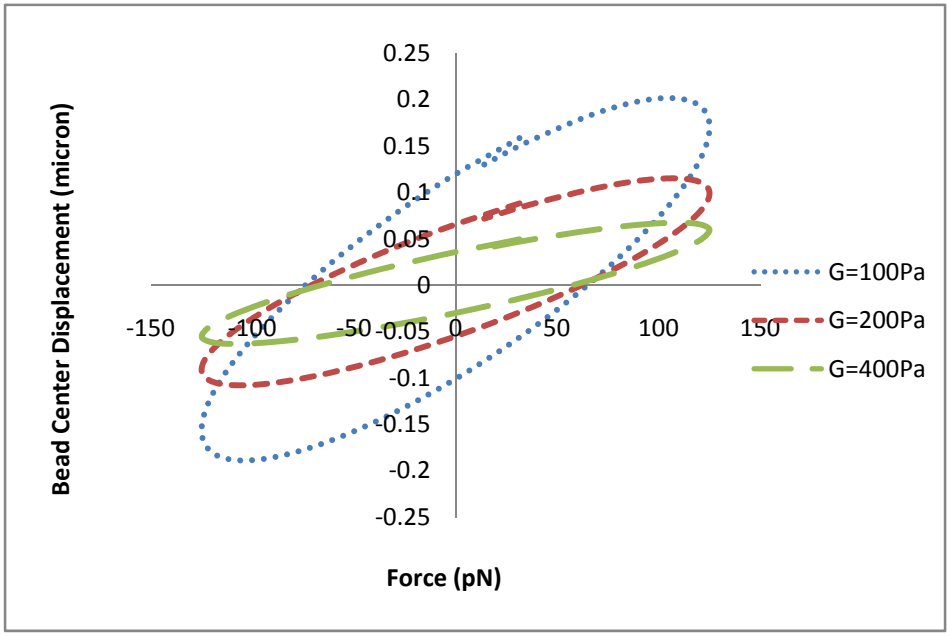

(b)

Figure 4.23 Force versus bead center lateral displacement, resulting from (a) SLS model and (b) SnHS model for fixed sinusoidal force amplitude 125pN with f=0.1Hz for various shear modulus.

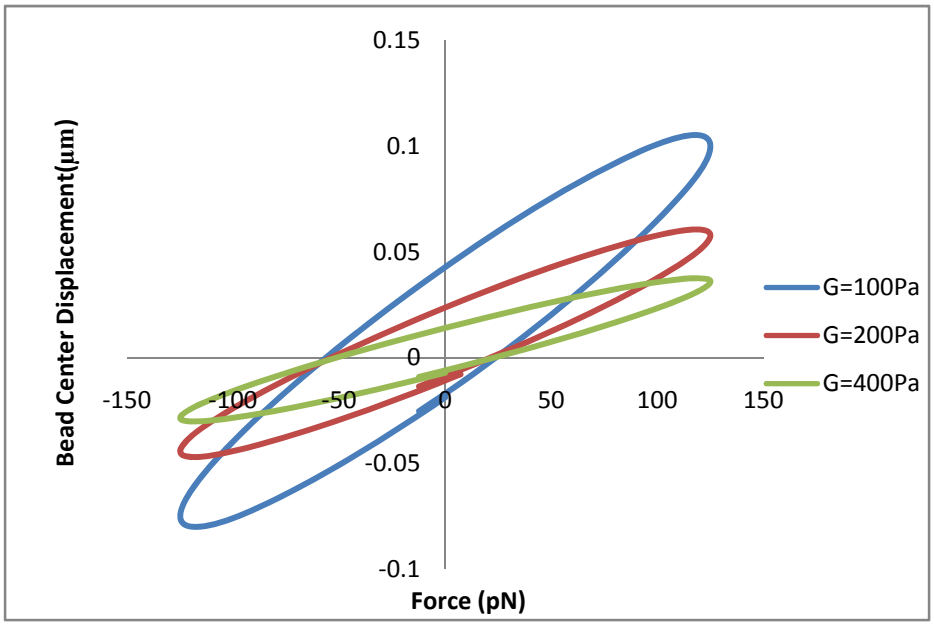

Figure 4.24 Force versus bead center lateral displacement, resulting from the SLS model for fixed sinusoidal force amplitude 125pN with f=0.5Hz for various SLS model shear modulus.

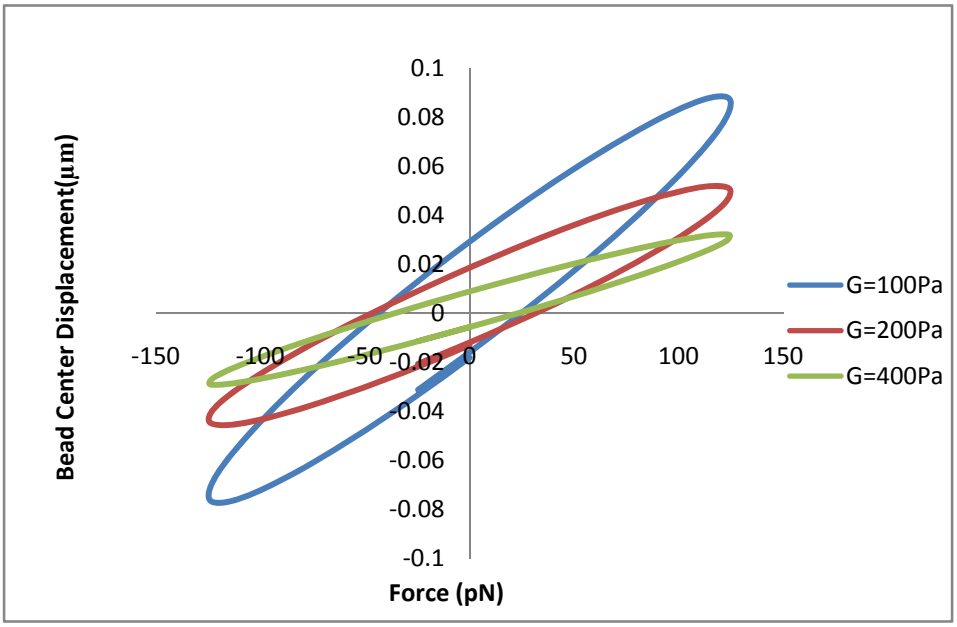

Figure 4.25 Force versus bead center lateral displacement, resulting from the SLS model for fixed sinusoidal force amplitude 125pN with f=1Hz for various SLS model shear modulus.

4.2.3. Influence of Forcing Rate

To further study the cell block viscoelastic behavior, simulations with various rates of force application on the bead were performed. And it is shown from the results that faster forcing rates led to bigger bead displacements (Figure 4.26, 4.27) From the force-bead center displacement curves (Figure 4.28, 4.29), we can see that the curves with different forcing rates comprise a set of concentric ellipses which means that they have the same phase lag but larger radius for larger forcing rate.

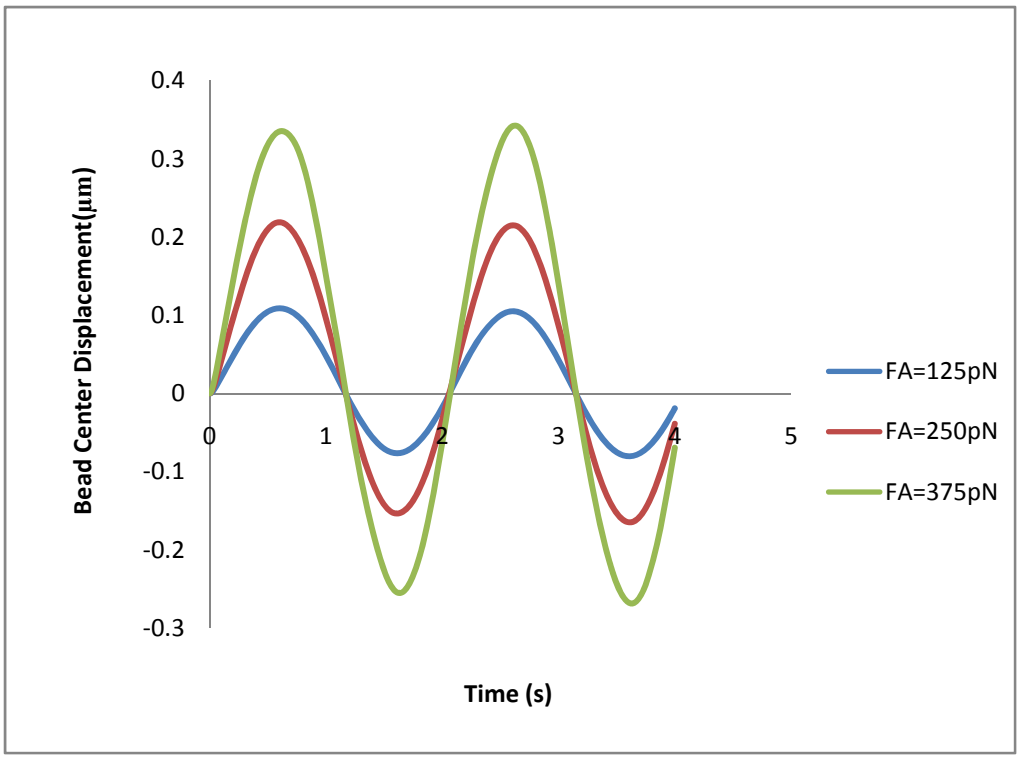

Figure 4.26 Bead center lateral displacement versus time, resulting for SLS model with both cortex and cytoplasm shear modulus 100Pa under fixed frequency f=0.5Hz with various sinusoidal force amplitude.

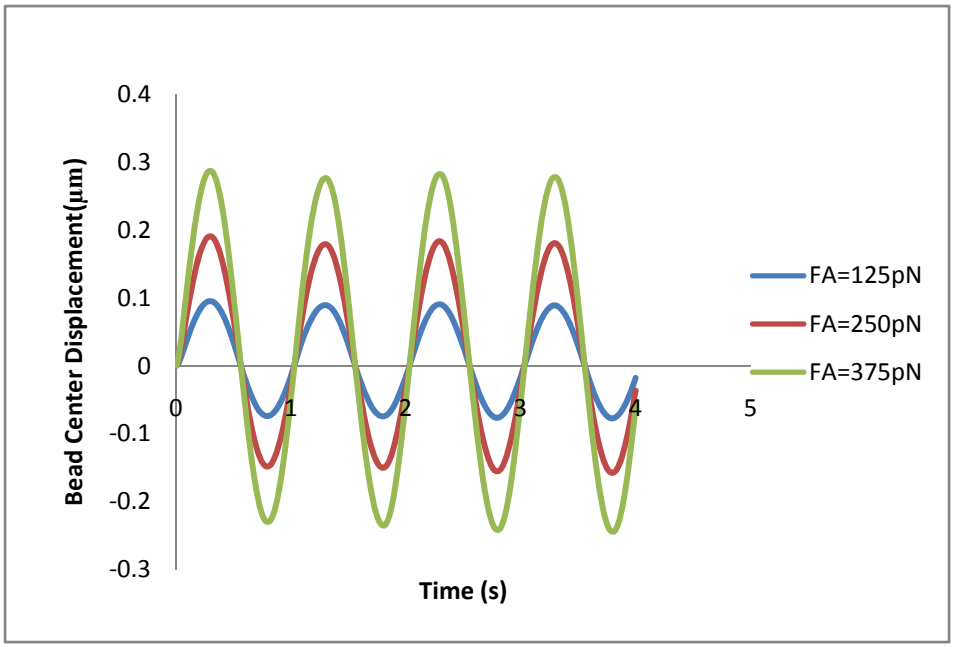

Figure 4.27 Bead center lateral displacement versus time, resulting for SLS model with both cortex and cytoplasm shear modulus 100Pa under fixed frequency f=1Hz with various sinusoidal force amplitude.

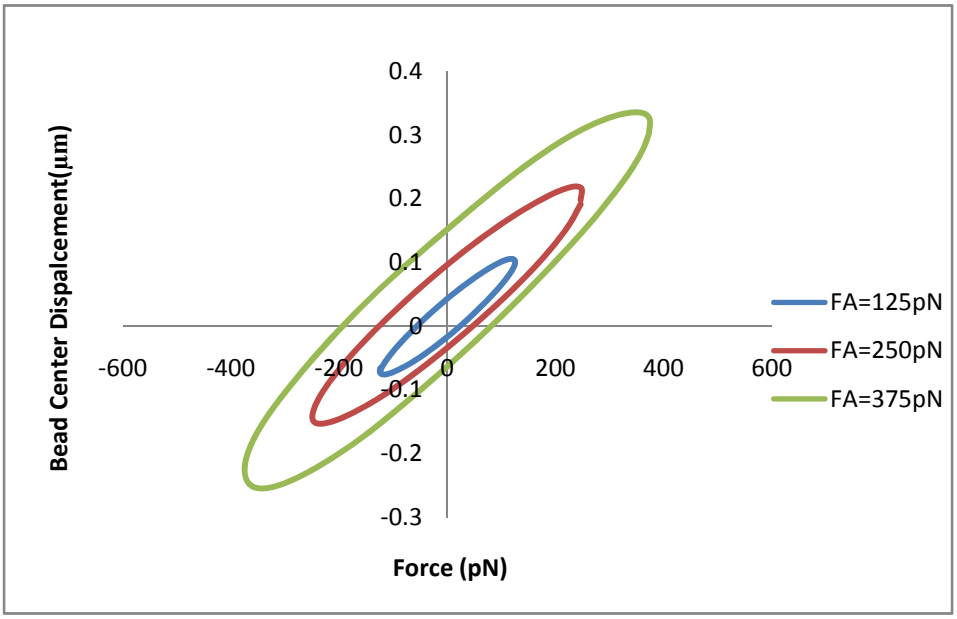

Figure 4.28 Force versus bead center lateral displacement, resulting for SLS model with both cortex and cytoplasm shear modulus 100Pa under fixed frequency f=0.5Hz with various sinusoidal force amplitude.

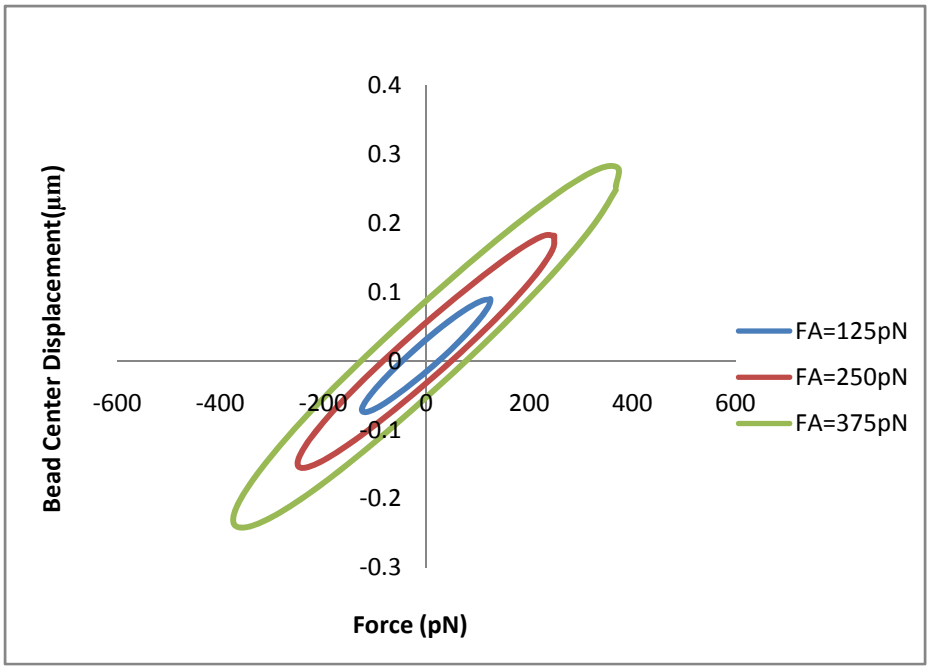

Figure 4.29 Force versus bead center lateral displacement, resulting for SLS model with both cortex and cytoplasm shear modulus 100Pa under fixed frequency f=1Hz with various sinusoidal force amplitude.

E. Conclusion

In this chapter, a nonlinear finite element model of the magnetic twisting cytometry (MTC) on the cell has been developed. The widely used viscoelastic material model- standard linear solid (SLS) viscoelastic model and its natural extension neo-Hookean solid (SnHS) viscoelastic model were introduced into this study for deformation analysis. The constant force and sinusoidal force was applied to study the time-dependent and frequency-dependent viscoelastic material properties of the cell.

Based on the results obtained from finite element analysis, influences of the forcing rates, cytoplasm shear modulus and load frequencies have been systematically studied for the interpretation of the mechanical properties of the cell.

a. Influence of forcing rate: For both constant and sinusoidal force, as the forcing rate increases, the bead center displacement also increases.
b. Influence of cytoplasm shear modulus: By increasing the shear modulus of cytoplasm, the bead center displacement will be increased for the constant force case while for the sinusoidal force case the bead center displacement and phase lag between the force and deformation will be also decreased.
c. Influence of frequency: The results show that bead displacement under sinusoidal forcing exhibits an oscillatory behavior and the displacement decreases as the frequency increases.

Also, it is found that the results of standard linear solid (SLS) viscoelastic model and standard neo-Hookean solid (SnHS) viscoelastic model are almost the same. But SnHS model is more time consuming.

CHAPTER V

FINITE ELEMENT ANALYSIS OF MICROPIPETTE ASPIRATION FOR SINGLE LIVING CELL

A. Introduction

The micropipette aspiration has been used extensively for measuring the mechanical properties of living cells. In the micropipette aspiration experiment, a lower-than ambient hydrostatic pressure is usually exerted on a circular surface of a cell through a glass micropipette. A portion of the cell is sucked into the pipette. In the experiment, the length of the cell projected in the pipette, the pressure applied and the time taken are recorded. The time-dependent pressure-deformation relationship is then obtained and the mechanical properties of the cell are evaluated. One important advantage of this method is that the cell can either be suspended in solution while bound to the micropipette or attached to a surface as the micropipette applies negative pressure from the top. The ability to probe nonadherent cells has made micropipette aspiration a powerful method to probe the viscoelasticity of various types of cells, including erythrocytes [38], leucocytes [39], endothelial cells [40] and chondrocytes [41].

In this chapter, an axisymmetric viscoelastic finite element model is developed for cell micromanipulation by micropipette aspiration. The effects of pipette radius, material properties, pressure rate on rheological behavior of a cell in the process of micropipette aspiration are systematically studied. Numerical results are validated by comparison with the results in [17].

B. Material Constitutive Relation

1. Modeling of Actin Cortex

The actin filaments are known to behave as biopolymers and form a complex filament network whose properties are dependent on the individual filament characteristics. The actin cortex region is modeled as Standard Linear Solid (SLS) and its natural extension Standard neo-Hookean Solid (SnHS) material.

The normalized shear stress relaxation modulus is often represented by a series expansion in Prony Series :

$$g_R(t) = 1 - \sum_{i=1}^{N} g_i[1 - \exp(-t/\tau_i)] \tag{4.1}$$

For the ***standard linear solid*** model see Figure 2, the shear relaxation modulus $G(t)$ can be expressed as a Prony series expansion with the first term:

$$G(t) = G_0[1 - g_1(1 - e^{-t/\lambda_1})] \tag{4.2}$$

The relationship between the two sets of viscoelastic parameters can be derived as

$$G_0 = k_1 + k_2, g_1 = \frac{k_2}{k_1 + k_2}, \lambda_1 = \frac{\mu}{k_2} \tag{4.3}$$

The material properties for SLS and SnHS in this study are given by the follows:

$$G_0 = 200, 400, 600\text{Pa}, g_1 = 0.9, \lambda_1 = 0.1\text{s}$$

2. Modeling of Inner Cytoplasm

Cytoplasm is composed of an organized network of cytoskeleton filaments of actin, inter mediate filaments, and microtubules. Here the material model of cytoplasm region was also assumed as SLS model and SnHS model.

$$G_0 = 200\text{Pa}, \quad g_1 = 0.9, \quad \lambda_1 = 1\text{s}$$

C. FEM Analysis

1. Model Geometry

The cell geometry is model as a sphere with 6 μm diameter, and has been divided into three parts -cortical cytoplasm (cortex), inner cytoplasm and nucleus. The cortical region is assumed to be 0.2 μm thick, and the nucleus is 1 μm in diameter at the center of the sphere. Figure 5.1 presents a schematic representation of the cellular deformation in micropipette aspiration. The finite element mesh of cross section of the cell is shown in Figure 5.2. The cell is assumed to be axisymmetric with a micropipette on the top cell surface. The pipette radius R_p and fillet radius e , are normalized by the initial cell radius $R_c = 6\mu m$. And the dimensionless pipette radius and fillet radius used in this study are: e*=0.1 and Rp*=0.25, 0.4, 0.5, and 0.6.

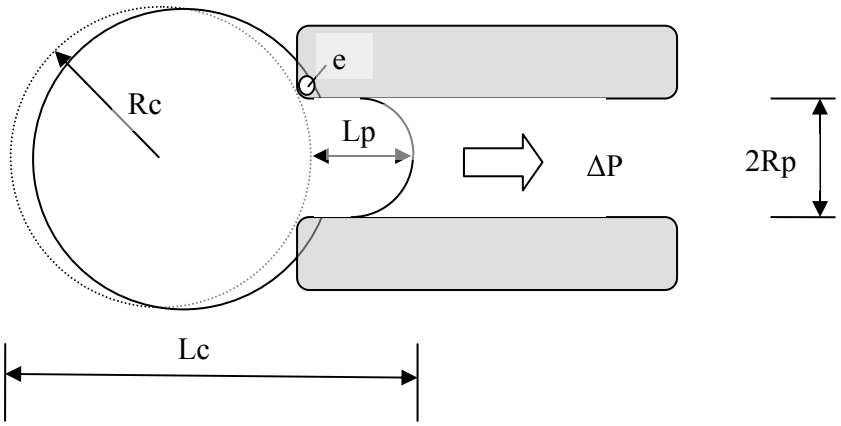

Figure 5.1 The micropipette aspiration of a cell. R_c is the radius of the undeformed cell, R_p is the pipette radius, e is the fillet radius, L_p is the projection length, and L_c is the axial cell length, Δp is the sucking pressure.

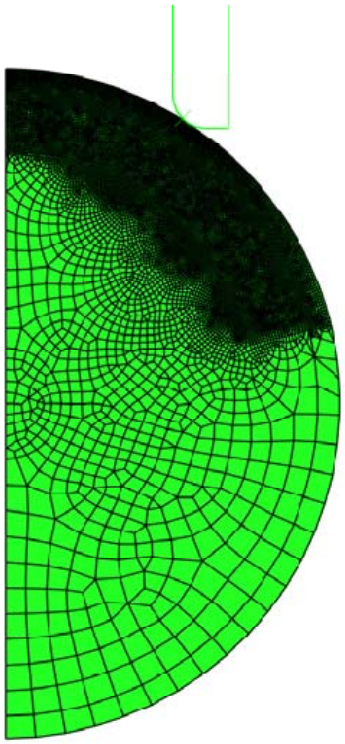

Figure 5.2 An axisymmetric finite element model for the cell.

All simulations were performed using a commercially available finite element modeling software ABAQUS. A dense mesh was adopted near the pipette fillet region because of the large deformation expected in this region. The finite element model consists of 9070 nodes with 12272 CAX4R elements.

2. Boundary Conditions

Fixed displacement boundary conditions are applied on the pipette, while symmetric boundary conditions are applied along the axis of symmetry to the half of the cell section.

3. Applied Load

In this study, the force boundary is modeled as a negative pressure exerted on the non- contact circular opening of the pipette. For the pipette aspiration deformation process which studies the elastic force-deformation relationship, a pressure rate of 100Pa/s is adopted and the maximum load is set to 500Pa. For the creep deformation process which studied the viscoelastic behavior of the cell, constant pressure (instead of rigorous definition of constant stress) 100Pa, 200Pa, 300Pa, 400Pa are applied for 50s.

It is difficult to accurately impose the pressure boundary condition inside the pipette because the boundary surface changes as the cell is sucked into and contact with the pipette wall. Therefore, the criterion is fixed during the entire aspiration process.

D. Results and Discussion

The simulated aspiration processes using the SLS viscoelastic finite element models comprise two cases: pipette aspiration deformation and creep deformation. The effects of the pipette geometry and cortex shear modulus on the cellular viscoelastic behavior in micropipette aspiration have been systematically investigated in this study.

1. Stress Distribution

In general, the stress (von- Mises) field in the cell is concentrated in the area where cell comes in contact with the pipette, see in Figure 5.3. The stresses that observed in the cell exceed pressure up to 3 times for the larger pipette radius. Figure 5.3 (a)-(d) show that as the pipette radius increases, for the same pressure, more portion of the cell is sucked into the pipette and the stress field spread more widely and become larger in the cell. It can be seen that for (a) Rp*=0.25, there is only a small part on top of the cell which experiences large stress, but for case (d), the stress field have enlarged to

nearly half space of the cell, and even the nucleus in the middle of the cell experiences large stress.

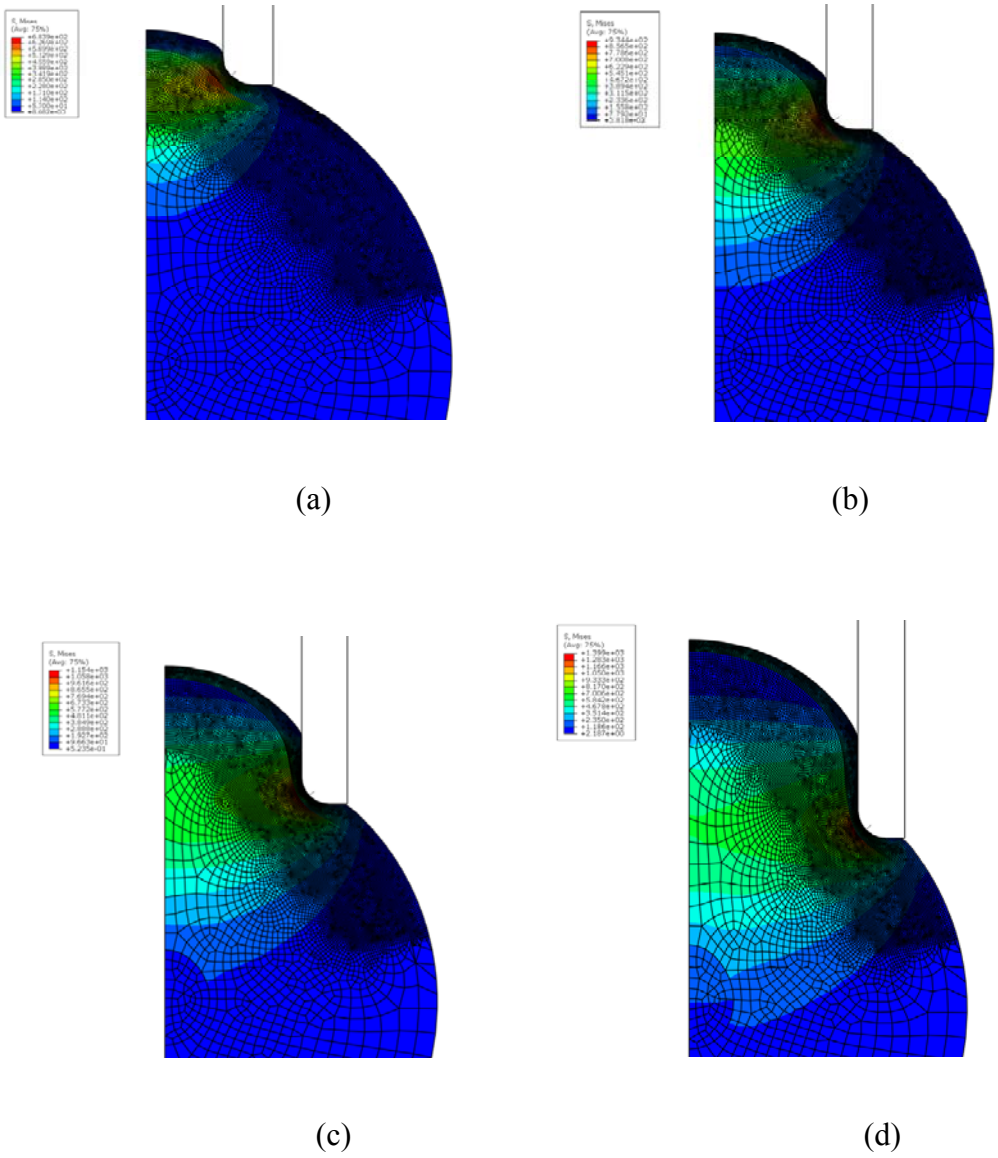

(a) (b)

(c) (d)

Figure 5.3 Stress distribution obtained from the finite element analysis of axisymmetric cell model due to pressure amplitude of 500Pa. (a) Rp*=0.25, (b) Rp*=0.4, (c) Rp*=0.5, (d) Rp*=0.6.

2. Strain Distribution

The strain distribution in cell is also concentrated in the area of cell adjacent to the pipette. Large strain also happened along the area of cell symmetry. The larger the pipette radius, the larger strain near the contact area appeared and the wider the large strain field spread (see Figure 5.4).

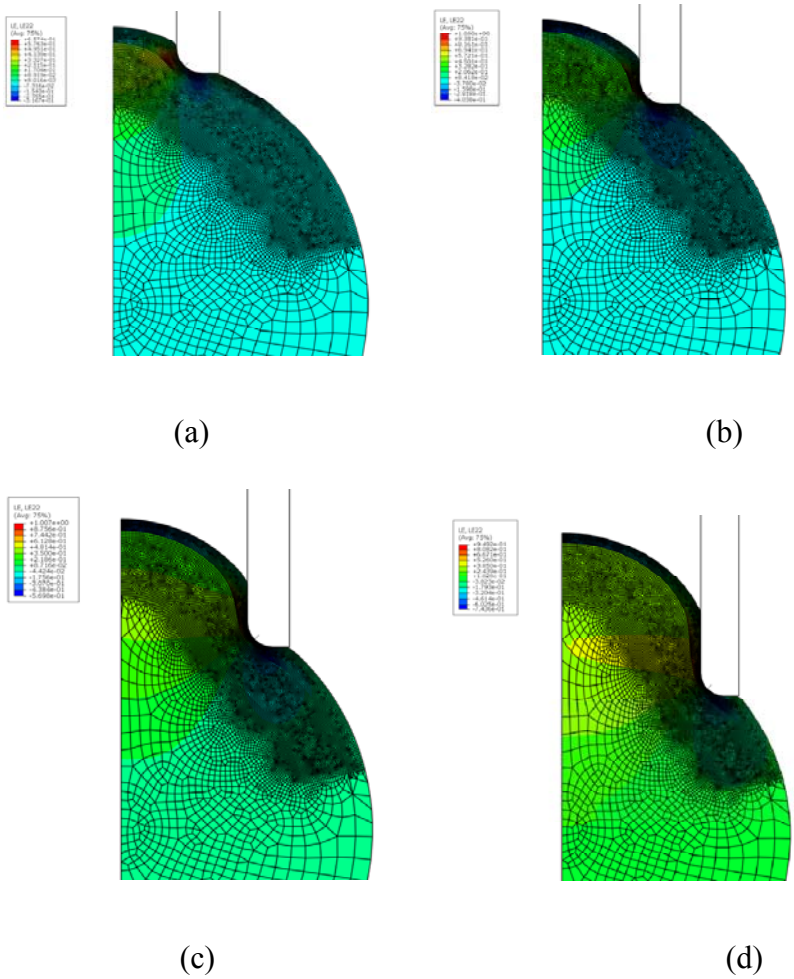

(a) (b)

(c) (d)

Figure 5.4 Strain distribution obtained from the finite element analysis of axisymmetric cell model due to pressure amplitude of 500Pa. (a) Rp*=0.25, (b) Rp*=0.4, (c) Rp*=0.5, (d) Rp*=0.6.

3. Displacement Distribution

The vertical displacement field shown in Figure 5.5 is generally concentrate on the tongue part at the top of the cell which had been sucked into the pipette, while the part in contact with but outside of the pipette have the smallest vertical displacement. As the pipette radius increases, the displacement becomes larger. In (d) Rp*=0.6, nearly entire cell move upward.

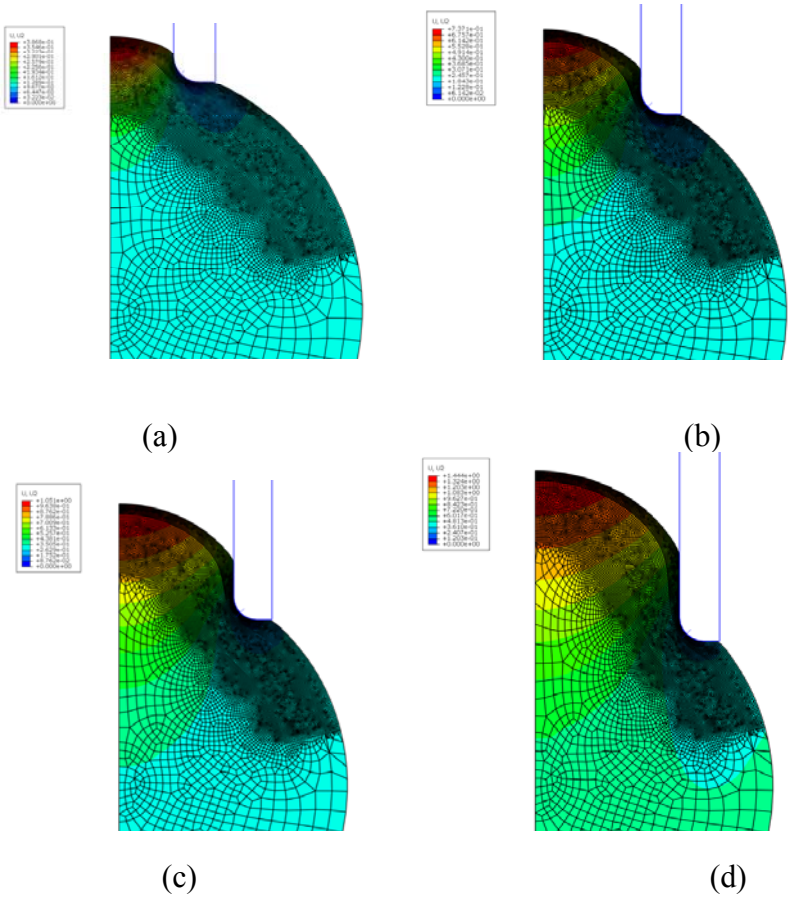

Figure 5.5 Vertical displacement distribution obtained from the finite element analysis of axisymmetric cell model due to pressure amplitude of 500Pa. (a) Rp*=0.25, (b) Rp*=0.4, (c) Rp*=0.5, (d) Rp*=0.6.

4. Pipette Aspiration Deformation Process

4.1.Effect of Pipette Radius

Figure.5.6. – Figure 5.8 show the FEM-computed force-deformation relation for the cases where cortex shear modulus G=200Pa, 400Pa, 600Pa and Rp*=0.25, 0.4, and 0.6. It is found that for the same shear modulus and pressure, the projection length Lp of the cell will increase significantly as increasing the pipette radius. This is reasonable because when the pipette radius becomes larger, more slippage will take place between the pipette wall and cell surface. The results are comparable with the ones in [17].

4.2.Effect of Cortex Shear Modulus

Here the influence of the cortex shear modulus on the overall mechanical behavior of cell has been investigated. In aspiration process there will be no stress fiber formed since they can only formed by the bundling of actin filaments through rigid connections in an adherent cell which occurs for AFM and MTC experiement. Therefore, only the contribution of the cortex material property to the cellular structure has been considered. And reasonably, from Figure 5.9-Figure 5.11 it can be seen that, as the shear modulus of the cortex increases, the cell becomes stiffer for all of the pipette radius cases.

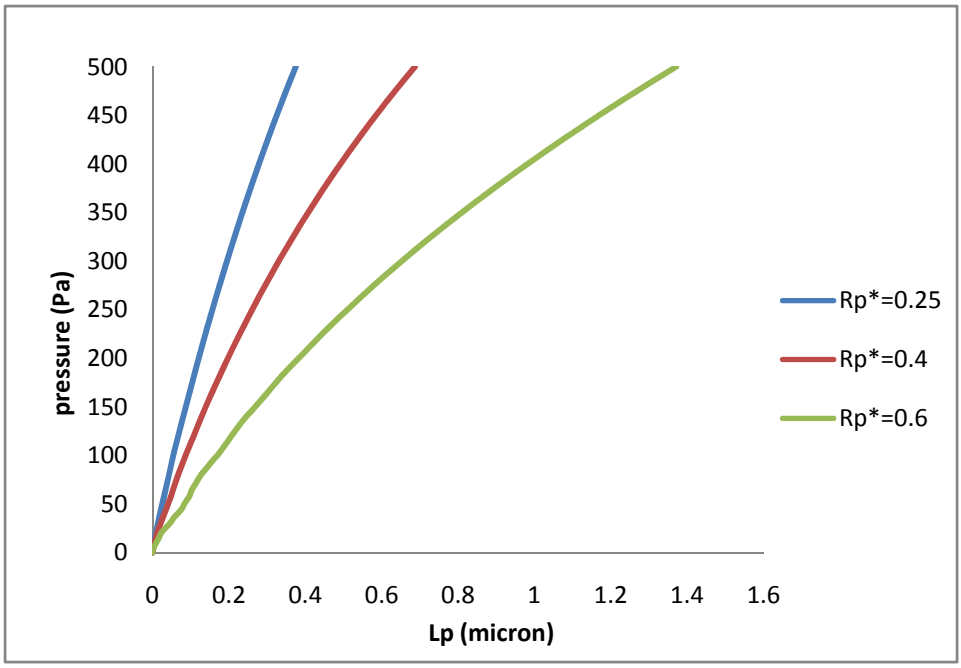

(a)

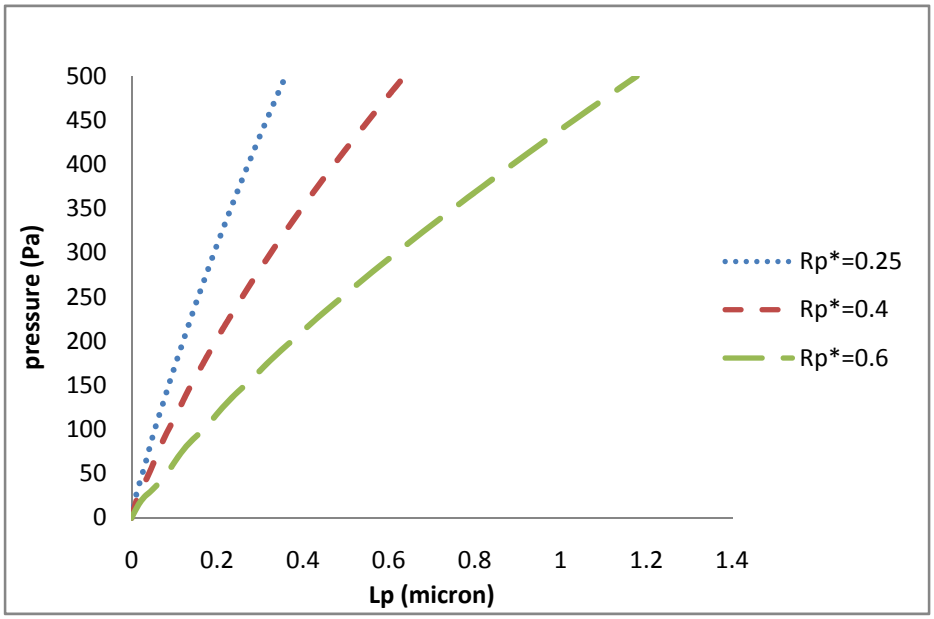

(b)

Figure 5.6 Force-deformation curve of (a) SLS model and (b) SnHS model, with cortex G=200Pa, cytoplasm G=200Pa for various pipette radius.

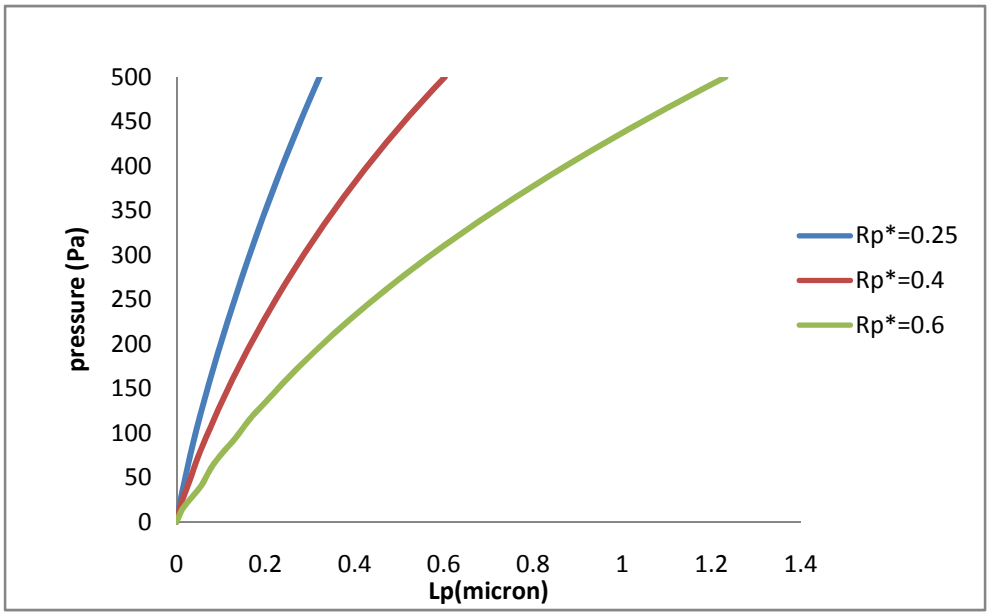

(a)

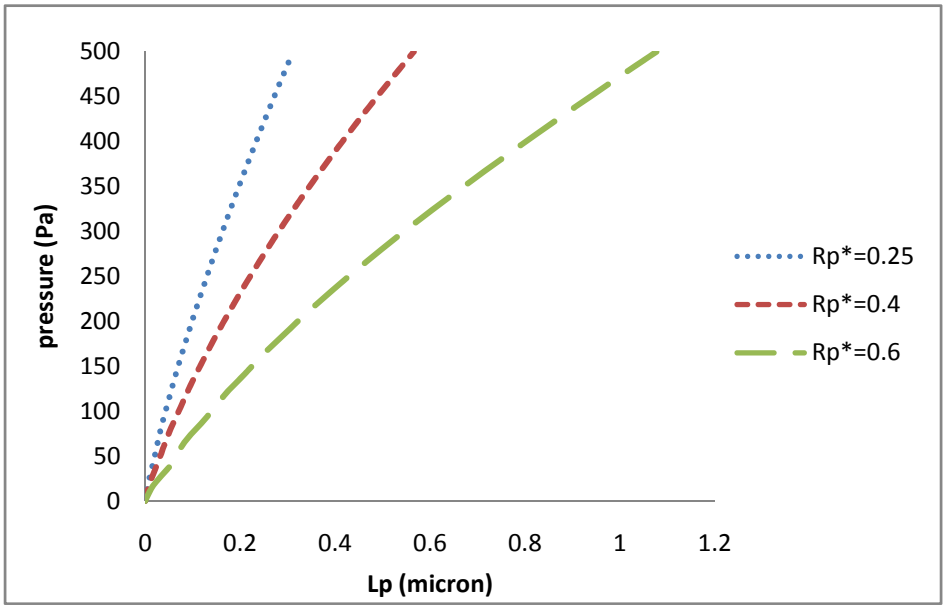

(b)

Figure 5.7 Force-deformation curve of (a) SLS model and (b) SnHS model, with cortex G=400Pa, cytoplasm G=200Pa for various pipette radius.

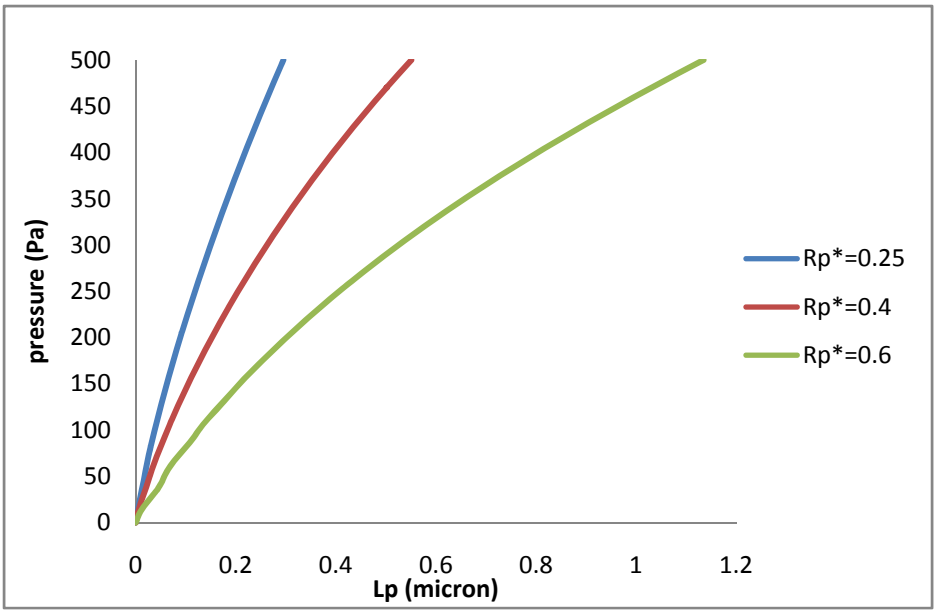

(a)

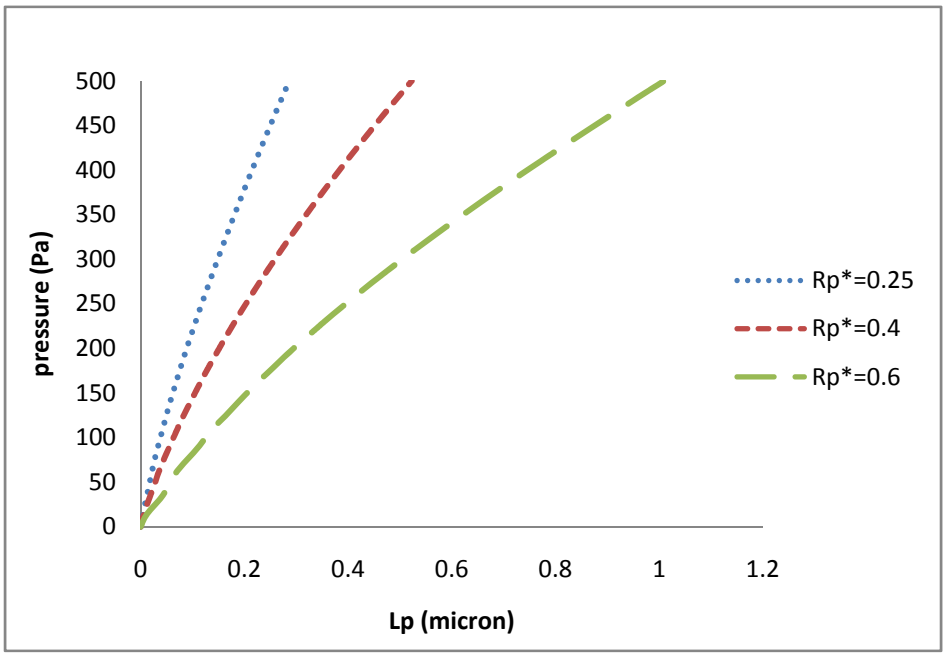

(b)

Figure 5.8 Force-deformation curve (a) SLS model and (b) SnHS model, with cortex G=600Pa, cytoplasm G=200Pa for various pipette radius.

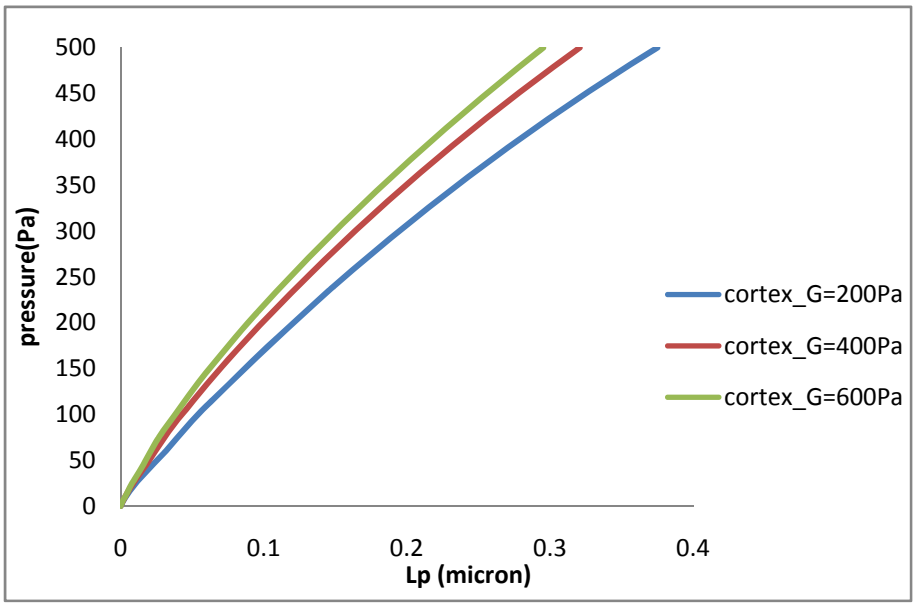

(a)

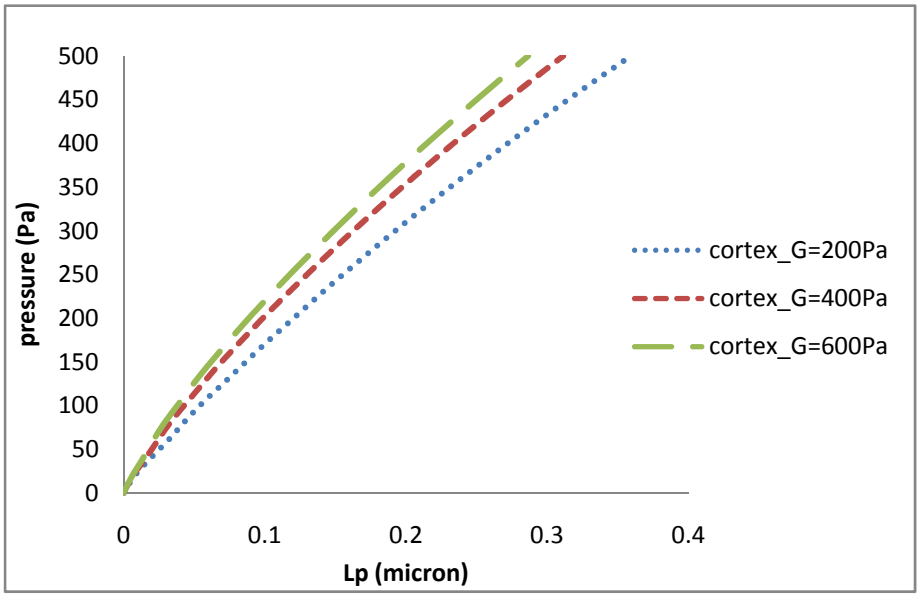

(b)

Figure 5.9 Force-deformation curve of (a) SLS model and (b) SnHS model, with various cortex shear modulus under pipette radius Rp*=0.25.

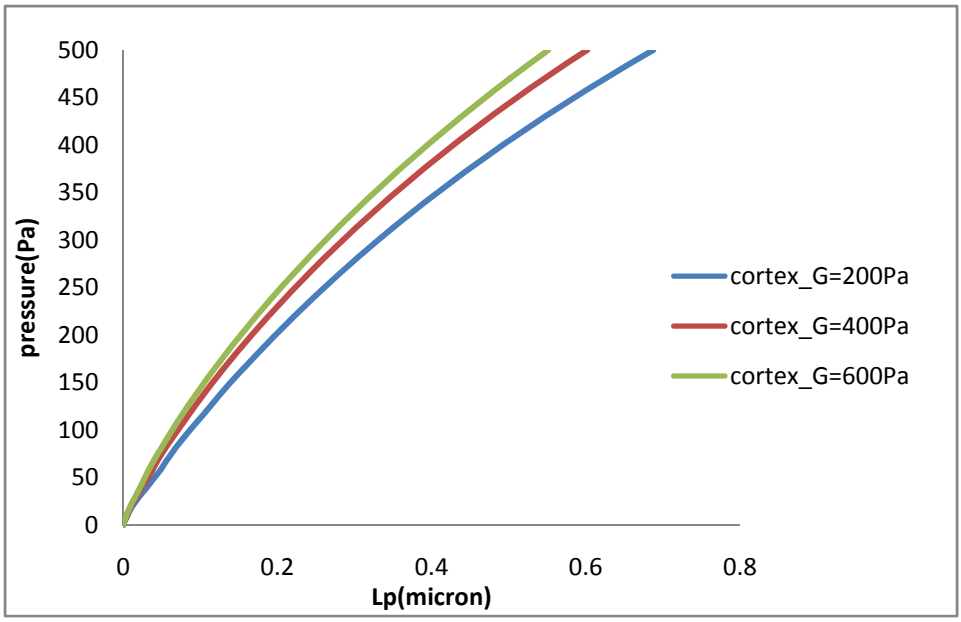

(a)

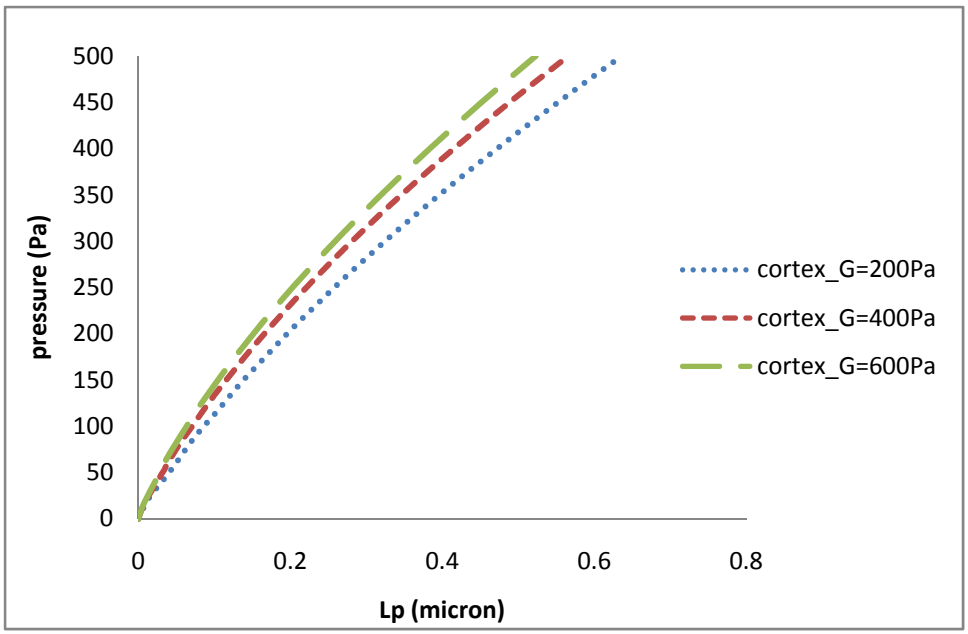

(b)

Figure 5.10 Force-deformation curve of (a) SLS model and (b) SnHS model, with various cortex shear modulus under pipette radius Rp*=0.4.

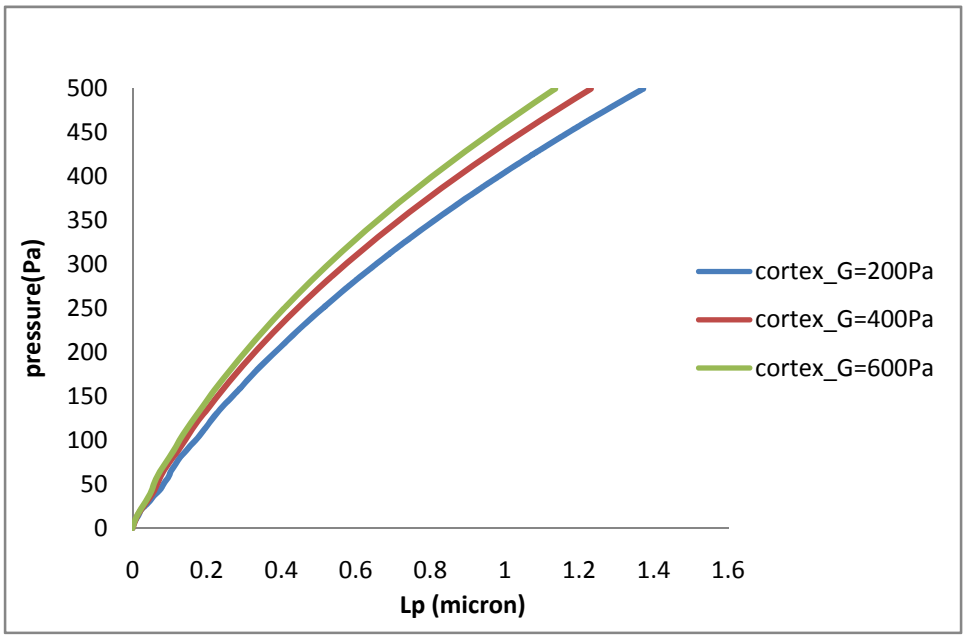

(a)

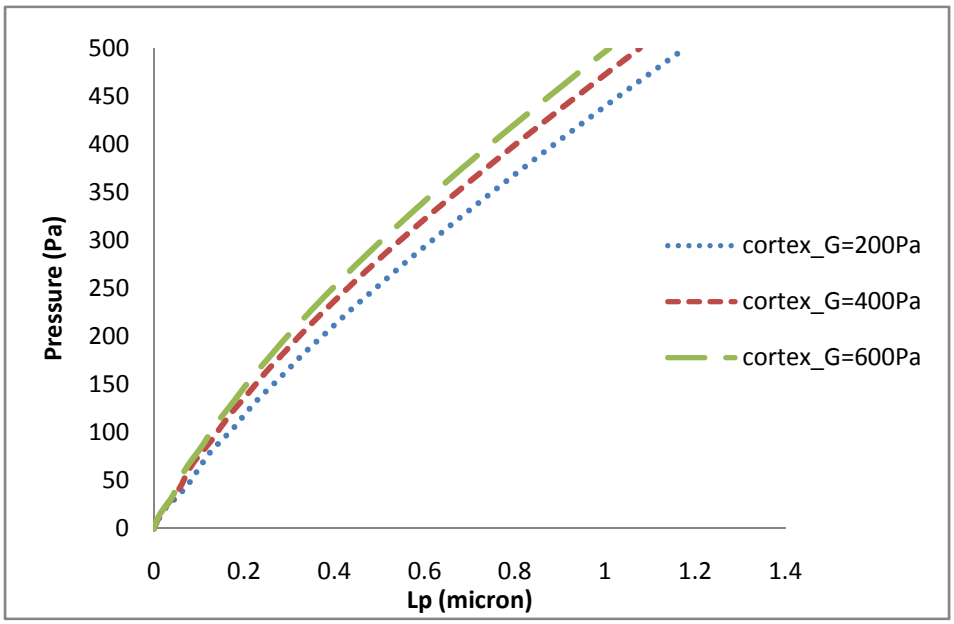

Figure 5.11 Force-deformation curve of (a) SLS model and (b) SnHS model, with various cortex shear modulus under pipette radius Rp*=0.6.

5. Creep Deformation Process

Creep test is a typical experimental technique to investigate the time-dependent material behavior. Although temperature is an important factor in creep test, only the pipette radius, cortex shear modulus and pressure amplitude were consider in the creep process of cell micropipette aspiration. Figure 5.12- Figure 5.15 show the FEM-simulated creep deformation processes for the cases of $e = 0.1$, Rp*=0.25, 0.4 and0.5, as well as cortex shear modulus G=200Pa, 400Pa, 600Pa. It is found that the results of SLS model and SnHS model are nearly the same, except the later is a little bit stiffer, see Figure 5.12. The results can be verified by comparison with the results in [17].

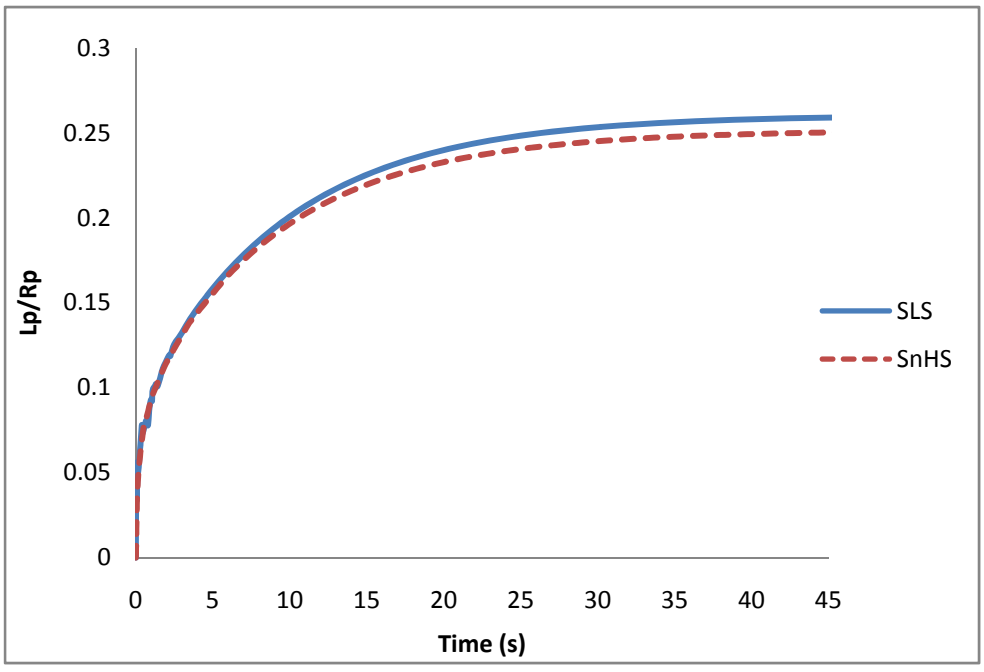

Figure 5.12 Creep deformation process for SLS model (solid line) and SnHS model (dash line) for the case of pressure 100Pa and the shear modulus of both of the cortex and cytoplasm is 200Pa.

5.1.Effect of Pipette Radius

The results shown in Figure 5.13, demonstrate that larger pipette radius will require more time for the creep deformation to reach the plateau. For example, for Rp*=0.25, the creep deformation has already reached its plateau at 50s while for Rp*=0.5, at 50s the creep deformation is still in the slowly increasing stage.

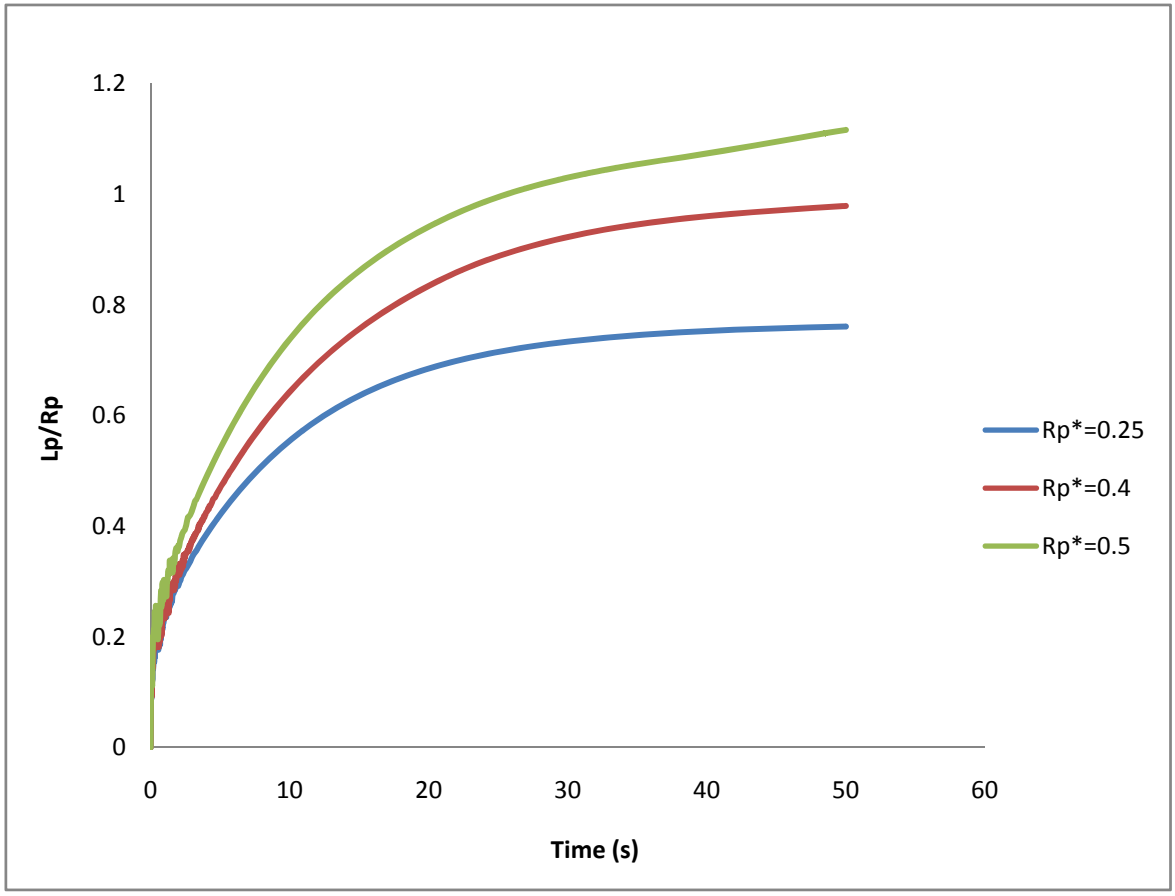

Figure 5.13 Effect of pipette radius on creep deformation process, cortex shear modulus G=200P and p=300Pa.

5.2.Effect of Pressure Amplitude

Here for cases of cortex shear modulus G=200Pa and Rp*=0.25 with various pressure amplitude 100Pa, 200Pa, 300Pa, 400Pa. From the results shown in Figure 5.14 it is found that the deformation is not proportional to the pressure amplitude. And the time needed for the creep deformation to reach the plateau will be longer with larger pressure amplitude.

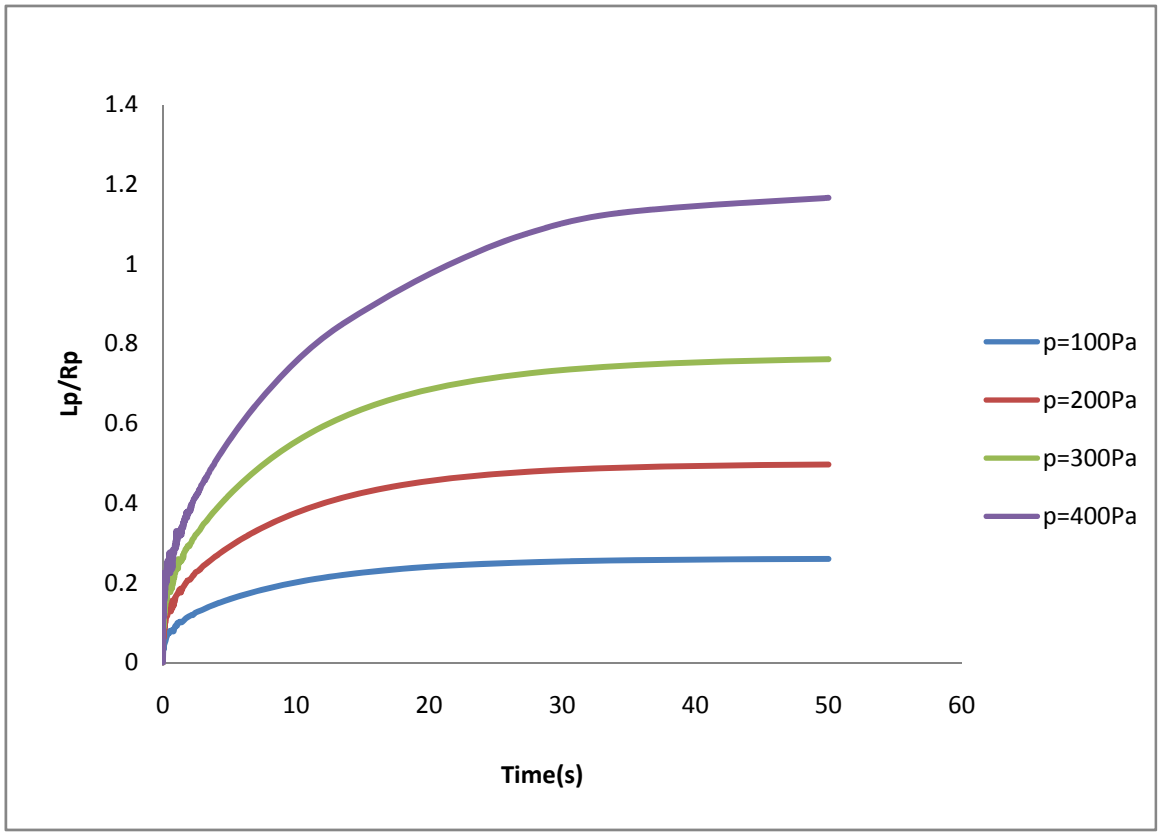

Figure 5.14 Effect of pressure amplitude on creep deformation process, cortex shear modulus G=200Pa and Rp*=0.25.

5.3.Effect of Cortex Shear Modulus

Figure 5.15 shows the creep deformation process for the cases with cortex G=200Pa, 400Pa, 600Pa and Rp*=0.25, and constant pressure 100Pa. It apparent that larger shear modulus will increase the stiffness of the cellular structure. Also, it shows that smaller cortex shear modulus will prolong the time of stabilization.

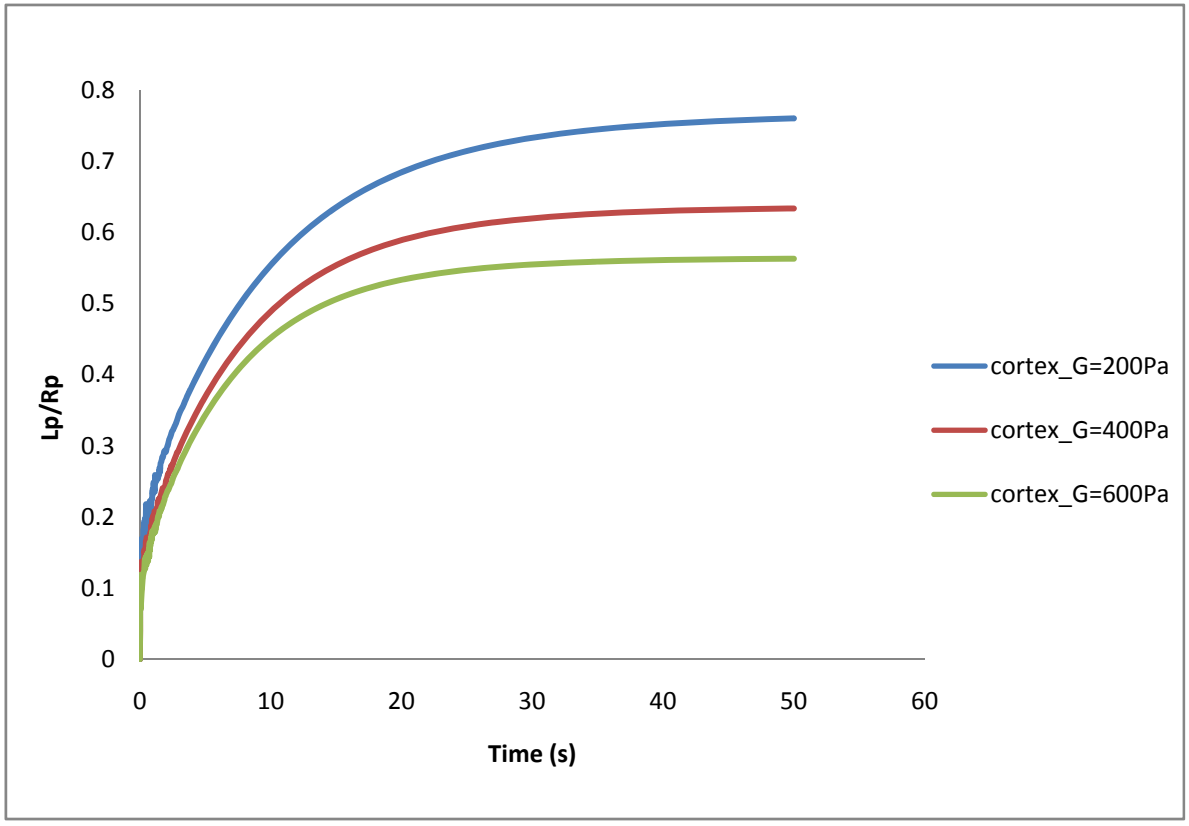

Figure 5.15 Effect of cortex shear modulus on creep deformation process, for fixed Rp*=0.25 and p=100Pa.

E. Conclusion

In this chapter, the micropipette aspiration of spherical cells has been simulated by conductinging nonlinear finite element analysis. The widely used viscoelastic material model- standard linear solid (SLS) viscoelastic model and its natural extension neo-Hookean solid (SnHS) viscoelastic model were introduced into this study for deformation analysis. The effect of pipette geometry is also investigated by changing the ratio of pipette radius to cell radius.

Based on the results obtained from finite element analysis, three relationships have been derived for the description of the mechanical parameters from the micropipette aspiration of cell. a) Effect of pipette geometry: It is found that as the ratio of pipette radius to cell radius Rp^* increases, the deformation Lp and duration of creep deformation process also increase. b) Effect of cortex shear modulus: As the shear modulus of the cortex increases, the cell becomes stiffer for all of the pipette radius cases. For creep deformation process, the results show that smaller cortex shear modulus will prolong the time of stabilization. c) Effect of pressure amplitude: In creep deformation process, it is found that the deformation is not proportional to the pressure amplitude and the time needed for the creep deformation to reach the plateau will be longer with larger pressure amplitude.

Also, by comparing the results of standard linear solid (SLS) viscoelastic model and standard neo-Hookean solid (SnHS) viscoelastic model, it is found SnHS model is a little bit stiffer than SLS model cost more computing time in the same kind of analysis than SLS model. On the other hand, since in SnHS model hyperelasticity is used instead of linear elasticity used in SLS, SnHS model is more general in large deformation analysis which is always the case in cell deformation.

CHAPTER VI

CONCLUSIONS

A. Summary

In this thesis, a continuum -based computational model of living cells that explicitly incorporate the material properties of various cellular components are developed. In the constitutive modeling of cell, the continuum *Standard Linear Solid viscoelastic model (SLS)*, its natural extension for large scale deformation *Standard Neo-Hookean Solid viscoelastic model (SnHS)* as well as polymer mechanics- based *Dynamic Shear Modulus model* was introduced. Finite element simulations of three widely used experiments- atomic force microscopy (AFM), magnetic twisting cytometry (MTC) and micropipette aspiration in the quantification of cell properties were carried out to verify the developed constitutive model.

In Chapter III, and Chapter IV, nonlinear finite elements models for atomic force microscopy (AFM) and magnetic twisting cytometry (MTC) were implemented to investigate both time domain and frequency domain viscoelastic behavior of living single cell. From the results of AFM finite element simulation, it was observed that the force-deformation and strain-relaxation curves obtained fit the experimental results very well. The influences of cytoplasm shear modulus which varies due to the formation of stress fiber were systematically studied. The cortical cytoplasm/cortex is consists of actin filaments network which also can be modeled as semi-flexible biopolymer network. Here, the polymer mechanics based dynamic shear modulus model for cortex was introduced into this work to study the influence of the features of actin filaments network to the overall mechanical properties of the cell. Although this model is an attempt to combine the polymer mechanics based cortex model with the continuum

based cytoplasm model and did not work very well in frequency domain, some relationships have been derived for small deformation case. The results show that the equivalent Young's modulus will increase as the rise of actin concentration factor and frequency.

In magnetic twisting cytometry (MTC) simulation, the role of cytoplasm material properties, constant/sinusoidal forcing rates and various frequencies on the overall mechanical response of a cell was obtained. Numerical results are validated against experiments results.

Micropipette aspiration simulation carried out in Chapter V, in which the typical creep deformation test was carried out to study the viscoelastic behavior of the cell. Based on the results form finite element simulation, the effect of pipette radius, effect of cortex shear modulus and effect of pressure rate have been derived for the interpretation of the mechanical parameters from the micropipette aspiration.

B. Future Works

As an extension to the computational framework presented in this thesis, the following works could be carried out for the future works.

a. Explore the material models to have insight into the structure of cytoplasm, such as how the variation of actin filaments (stress fiber) influences the overall mechanical property of cell.
b. Develop more general polymer mechanics- based cortex model which can be used in large deformation analysis and the study for frequency- dependent viscoelastic material behavior of the cell.

c. Incorporate viscoelastic material properties of nucleus in modeling the cell and represent other experiments, such as optical tweezers/laser traps, to determine the material properties of cells.
d. Study the cellular phenomenon like cell migration and motility which is essential in a variety of biological processes in health (such as embryonic development, angiogenesis and wound healing) or disease (as in cancer metastasis).
e. Study the mechanism of mechanotransduction which is an important function controlling the growth, proliferation, protein synthesis and gene expression of the cell.

REFERENCES

[1] Mofrad, M.R.K., and Kamm, R.D., 2006, “Cytoskeletal mechanics- models and measurements,” Cambridge University Press.

[2] Na, S., Sun, Z., Meininger, G. A., and Humphrey, J. D., 2004, "On Atomic force microscopy and the constitutive behavior of cells," Biomech. Model. Mechanobiol, **3**, pp. 75-84.

[3] Karcher, H., Lammerding, J., Huang, H., Lee, R. T., Kamm, R. D., and Kaazempur-Mofrad, M. R., 2003, "A three-dimensional viscoelastic model for cell deformation with experimental verification," Biophysical Journal, **85**(5), pp. 3336–3349.

[4] Ohayon, J., and Tracqui, P., 2005, "Computation of adherent cell elasticity for critical cell-bead geometry in magnetic twisting experiments," Annals of Biomedical Engineering, **33**(2), pp. 131-141.

[5] Costa, K.D., Sim, A. J., and Yin, F.C.-P., 2006, "Non-Hertzian approach to analyzing mechanical properties of endothelial cells probed by atomic force microscopy," ASME Journal of Biomechanical Engineering, **128**(2), pp. 176-184.

[6] Rotsch, C., and Radmacher, M., 2000, "Drug-induced changes of cytoskeletal structure and mechanics in fibroblasts: An atomic force microscopy study " Biophysical Journal, **78**(1), pp. 520-535.

[7] Humphrey, J.D., 2002, "On mechanical modeling of dynamic changes in structure and properties in adherent cells," Math Mech. Solids, 7, pp. 521-539.

[8] Wu, H.W., Kuhn, T., and Moy, V.T., 1998, "Mechanical properties of L929 cells measured by atomic force microscopy: Effects of anticytoskeletal drugs and membrane crosslinking," Scanning, **20**(5), pp. 389-397.

[9] Hu, S., Eberhard, L., Chen, J., and Love, J.C., 2004, "Mechanical anisotropy of adherent cells probed by a three-dimensional magnetic twisting device," Am. J. Physiol.: Cell Physiol., **287**, pp. C1184-C1191.

[10] Lekka, M., Laidler, P., Gil, D., Lekki, J., Stachura, Z., and Hrynkiewicz, A. Z., 1999, "Elasticity of normal and cancerous human bladder cells studied by scanning force microscopy," European Biophysics Journal, **28**(4), pp. 312-316.

[11] Rao, K.M., and Cohen, H.J., 1991, "Actin cytoskeletal network in aging and cancer," Mutation Research, **256**(2-6), pp. 139-148.

[12] Ingber, D.E., Heidemann, S.R., Lamoureux, P., and Buxbaum, R.E., 2000, "Opposing views on tensegrity as a structural framework for understanding cell mechanics," Journal of Applied Physiology, **89**, pp. 1663-1678.

[13] Darling, E.M., Zauscher, S., Guilak, F., 2006, "Viscoelastic properties of zonal articular chodrocytes measured by atomic force microscopy," OsteoArthiritis and Cartilage, **14**, pp. 571-579.

[14] Peeters, Emile. A.G., Oomens, Cees. W.J., 2005, "Viscoelastic properties of single attached cells under compression," Journal of Biomechanical Engineering, **127**, pp. 237-243.

[15] McElfresh, M., Baesu, E., 2002, "Combining constitutive material modeling with atomic force microscopy to understand the mechanical properties of living cells," P. Natl. Acad. Sci. USA, **99,** pp.6493-6497.

[16] Vaziri, A., Xue, Z., Kamm, R.D., Mofrad, M.R., 2007, "A computational study on power-law rheology of soft glassy materials with application to cell mechanics," Computer methods in applied mechanics and engineering, **196**, pp. 2965-2971.

[17] Zhou, E.H., and Lim, C.T., 2005, “Finite element simulation of the micropipette aspiration of a living cell undergoing large viscoelastic deformation,” Mechanics of Advanced Materials and Structures, **12**, pp.501-512.

[18] Fabry, B., Maksym, G.N., Butler, J.P. Glogauer, Michael, Navajas, Daniel, Taback, N.A., Millet, E.J., and Fredberg, J.J. 2003, “Time scale and other invariants of integrative mechanical behavior in living cell,” Phys. Rve. E**68**:4, 041914.

[19] Bursac, P., Lenormand, G., Fabry, B., Oliver, M., Weitz, D., Viasnoff, V., Bulter, J., and Fredberg, J.J. 2005, “Cytoskeletal remodeling and slow dynamics in the living cells,” Nat. Mater, **4**:7, pp. 557-561.

[20] Hoffman, B.D., Massiera, G., Van Citters, K.M., and Crocker, J.C., 2006, “The consensus mechanics of cultured mammalian cells,” P. Nat. Sci. USA, **103**:27, pp. 10259-10264.

[21] Vaziri, Ashkan, Gopinath, Arvind., and Deshpande, Vikram.S.,2007, “Continuum-based computational models for cell and nuclear mechanics,” Journal of Mechanics and Structures, **2**:6, pp. 1169-1191.

[22] Unnikrishnan, G.U., 2007, “Computational modeling of biological cells and soft tissues,” Doctoral Dissertation, Texas A&M University, pp. 12.

[23] Boal, David, 2002, “Mechanics of cell,” Cambridge University Press.

[24] Heidemann, S.R., and Wirtz, D., 2004, "Towards a regional approach to cell mechanics," Trends Cell Biol., **14**(4), pp. 160-166.

[25] Feneberg,W., Aepfelbacher, M., and Sackmann, E., 2004, "Microviscoelasticity of the apical cell surface of human umbilical vein endothelial cells (HUVEC) within confluent monolayers," Biophysical Journal, **87**, pp. 1338-1350.

[26] McGarry, J.G., and Prendergast, P.J., 2004, "A three-dimensional finite element model of an adherent eukaryotic cell," European Cells and Materials, **16**(7), pp. 27-33.

[27] Lee, K.W., and Xu, X.Y., 2002, "Modeling of flow and wall behavior in a mildly stenosed tube," Medical Engineering & Physics, **24**, pp. 575-586.

[28] Gittes, F., and MacKintosh, F.C., 1998, "Dynamic shear modulus of a semi-flexible polymer network," Physical Review E, **58**, 2, pp. R1241- R1244.

[29] Seifert, U., Wintz, W., and Nelson, P., 1996, "Straightening of thermal fluctuations in semiflexible polymers by applied tension," Phys. Rev. Lett. **77**, pp. 5389-5392.

[30] Granek, R.J., 1997, "Semi-flexible polymers to membranes: Anomalous diffusion and reptation," Phys. II **7**, pp. 1761.

[31] Unnikrishnan, G.U., Unnikrishnan, V.U., Reddy, J. N., 2007, "Constitutive material modeling of cell: A micromechanics approach," Journal of Biomechanical Engineering, **129**, pp. 315-323.

[32] Morse, D.C., preceding paper, 1998, "Viscoelasticity of tightly entangled solutions of semiflexible polymers," Phys. Rev. E **58**, pp. 1237-1240.

[33] Gittes, F. Schnurr, B., Olmsted, P.D., MacKintosh, F. C., and Schmidt, C. F., 1997, "Microscopic viscoelasticity: shear moduli of soft materials determined from thermal fluctuations," Phys. Rev. Lett. **79**, pp. 3286-3289.

[34] Guilak, Farshid, Tedrow, J.R., and Burgkart, Rainer, 2002, "Viscoelastic properties of the cell nucleus," Biochemical and Biophysical Research Communications, **269**, pp.781-786.

[35] Giessibl, F., 2003, "Advances in atomic force microscopy," Reviews of Modern Physics, **75** (3), pp. 949-983.

[36] Maksym, G.N., Fabry, B., Butler, J.P., Navajas, D., Tschumperlin, D.J., Laporte, J.D., and Fredberg, J.J., 2004, "Quantitative analysis of the viscoelastic properties of thin regions of fibroblasts using atomic force microscopy," Biophys, J. **86**(3), pp. 1777-1793.

[37] Puig-de-Moarles, M., Grabulosa, M., Alcaraz, J., Mullol, J., Maksym, G.N., Fredberg, J.J., and Navajas, D., 2001, "Measurement of cell microrheology by magnetic twisting cytometry with frequency domain demodulation," J. Appl. Phys. **91**(3), pp. 1152-1159.

[38] Chien,S., Sung, K. L., Skalak,,R., Usami, S., and Tozeren, A., 1978, " Theoretical and experimental studies on viscoelastic properties of erythrocyte membrane," Biophys J., **24**(2), pp. 463–487.

[39] Schmid-Schonbein, G.W., Sung, K. L., Tozeren, H., Skalak, R., and Chien, S., 1981, "Passive mechanical properties of human leukocytes," Biophys. J., **36**(1), pp. 243–256.

[40] Sato, M., Levesque, M. J., and Nerem, R.M., 1987, "An application of the micropipette technique to the measurement of the mechanical properties of cultured bovine aortic endothelial cells," J. Biomech. Eng., **109**(1), pp. 27–34.

[41] Jones, W. R., Ting-Beall, P. H., Lee, G.M., Kelley, S.S., Hochmuth, R.M., and Guilak, F., 1999, "Alterations in the young's modulus and volumetric properties of chondrocytes isolated from normal and osteoarthritic human cartilage," Journal of Biomechanics, **32**(2), pp. 119–127.

VITA

Name:	Feifei Cheng
Address:	Advanced Computational Mechanics Laboratory, Department of Mechanical Engineering, Texas A&M University, College Station, TX 77843-3123
Email Address:	feifeicheng@tamu.edu
Education:	B.E., Engineering Mechanics, Dalian University of Technology, China, 2005
	M.S., Mechanical Engineering, Texas A&M University, 2008